SILICON-GERMANIUM HBT RECEIVER COMPONENTS FOR MILLIMETER-WAVE EARTH-OBSERVING RADIOMETERS

A Dissertation
Presented to
The Academic Faculty

by

Christopher T. Coen

In Partial Fulfillment
of the Requirements for the Degree
Doctor of Philosophy in the
School of Electrical and Computer Engineering

Georgia Institute of Technology
May 2017

SILICON-GERMANIUM HBT RECEIVER COMPONENTS FOR MILLIMETER-WAVE EARTH-OBSERVING RADIOMETERS

Approved by:

Dr. John D. Cressler, Advisor
School of Electrical and Computer Engineering
Georgia Institute of Technology

Dr. Glenn Lightsey
School of Aerospace Engineering
Georgia Institute of Technology

Dr. Gregory Durgin
School of Electrical and Computer Engineering
Georgia Institute of Technology

Dr. Negar Ehsan
Microwave Instruments and Technology Branch
NASA Goddard Space Flight Center

Dr. Paul Steffes
School of Electrical and Computer Engineering
Georgia Institute of Technology

Date Approved: March 28, 2017

ACKNOWLEDGEMENTS

First and foremost, I would like to thank my advisor, Dr. John Cressler, for all of his guidance, teaching, and unwavering support throughout my eight and a half years as his student. He is truly an outstanding mentor and role model, both professionally and personally. I will forever be grateful to him.

I would like to thank Drs. Paul Steffes and Dr. Greg Durgin for taking the time to serve on my reading committee and provide helpful feedback about my work. I would also like to thank Dr. Glenn Lightsey and Dr. Negar Ehsan for serving on my defense committee. I am particularly indebted to Negar for serving as my NASA fellowship mentor and introducing me to the wonders of microwave absorber foam, Styrofoam, and waveguide packaging.

I am deeply grateful to NASA for supporting me initially through the X-band radar IIP and then for four more years through my Space Technology Research Fellowship. I am indebted to Dr. Jeff Piepmeier from NASA Goddard Space Flight Center for mentoring me during the early years of my fellowship and introducing me to radiometers. I would like to thank Diep, Jared, Quenton, Kongpop, Paul, Shawn, John, Mae, and Matt from Goddard for their support and company during my time there. I would also like to thank Dr. Bill Blackwell from MIT Lincoln Laboratory for providing research guidance and setting up my internship there, and Dr. Tim Hancock and Dr. Chris Galbraith for their support during my time at Lincoln.

I would like to thank Dr. Wyman Williams and Mark Mitchell from the Georgia Tech Research Institute for supporting me over the past year and a half through the

MicroNimbus project. I am excited to join them in the Advanced Concepts Laboratory at GTRI after I graduate. I am also thankful to GlobalFoundries and IHP for the extremely large amounts of free fabrication space they have provided to us. Without their support this research would not have been possible.

I would surely not have made it to this point without the support of my friends and colleagues in the SiGe Group. I would like to particularly thank Steve and Tushar for mentoring me during my first years in the group. I would also like to thank, in no particular order, Rob, Sachin, Jompo, Duane, Richie, Adrian, Milad, Saeed, Peter, Çağrı, Nelson, Michael, Rusty, Moon-Kyu, Zach, Brian, and Rajan. Thank you all so much for the teaching, collaboration, and support over the years, and for helping me unwind during our regular Starbucks and Dunkin runs. I would also like to thank Dr. John Papapolymerou and the former members of the MiRCTECH Group for their support, especially Carlos, Chad, Spyros, and Ben. I am also grateful to the members of the TSRB and GEDC staff for all their support over the years, including Lisa, Carolyn, Maria, Scott, Daphne, Daniel, Craig, and Miss Diane. I would particularly like to thank Roosevelt Hardy for his boundless happiness and enthusiasm, which always made TSRB a brighter place.

Lastly, I would like to thank my friends and family for all of their support. I am particularly thankful to my wonderful wife, Dr. Liz Minne, for putting up with me throughout the past seven years. Without her love, support, and encouragement, I would have quit graduate school years ago. I am also deeply grateful to our dog, Puzzles, for cheering me up after every long day in lab with his smiling face, wagging tail, and unconditional love.

TABLE OF CONTENTS

LIST OF TABLES

LIST OF FIGURES

SUMMARY

The objective of this research is to leverage silicon-germanium (SiGe) heterojunction bipolar transistor (HBT) integrated circuit technologies to develop millimeter-wave receiver components for future space-based atmospheric sounding radiometers. Integrated SiGe components can potentially enable significant reductions in the size, weight, and power consumption of these instruments and enable economical production of radiometers for proposed constellations of Earth-observing CubeSats. The work presented in this dissertation explores the attainable performance of multiple key components of millimeter-wave radiometer receivers developed using best-in-class SiGe HBTs. The results of this work highlight the ability of custom SiGe HBT integrated circuits to substantially improve the integration and power consumption of these receivers while enabling comparable radiometric sensitivity to receivers implemented using traditionally-used millimeter-wave components.

The following is a summary of the contributions of this research:

1. A detailed analysis of the benefits of SiGe HBT technologies versus traditional semiconductor technologies used in CubeSat-based radiometers. This analysis has been presented at the IEEE International Geoscience and Remote Sensing Symposium in 2013 [1] and at the USNC-URSI National Radio Science Meeting in 2014 [2].
2. The design and demonstration of ultra-low noise 18.7 GHz SiGe HBT low noise amplifiers (LNAs) for snow and ice sensing radiometers which utilize back-side

etched inductors to achieve record-setting noise figure. This work was presented at the 2014 IEEE Bipolar/BiCMOS Circuits and Technology Meeting [3].

3. The design and optimization of *G*-band SiGe HBT LNAs for humidity sounding radiometers, along with novel methods for measuring noise figure and linearity on-wafer at these frequencies. This work has been published in the November 2016 issue of the IEEE Transactions on Microwave Theory and Techniques [4].
4. A wideband and low-power intermediate frequency (IF) amplifier and a monolithic active SiGe HBT square-law detector with ultra-low 1/*f* noise for hyperspectral radiometer receivers. The power detector has been submitted to the 2017 European Microwave Integrated Circuits Conference [5].
5. A highly efficient SiGe HBT frequency doubler which demonstrates the ability of custom SiGe circuits to reduce the power consumption of local oscillator multiplication chains in power-constrained systems. This work was presented at the 2016 IEEE Radio Frequency Integrated Circuits (RFIC) Symposium [6].
6. A high-performance monolithically-integrated *G*-band single-sideband downconverter with low power consumption for hyperspectral humidity sounding radiometers. This work has not yet been submitted for publication.
7. The demonstration of two low-loss SiGe HBT Dicke switches for 60 GHz temperature-sounding radiometers, one using a conventional quarter-wave shunt topology and the other using a compact lumped-element pi-network topology. The pi-network switch has been submitted for publication in the IEEE Microwave and Wireless Components Letters [7].

Copyright Statement

In reference to IEEE copyrighted material which is used with permission in this thesis, the IEEE does not endorse any of Georgia Institute of Technology's products or services. Internal or personal use of this material is permitted. If interested in reprinting/republishing IEEE copyrighted material for advertising or promotional purposes or for creating new collective works for resale or redistribution, please go to http://www.ieee.org/publications_standards/publications/rights/rights_link.html to learn how to obtain a License from RightsLink.

Portions of the enclosed text and many of the figures will become IEEE copyrighted material in the future.

CHAPTER 1

INTRODUCTION

1.1 Passive Remote Sensing of the Earth's Atmosphere

Radiometry is a remote sensing technique used to infer information about the physical properties of a material medium through passively characterizing the blackbody radiation emitted by the medium. Microwave radiometric observations are used by the Earth science community to characterize parameters of interest such as ocean salinity, vegetation density, and snow water content. In the millimeter-wave spectrum, Earth-sensing radiometry is typically performed near the resonance frequencies of oxygen (near 60 GHz, 118 GHz, etc.) and water vapor (183 GHz, 325 GHz, etc.) to obtain soundings (vertical distribution profiles) of the Earth's atmospheric temperature and humidity. High-resolution global sounding data are needed to improve global weather forecasting capabilities, as indicated by the 2007 decadal survey recommendation of a Precipitation and All-Weather Temperature and Humidity (PATH) mission [8,9].

Spaceborne radiometric sensors are typically implemented as one-of-a-kind instruments contained in bulky thermally-stabilized and radiation-shielded enclosures that are hosted on large multi-instrument satellites. These satellites generally cost on the order of $1 billion and have long design cycles. Failures of these satellites or instruments are extremely high-impact events. These factors have induced a paradigm shift towards using CubeSats for atmospheric science. Feasibility studies have concluded that CubeSats are capable of hosting millimeter-wave radiometers, and although CubeSat instruments are unlikely to collect the same quality of data as traditional large satellites, CubeSats are far

cheaper (on the order of $1 million), faster to design and construct, and less risky than large satellites [10,11,12]. A major advantage of CubeSats is that they can be potentially be deployed in distributed constellations which can observe localized short-term geophysical events that single satellites are normally unable to observe. The benefits of CubeSat-based radiometers are highlighted by the development of prototypes including RACE [13], MicroMAS [14], MiRaTA [15], and PolarCube [16] along with the envisioned TEMPEST [17] and DOME [10] constellations.

The constrained payload of CubeSats presents a unique instrument design challenge. Radiometers for CubeSats must be capable of performing useful science while being small, lightweight, and low-power. Additionally, constellations of Earth-observing CubeSats may not be economically feasible unless the radiometers are implemented using high-yielding, low-variation components with economy-of-scale benefits. This work investigates the potential of using submillimeter-wave silicon-germanium (SiGe) heterojunction bipolar transistor (HBT) technologies to develop integrated receiver components for low-power atmospheric sounding radiometers. These components can potentially reduce instrument size, weight, and power consumption (SWaP) versus the current state-of-the-art and enable economical manufacturing of millimeter-wave radiometers for proposed constellations of Earth-observing CubeSats. The majority of the circuits presented here pertain to 183 GHz humidity sounding radiometers, as 183 GHz is the highest atmospheric radiometry frequency for which useful low-noise amplifiers (LNAs) can be developed using current SiGe technologies. Furthermore, few commercially-available *G*-band (140–220 GHz) receiver components exist, so developing custom integrated circuit (IC) components does not present a unique instrument design challenge for *G*-band radiometers.

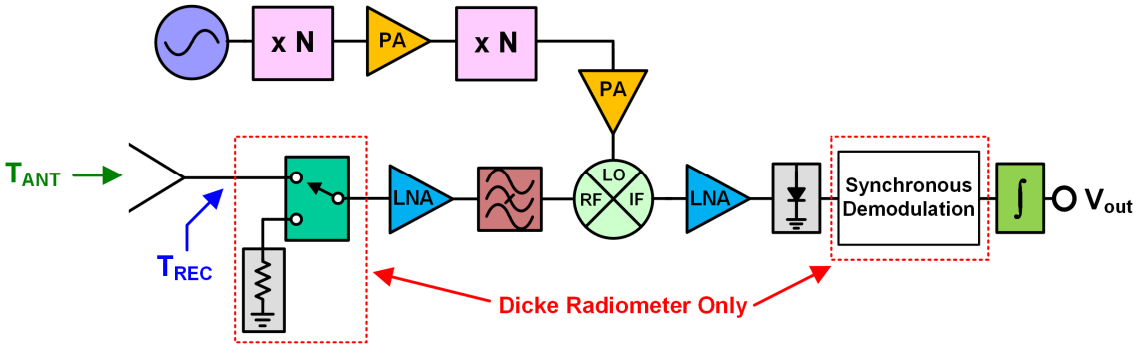

Figure 1.1: Simplified block diagram of a typical millimeter-wave radiometer receiver.

1.2 Radiometer System Fundamentals

A block diagram of a typical millimeter-wave radiometer is shown in Figure 1.1. The antenna receives incoherent noise power, which is represented by an equivalent noise temperature T_{ANT}. The sum of T_{ANT} and the equivalent input-referred noise temperature of the receiver, T_{REC}, is both amplified and bandpass filtered by the receiver and then converted to a voltage by integrating the output from a square-law detector. Millimeter-wave radiometers usually employ a heterodyne architecture and require a low phase noise local oscillator (LO), which is typically generated using a high-quality frequency-multiplied microwave source.

The main figure of merit for this basic radiometer (referred to as a total-power radiometer) is the noise-equivalent temperature difference (NEΔT), which is defined as

$$\mathrm{NE}\Delta\mathrm{T}_{\text{total-power}} = (T_{\mathrm{ANT}} + T_{\mathrm{REC}})\sqrt{\frac{1}{B\tau} + \left(\frac{\Delta G}{G}\right)^2} \qquad (1.1)$$

where B is the bandwidth, τ is the integration time, G is the receiver gain, and ΔG represents receiver gain fluctuations. The parameters B and τ are often constrained by the scientific application and the host platform, and $\Delta G/G$ is generally limited by the $1/f$ noise of the

component technologies used in the receiver. Therefore, to minimize NEΔT, T_{REC} must be minimized by using a high-quality front-end LNA.

In practice, $\Delta G/G$ often dominates the NEΔT. The typical approach to overcome these gain fluctuations is Dicke switching. This is implemented by placing a single-pole double-throw (SPDT) switch at the receiver input and switching between the antenna and a matched ambient load, as shown in Figure 1.1. This switch is actuated at a fixed frequency above the $1/f$ corner frequency of the radiometer, which is the frequency at which the power spectral density of the output white noise equals that of the $1/f$ noise. The modulated noise is synchronously demodulated prior to integration, which filters out most of the low-frequency gain variations due to $1/f$ noise. The NEΔT of the Dicke radiometer is given by

$$\mathrm{NE}\Delta T_{\mathrm{dicke}} = 2(T_{\mathrm{ANT}} + T_{\mathrm{REC}})\sqrt{\frac{1}{B\tau}}. \tag{1.2}$$

The $\Delta G/G$ term is removed by the modulation, but the remaining terms are doubled and T_{REC} is increased due to the switch loss. Many radiometers use alternative modulation techniques such as optical chopping and bias modulation of internal diode noise sources to overcome receiver gain fluctuations without using lossy high-frequency switches [18,19].

1.3 Millimeter-Wave Radiometers for CubeSats

Numerous atmospheric sounders are currently in operation aboard large satellites, including the Advanced Microwave Sounding Unit (AMSU) [20], the Advanced Technology Microwave Sounder (ATMS) [21], the Special Sensor Microwave Imager/Sounder (SSMI/S) [22], and the Global Precipitation Measurement Microwave Imager (GMI) [23]. These instruments each have between 13 and 24 microwave and millimeter-wave channels, and all of the *G*-band channels in these instruments use double-

sideband (DSB) mixer front-ends. The lowest-SWaP instrument, the ATMS, has a mass of 75 kg and power consumption of 130 W. Major SWaP reductions are required to design similar instruments which are compatible with CubeSats. Furthermore, LNA-based radiometers are desired to improve their sensitivity and frequency selectivity.

The first atmospheric sounding CubeSat to be launched was MIT Lincoln Laboratory's Micro-sized Microwave Atmospheric Satellite (MicroMAS), a 34 cm × 10 cm × 10 cm CubeSat which weighs 4 kg and carries a single-sideband (SSB) total-power radiometer with nine channels near 118 GHz for temperature sounding [14]. The radiometer consists of multiple separately packaged modules including a low-noise preamplifier with a weakly coupled noise diode for calibration, a pre-amplified mixer, a frequency-multiplied LO source, and an intermediate frequency (IF) processor. The instrument payload, including the antenna, weighs less than 1 kg and has a volume of 1000 cm^3. The average power consumption is 3 W, which is largely driven by the 90 GHz LO generation (using a resistively tripled dielectric resonator along with a driver amplifier) and the IF processor (dominated by IF amplifiers) [14,24].

The follow-on to MicroMAS, the Microwave Radiometer Technology Acceleration (MiRaTA) CubeSat, is the same size as MicroMAS and weighs 4.5 kg. MiRaTA features a 10-channel tri-band (60, 183, and 206 GHz) radiometer with GPS radio occultation sensors to support both temperature and humidity sounding. The 60 GHz receiver contains radio frequency (RF) LNAs, but the 183 GHz and 206 GHz channels use subharmonic DSB mixer front-ends. This radiometer is also implemented using many separate packaged modules, including a redundant 10 GHz dielectric resonator which is multiplied and amplified to drive the mixers. The payload consumes 6 W of power, which is largely due

to the LO generation and IF processors [15,24]. The planned MicroMAS-2 and Earth Observing Nanosatellite missions aim to increase data collection by adding more channels, adding *G*-band LNAs, and increasing the satellite lifetime [25].

NASA's Jet Propulsion Laboratory (JPL) has developed one humidity sounding CubeSat for the Radiometer Atmospheric CubeSat Experiment (RACE) (originally known as CHARM) [26,27]. The RACE instrument was a two-channel 183 GHz radiometer which used a direct-detection topology to eliminate the need for a mixer and the associated power required to generate a millimeter-wave LO, enabling an instrument power consumption of 1.5 W. The radiometer front-end, which was integrated into a compact waveguide module, utilized 35 nm indium phosphide (InP) high electron mobility transistor (HEMT) LNAs with noise figures (NFs) of 4 dB or less to achieve excellent radiometric sensitivity [28]. Internal calibration was enabled through the use of a Dicke switch with a matched load along with a weakly coupled hot noise source (implemented using an LNA with a matched input termination). A separate diplexer module performed channel splitting, filtering, and detection. The receiver NF was 8 dB, which was largely dominated by the 3 dB insertion loss (IL) of the front-end Dicke switch [13]. Although RACE was lost in the 2014 Orb-3 launch failure, JPL's millimeter-wave radiometers for CubeSats continue to advance through the ongoing development of the Microwave Atmospheric Sounder on Cubesat (MASC) and Tropospheric Water and Cloud Ice (TWICE) instrument prototypes [29,30].

Future sounding CubeSats would greatly benefit from higher RF front-end integration, more efficient LO generation, and improved efficiency and integration in the IF modules. In order to practically produce many (~15–30) identical instruments for envisioned CubeSat constellations, these instruments would ideally use high-yielding

millimeter-wave components with economy-of-scale manufacturing benefits. Highly scaled InP components are notorious for having relatively low yields and non-optimal economy-of-scale benefits. An ideal radiometer receiver for CubeSats would be a single chip with similar performance to InP receivers and manufactured in a silicon-based technology. This work explores the feasibility of implementing such a radiometer using existing SiGe bipolar-CMOS (BiCMOS) technologies.

1.4 SiGe BiCMOS Technologies

A SiGe HBT is essentially a silicon BJT with a graded SiGe alloy placed in the base region that significantly improves the transistor's performance versus that of a BJT [31]. Unlike III-V transistors, which are typically only suitable for RF usage, SiGe HBTs are specifically designed to balance RF, analog, and digital performance to enable application flexibility. Commercially-available SiGe BiCMOS processes offer SiGe HBTs side-by-side with silicon CMOS, and emerging platforms include diverse offerings such as capacitive micro-electro-mechanical systems (MEMS) switches and integrated photonics elements to enable unprecedented levels of system-on-chip integration [32,33]. SiGe technologies have low across-wafer performance variability and are readily accessible through multi-project wafer (MPW) services, unlike most submillimeter-wave InP and gallium arsenide (GaAs) processes. The ability to fabricate small-sized chips with shared mask costs makes the MPW development model well-suited for economically fabricating radiometer components for CubeSat constellations.

The RF performance of SiGe HBTs is rapidly advancing. Multiple BiCMOS processes now offer SiGe HBTs with peak unity gain cutoff frequencies (f_T) and maximum oscillation frequencies (f_{max}) of up to 300 and 500 GHz, respectively [34,35]. Multiple

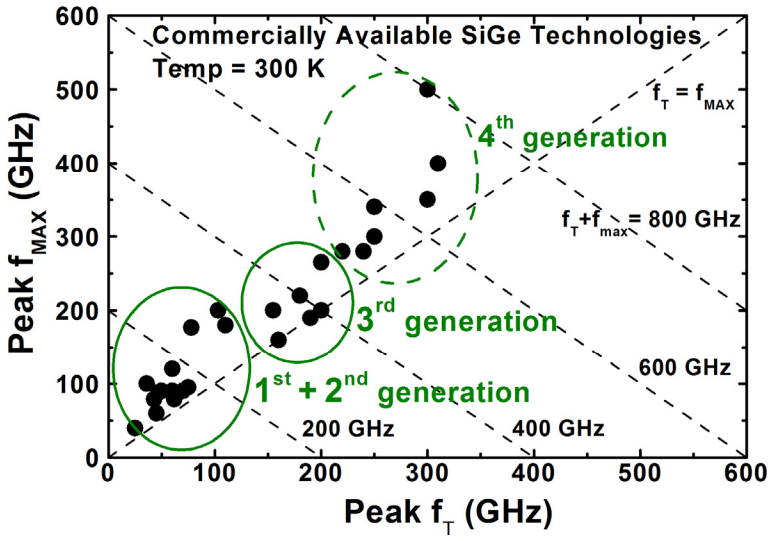

Figure 1.2: Peak f_{max} versus peak f_T of commercially-available SiGe BiCMOS technologies © 2013 IEEE [1].

foundries offer commercially-accessible SiGe BiCMOS technologies with peak f_{max} of 300 GHz or higher, as shown in Figure 1.2. Although highly-scaled n-type field-effect transistors (nFETs) attain similar performance, SiGe HBTs achieve significantly higher f_{max} at the top metal layer as a result of the relaxed lithography and back-end-of-line metallization used in SiGe technologies [36,37]. Recent publications have presented SiGe HBTs operating with peak f_{max} as high as 720 GHz at room temperature [38] and 798 GHz at 4.3 K [39]. It has been projected that with proper scaling, SiGe HBTs can eventually achieve greater than 900 GHz peak f_{max} [40]. SiGe HBTs cannot yet achieve the same RF performance as the best III-V technologies, however. InP HBTs from Teledyne Scientific achieve peak f_T/f_{max} of 520/1100 GHz at the 0.13 μm node [41], while 35 nm indium gallium arsenide (InGaAs) metamorphic HEMTs (mHEMTs) from Fraunhofer IAF achieve 515/>1000 GHz [42] and 25 nm InP HEMTs from Northrop Grumman Aerospace Systems attain 0.61/1.5 THz [43].

1.5 Advantages of SiGe Technologies for CubeSat-Based Radiometers

Although multiple publications have concluded that SiGe technologies are well-suited for use in radiometers, few SiGe-based radiometers have been demonstrated outside of the laboratory environment [44,45,46]. The general paradigm in the remote sensing community is to design one-of-a-kind radiometers to achieve the best attainable performance, so III-V MMICs are typically used. The primary drawback of SiGe HBTs versus III-V devices with respect to radiometers is a higher minimum NF, so SiGe radiometers cannot achieve sensitivities as low as III-V-based radiometers. However, SiGe has many advantageous characteristics over III-V technologies for use in CubeSat-based radiometers, as will be discussed throughout the remainder of this section. This analysis has been published in [1] and [2].

1.5.1 Fabrication

Receivers developed using III-V monolithic microwave ICs (MMICs) are not well-suited for large-scale production. Fabricating III-V MMICs is expensive and extremely technically challenging. III-V semiconductors typically have poor fabrication properties—only small wafers can be used (150 mm or less), yields are low, and performance can vary significantly from die to die, which makes III-V fabrication expensive. Thorough testing is required to ensure all components have sufficiently similar performance for implementing a number of identical receivers.

SiGe technologies, on the other hand, are well-suited for scale production. Silicon fabrication lines use large (200 mm) diameter wafers, are high yielding, and have low chip-to-chip performance variations. Lithographic mask set generation drives costs in silicon fabrication, and the actual wafer processing is relatively cheap. In III-V technologies, on

the other hand, the opposite is true—mask set generation is cheaper (fewer masks are required) and processing costs are significant. SiGe platforms are best utilized in applications where these economy-of-scale benefits can be realized.

1.5.2 Low-Frequency Noise

Short-term and long-term performance stability is a critical consideration in scientific radiometers, where sensitivity must be traded off to correct for short-term and long-term performance fluctuations in the receiver. Short-term gain fluctuations are primarily caused by the 1/*f* noise (flicker noise) in the active devices in the receiver. In order to ease the chopping and calibration requirements for these radiometers, devices with excellent 1/*f* noise are highly desirable.

1/*f* noise in transistors is primarily caused by defects at the semiconductor-oxide interfaces. SiO_2 is an excellent oxide that is easily thermally grown, so silicon-based devices generally have high-quality oxide interfaces. High-quality oxides cannot be easily grown on GaAs and InP, however, so oxide interfaces in these technologies tend to be low-quality with much higher defect densities than in silicon. For this reason, III-V devices have higher levels of 1/*f* noise than silicon-based devices [47].

Field effect devices such as FETs and HEMTs operate by passing current in a very thin layer directly under the critical barrier-channel interface. Bipolar devices such as BJTs and HBTs, on the other hand, are typically grown vertically, so only a small amount of current encounters defects at the oxide interfaces. Bipolar devices therefore have substantially lower 1/*f* noise than field-effect devices [48].

The addition of germanium in SiGe HBTs further improves their 1/*f* noise characteristics. The main interface which introduces defects in SiGe HBTs is the emitter-

base spacer oxide, so 1/*f* noise in the base current drives the 1/*f* noise of the SiGe HBT [49]. The germanium in SiGe HBTs increases the current gain, which suppresses the base current and reduces the input-referred 1/*f* noise of SiGe HBT below that of identical BJTs. Due to these advantages, SiGe HBTs have the best low-frequency noise characteristics of all high-frequency semiconductor technologies [47].

1.5.3 Total-Dose Radiation Tolerance

Due to the small size and weight of CubeSats, only a limited amount of radiation shielding can be included on-board. Therefore, the use of total-dose tolerant electronics in these applications is highly desirable in order to maximize the lifetime of the instrument electronics in the harsh operating environment of space.

Total-dose radiation primarily affects oxide-semiconductor interfaces, introducing defects, as described in the previous section. In field-effect devices, damage to the critical oxide-channel interface increases the threshold voltage, reduces transconductance (gain), and increases the 1/*f* noise. In bipolar devices total-dose damage mainly occurs at the less critical emitter-base spacer oxide interface. As shown in Figure 1.3, critical RF parameters such as f_T, f_{max} and NF are only slightly degraded by multi-Mrad(SiO_2) doses, far higher doses than would be experienced during the lifetime of a CubeSat orbiting the Earth. Low-frequency noise increases as well, but because the interface damage occurs in non-critical regions of the HBTs, the relative increase is less than that which occurs in a field-effect device. III-V and silicon devices respond similarly to total-dose damage; the most important factor being the physical structure of the device [50].

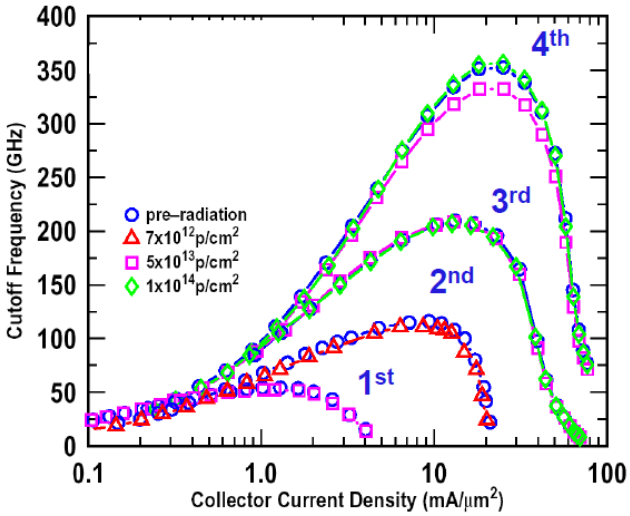

Figure 1.3: Measured f_T versus collector current density as a function of 63 MeV proton fluence for multiple generations of SiGe HBTs [51]. The highest dose shown corresponds to a total dose of more than 13 Mrad(Si).

1.5.4 Thermal Control

Unlike large scientific satellites, CubeSats are highly SWaP-constrained platforms, so their capability for providing precise thermal control is limited. Consequently, passive thermal control techniques such as heat sinks and thermally insulating tapes are typically used in CubeSats. The temperature inside CubeSats typically ranges between -15° C and 40° C in sun-synchronous orbits, a much wider range than in large scientific satellites [11]. Technologies which have inherently stable behavior across temperature and are compatible with low-power thermal control techniques are desirable for these applications.

SiGe BiCMOS technologies have many advantages over III-V technologies for thermal control. The thermal conductivity of bulk silicon at is 1.41 W/cm·K at 300 K, while the thermal conductivities of GaAs and InP are 0.46 and 0.68, respectively. This higher conductivity improves the ability of silicon-based devices to dissipate heat from critical device junctions, which increases device reliability and allows for rapid thermal

equalization across die [48]. An integrated SiGe radiometer would have relaxed thermal control requirements due to its small size and high thermal conductivity. Some active thermal control could potentially be applied using on-chip resistive micro-heaters [46].

The availability of SiGe HBTs with CMOS enables the design of on-die analog temperature sensors, which can be implemented close to each of the receiver blocks. This cannot be readily done in III-V platforms. Bandgap temperature sensors can be implemented on-chip using proportional to absolute temperature (PTAT) biasing sources. Additionally, on-die active biasing circuits can be used to reduce performance variations in RF circuits due to varying temperature. The reduced gain drift enabled by active temperature-compensating bias networks would reduce the need for frequent calibration and help compensate for the higher intrinsic NF of SiGe with respect to III-V transistors.

1.6 Objectives and Organization

The objective of this research is to leverage SiGe HBT technologies to develop millimeter-wave receiver components for future space-based atmospheric sounding radiometers which require integration and power efficiency. The work presented in this dissertation explores the attainable performance of multiple key components of millimeter-wave radiometer receivers developed using best-in-class SiGe HBTs. The results highlight the ability of custom SiGe HBT integrated circuits to substantially improve the integration and power consumption of these receivers while enabling comparable radiometric sensitivity to receivers implemented using traditionally-used millimeter-wave components.

Figure 1.4 shows a block diagram of a notional radiometer receiver which depicts a visual outline of this dissertation. Chapter II discusses the design, optimization, and characterization of SiGe HBT LNAs—the primary NEΔT-constraining blocks in high-

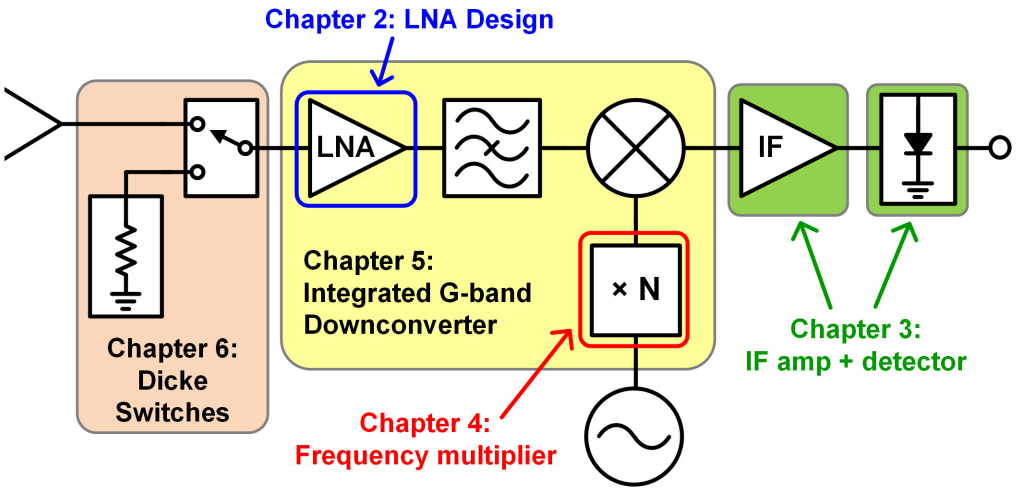

Figure 1.4: Block diagram of a notional radiometer receiver which outlines the topics discussed in this dissertation.

frequency radiometers—to show that SiGe receivers can attain comparable noise performance to traditional III-V based receivers. Chapter III presents the design of two wideband components for low-SWaP hyperspectral millimeter-wave radiometers, a low-power IF amplifier and a SiGe HBT square-law detector with ultra-low $1/f$ noise. Chapter IV presents a power-efficient millimeter-wave SiGe HBT frequency doubler which highlights the potential of custom SiGe RFICs to significantly reduce the power required to drive millimeter-wave mixers. Chapter V leverages the results of Chapters II and IV to demonstrate a monolithically integrated, power-efficient, and low-noise *G*-band single-sideband downconverter for hyperspectral humidity sounding radiometers. Finally, Chapter VI presents two compact and low-loss single-pole double-throw Dicke switches for *V*-band temperature-sounding radiometers developed using reverse-saturated SiGe HBTs.

CHAPTER 2

HIGH FREQUENCY LOW-NOISE AMPLIFIERS

2.1 Introduction

Low-noise amplifiers (LNAs) are essential elements of high-quality radiometer receivers. The gain and effective input-referred noise temperature, T_{eff}, of the front-end LNA drives the effective noise temperature of the receiver, T_{rec}. Minimizing T_{rec} is essential to ensure a low system NEΔT (and therefore high radiometric sensitivity), following Equations 1.1 and 1.2. Data quality is paramount in scientific applications, so SiGe receivers must yield a comparable NEΔT with compelling SWaP and cost benefits if they are to be used instead of III-V-based receivers in actual systems. Therefore, if integrated all-SiGe receivers are to be considered for use in scientific radiometers, it is essential to demonstrate SiGe HBT LNAs with comparable noise figure (NF) to the InP and GaAs amplifiers which are currently used in these systems.

In this chapter, the design, optimization, and characterization of ultra-low-noise SiGe HBT amplifiers for both microwave (18.7 GHz) and millimeter-wave (*G*-band) radiometers are presented. Each of the amplifiers presented here was designed to achieve ultra-low NF with minimal power consumption to enable the use of these amplifiers in power-constrained systems.

2.2 18.7 GHz SiGe LNAs with Back-Side Etched Inductors

This section presents SiGe LNAs designed for use in 18.7 GHz radiometers for snow and ice measurement, which have been published in [3]. Proposed satellite-based snow and ice measurement concepts require hundreds of integrated and low power radiometer receivers [52], and integrated SiGe receivers would enable cost reductions and

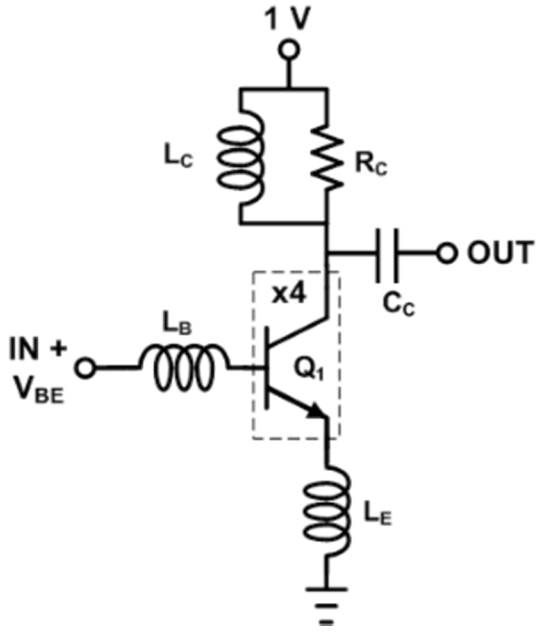

Figure 2.1: Simplified schematic of the 18.7 GHz common-emitter SiGe LNA [3] © 2014 IEEE.

improve the feasibility of such mission concepts. The LNAs presented here leverage the fastest commercially-available SiGe technology, IHP's 0.13 μm SG13G2 platform [34], to achieve unprecedented noise performance at 18.7 GHz with very low power consumption. To further improve NF, IHP's localized backside etching (LBE) module was utilized to remove the conductive silicon substrate under the on-chip inductors and suppress losses due to the conductive silicon substrate. Versions of the LNAs both with and without LBE were compared to demonstrate the performance improvements enabled by LBE.

2.2.1 Amplifier Design

Two single-stage LNAs were designed to demonstrate the potential of the SG13G2 SiGe HBTs (peak f_T/f_{max} of 300/500 GHz) for use in this application. The first LNA was designed to demonstrate the absolute minimum NF achievable using this SiGe technology. This LNA was implemented using a common-emitter (CE) topology without a lossy on-

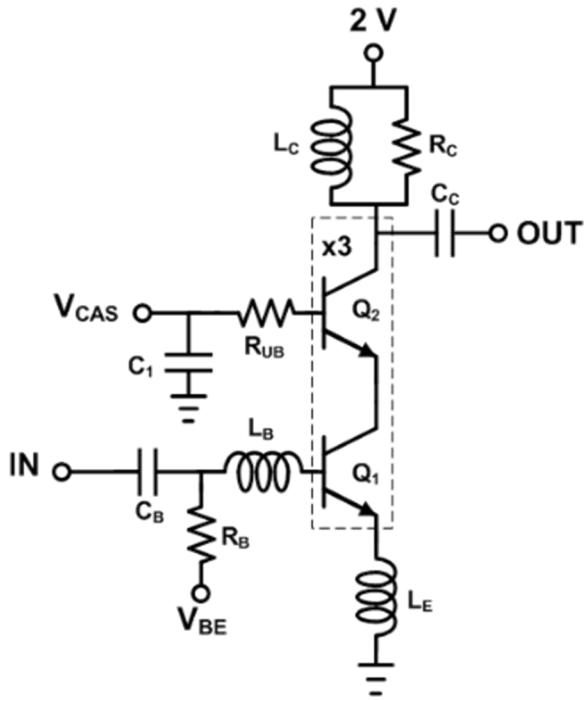

Figure 2.2: Simplified schematic of the 18.7 GHz cascode SiGe LNA [3] © 2014 IEEE.

chip input bias tee, as shown in Figure 2.1. A supply voltage of 1.0 V was chosen to minimize power dissipation while keeping the SiGe HBTs biased in forward-active mode.

The second LNA was designed to demonstrate the NF which can be achieved by a more practical LNA design which achieves higher gain and includes an on-chip bias tee. A cascode core was utilized to obtain higher gain and reverse isolation than the CE design, and a lossy input bias tee was included on chip to enable practical use. A schematic is shown in Figure 2.2. Both the supply voltage and the upper base bias voltage (V_{CAS}) were set to 2.0 V to balance gain and NF and to keep both SiGe HBTs in forward-active mode. The input biasing is injected through a large 5 kΩ resistor to minimize its loss. To ensure stable operation, a 15 Ω resistor was added in series with the base of the upper transistor to reduce the reflection coefficient at that node [53].

Both LNA designs utilized the simultaneous gain and noise matching procedure outlined in [54]. The current density for each LNA core was selected to balance NF, gain, and power dissipation, and the emitter area was scaled to set the optimum noise resistance to 50 Ω. Candidate transistor cores were laid out and parasitic extracted, and this process was iterated until sufficient performance was attained. After optimization, the CE LNA core consisted of four 0.12 μm × 0.96 μm × 5-emitter SiGe HBTs operating at a current density of 2.2 mA/μm^2. The cascode LNA core used three cascode pairs consisting of 6-emitter SiGe HBTs biased at 2.4 mA/μm^2.

Emitter degeneration inductance was utilized in each design to match the input resistance to 50 Ω and improve linearity. This inductance was implemented as a thin metal trace over the substrate. A series inductor at each CE base node resonates out the input capacitance and completes the match. Each core output was matched to 50 Ω using a shunt-L series-C network, with a shunt resistor to ensure stability. Due to the finite reverse isolation of each core, this process was iterated until sufficient matching was attained.

Particular emphasis was placed on the design of the on-chip inductors. Custom square spiral inductors were designed, and all inductors used wide signal traces where possible to minimize resistive losses. The IHP foundry's LBE module was utilized to remove the silicon substrate beneath the inductors, virtually eliminating capacitive substrate coupling and eddy current-induced losses. All inductors were EM simulated in Sonnet following the procedure in [55]. The EM-simulated quality factor (Q) for the 380 pH CE LNA input inductor with and without LBE is shown in Figure 2.3. LBE-induced Q improvements become apparent above 10 GHz, where capacitive losses become significant. At 18.7 GHz, LBE improves the Q from 18.0 to 20.5—a 14% improvement.

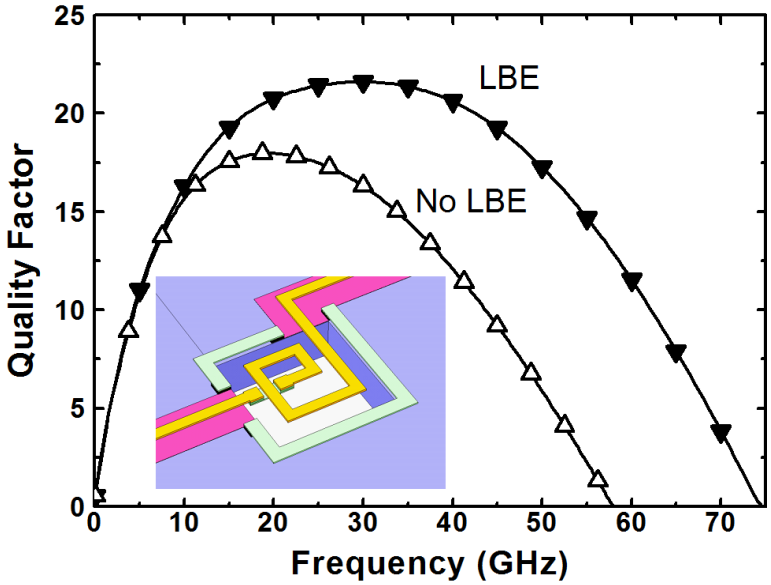

Figure 2.3: **Simulated *Q* of the 380 pH inductor used in the 18.7 GHz CE LNA, with and without LBE. The inset shows a 3-D model of the inductor [3] © 2014 IEEE.**

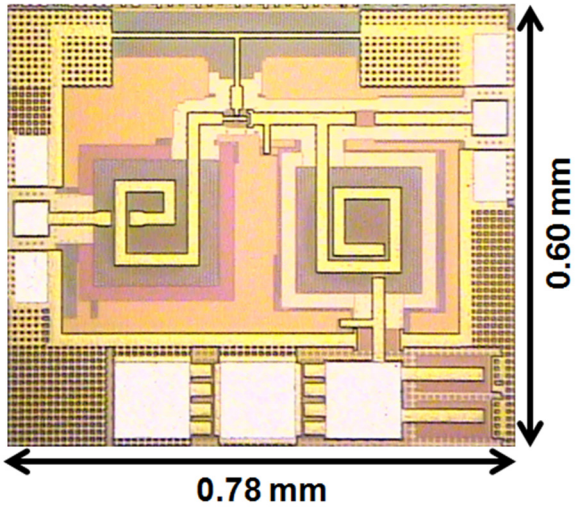

Figure 2.4: **Photograph of the 18.7 GHz CE LNA with annotated dimensions [3] © 2014 IEEE.**

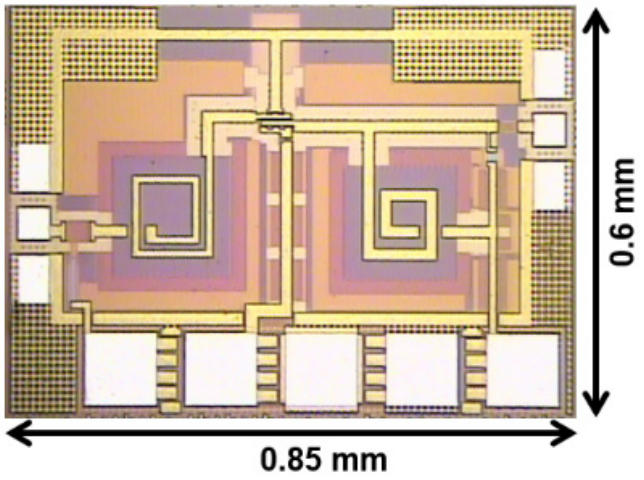

Figure 2.5: Die photograph of the 18.7 GHz cascode LNA with annotated dimensions [3] © 2014 IEEE.

2.2.2 Measurements

Each of the LNAs, both with and without LBE, was characterized on-wafer in an RF-shielded room. The measured S-parameters of the CE LNA with and without LBE are shown in Figure 2.6, along with the simulated S-parameters of the LNA with LBE. The measured S_{12} is greater than predicted by simulation, which is primarily due to incomplete modeling of the HBT substrate network. The reverse isolation of this CE LNA is inherently low due to the Miller effect, so this S_{12} change induces a frequency shift. At 18.7 GHz, the LNA with LBE has an S_{21} of 8.6 dB as compared to 8.1 dB for the LNA without LBE. Due to the relatively low gain and reverse isolation, this LNA would be most practically used as the first stage of a multi-stage LNA in a radiometer receiver.

The measured performance of the cascode LNA with and without LBE versus the simulated performance with LBE is shown in Figure 2.7. The measured S_{12} for this LNA was also greater than predicted by simulation. Cascode pairs eliminate the Miller effect and therefore have much higher reverse isolation than CE HBTs, so despite the S_{12} reduction from simulation, a much smaller frequency shift is observed in this LNA. The

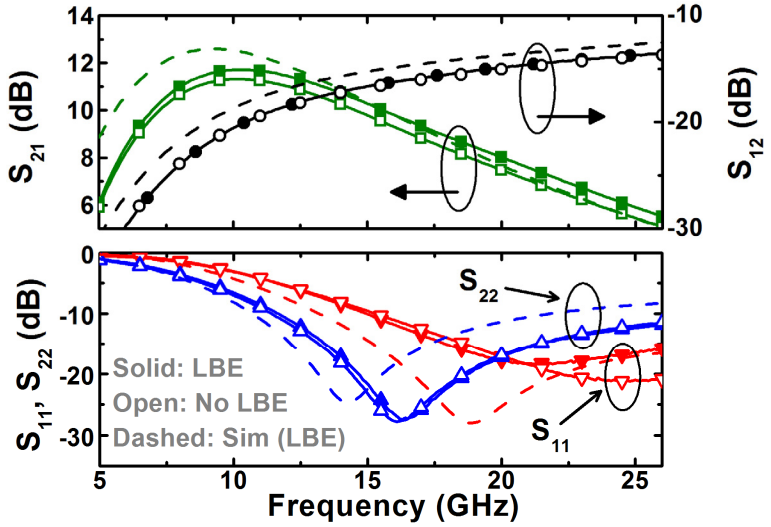

Figure 2.6: **Measured S-parameters of the CE LNA with and without LBE, along with the simulated performance with LBE [3] © 2014 IEEE.**

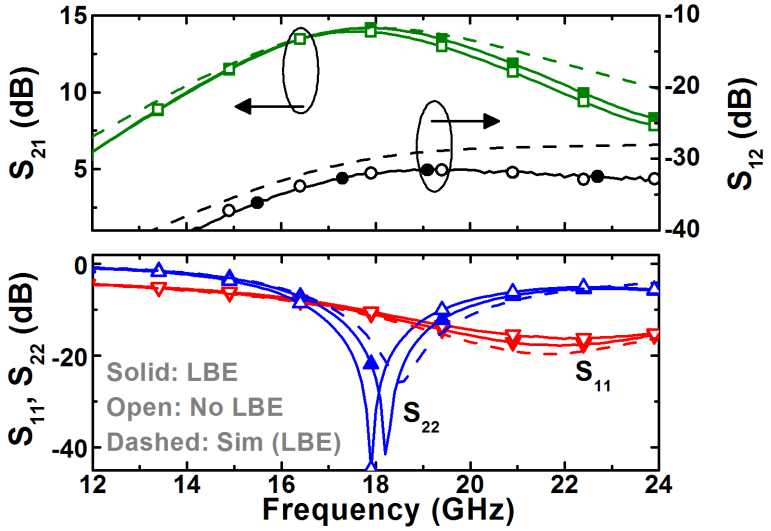

Figure 2.7: **Measured S-parameters of the cascode LNA with and without LBE, along with the simulated performance with LBE [3] © 2014 IEEE.**

return loss is greater than 12 dB at both the input and output, and the use of LBE only slightly shifts the matching. At 18.7 GHz, the S_{21} of this LNA is 14.0 dB with LBE and 13.6 dB without LBE—a gain improvement similar to that observed in the common-emitter LNA, as expected. The measured S_{21} is more narrowband than simulated, although the LNA is well-centered near 18.7 GHz.

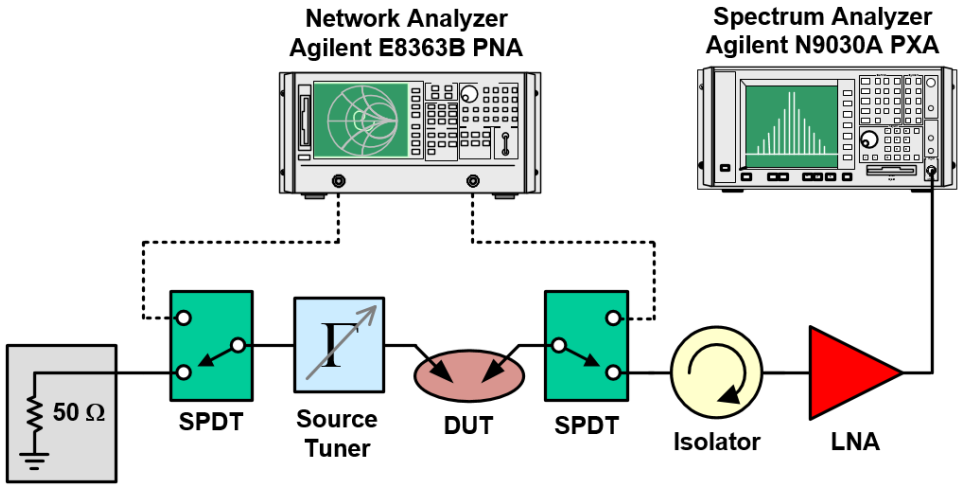

Figure 2.8: Simplified block diagram of the cold-source NF measurement setup [3] © 2014 IEEE.

The NF of the LNAs was measured on-wafer using an accurate cold-source noise parameter measurement method controlled by Focus Microwaves' Load-Pull Explorer software [56]. A block diagram of the measurement setup is shown in Figure 2.8. A matched termination at ambient temperature is used as a cold noise source, and the output noise power is measured across a narrow bandwidth using a precisely calibrated noise receiver. Great care was taken to minimize the NF of the noise receiver, which directly impacts measurement precision. The switched-in network analyzer enables accurate vector calibration of all setup losses and impedance mismatches. The LNA noise parameters were extracted from NF measurements at 22 source impedances for each frequency, from which the reported 50 Ω NF values were obtained.

The measured noise performance of both LNAs with and without LBE is shown in Figure 2.9. The data exhibits some ripple due to imperfect calibration and reflections in the measurement path; however, all measurements were highly repeatable and the data trends are accurate. We therefore conservatively estimate an NF uncertainty of ±0.1 dB. The NF of the common-emitter LNA at 18.7 GHz is 1.10 dB (84 K T_{eff}) with LBE, in comparison

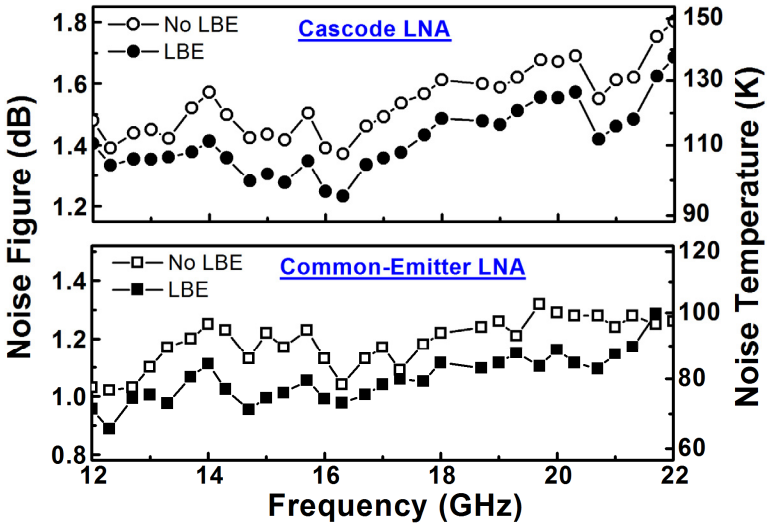

Figure 2.9: Measured noise performance of both 18.7 GHz LNAs with and without LBE [3] © 2014 IEEE.

to 1.24 dB (96 K) without LBE. The cascode LNA has a measured 18.7 GHz NF of 1.48 dB (118 K) with LBE and 1.60 dB (129 K) without LBE. LBE improves the NF and T_{eff} of these LNAs by averages of 0.12 dB and 11.0 K, respectively, across the band. While this LBE-induced NF reduction may seem small, this represents a roughly 10% reduction in linear noise temperature and is significant for radiometers (see Equation 1.1).

Although radiometers measure small input power levels, they operate in a crowded spectral environment and are often subjected to spurious RF interference. High linearity is desirable to prevent interference-induced compression and intermodulation distortion. The two-tone linearity of each LNA was measured at 18.7 GHz with an 8 MHz offset, and the results for each LNA with LBE are shown in Figure 2.10. The extrapolated input- and output-referred third-order intercept points (IIP_3 and OIP_3) are +8.5 dBm and +17.1 dBm, respectively, for the CE LNA and -2.4 dBm and +11.5 dBm for the cascode LNA. Without LBE, the measured OIP_3 is +16.4 dBm for the CE LNA and +11.2 dBm for the cascode LNA. These values are sufficiently high for typical radiometers.

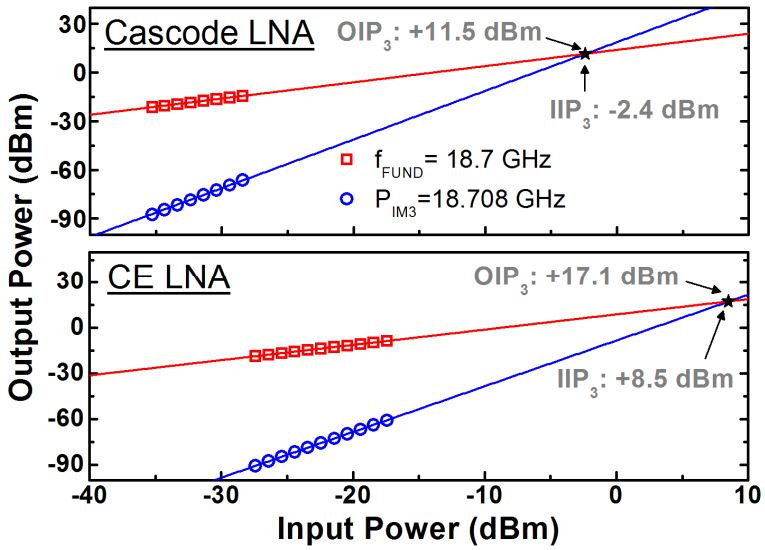

Figure 2.10: Measured two-tone linearity of both 18.7 GHz LNAs with LBE [3] © 2014 IEEE.

Table 2.1: Comparison to similar low-noise and low-power microwave LNAs [3] © 2014 IEEE.

Ref.	Frequency (GHz)	NF (dB)	Gain (dB)	P_{DC} (mW)	OIP_3 (dBm)	Technology
This	18.7	1.10	8.6	5.0	17.1	500 GHz SiGe HBT
This[1]	18.7	1.48	13.9	10.0	11.5	500 GHz SiGe HBT
[54]	10	1.36	19.5	15	20.3	285 GHz SiGe HBT
[57]	10	1.98	10	2	10	285 GHz SiGe HBT
[58][2]	33	2.9	23.5	11	4	285 GHz SiGe HBT
[59]	24	3.2	13	4.1	8	40 nm CMOS
[60][1]	10	1.60	8.7	0.60	-	0.1 µm InP pHEMT
[61][2]	16	1.06	38	16	-	70 nm GaAs mHEMT

[1]Full input bias tee included on-chip [2]Multi-stage design

The performance of these LNAs is compared with other state-of-the-art ultra-low noise and low-power LNAs in Table 2.1. It should be noted that many of the listed results did not utilize a lossy on-chip input bias tee unlike the cascode LNA presented here. To the authors' best knowledge, these LNAs have the lowest NF of all published silicon-based LNAs at this frequency and are competitive with the best III-V results.

2.2.3 Summary

This section presented the design of LNAs for 18.7 GHz snow and ice sensing radiometers using a 0.5 THz SiGe technology. These LNAs achieve record-setting NF for a silicon-based technology at this frequency, with very low power consumption and sufficient linearity for radiometers. The results show the ability of LBE to reduce inductor losses and improve circuit performance. At 18.7 GHz, LBE improved the gain of the two LNAs by 0.4/0.5 dB, the NF by 0.12/0.13 dB, and the OIP3 by 0.3/0.7 dB. These results clearly indicate that SiGe technologies are well-suited for implementing receivers for performance-constrained radiometers at microwave frequencies.

2.3 Design and On-Wafer Characterization of G-band SiGe LNAs

The results of the previous section show that SiGe HBT LNAs attain competitive performance to the best demonstrated III-V amplifiers at microwave frequencies. At these frequencies, however, LNA technologies are numerous and mature. SiGe receivers are most attractive for use in microwave radiometer systems which require high integration or a large number of identical low-noise and low-power receivers. However, at millimeter-wave frequencies, only a few III-V technologies which can achieve low LNA NF exist, including InP HEMTs from Northrop Grumman Aerospace Systems, [43], GaAs mHEMTs from Fraunhofer IAF [42], and InP HBTs from Teledyne Scientific [41]. These are small-volume technologies which are not readily accessible, whereas SiGe technologies are well-suited for scale production and are easily accessible through MPW services, and unlike the aforementioned millimeter-wave III-V technologies, are well-suited for receiver-on-chip integration. Maximizing on-chip integration at millimeter-wave frequencies is highly

desirable, as millimeter-wave chip-to-package transitions are typically quite lossy and can be large when typical split-block waveguide packages are utilized.

In this section, the design and on-wafer characterization of two *G*-band SiGe HBT LNAs for 183 GHz humidity-sounding radiometers is presented. This work has been published in [4]. The two amplifiers are separately implemented using exclusively cascode cores and exclusively CE HBTs to determine which transistor configuration yields lower NF and better overall performance when exclusively used to design a stable multi-stage *G*-band SiGe HBT LNA. This section also presents a novel blackbody noise source implementation for on-wafer Y-factor NF measurements which leverages the near-transparency of expanded polystyrene (EPS) foam to reduce the length of waveguide needed to transition between the antenna and the input probe, which significantly reduces the sensitivity of the measurements to noise fluctuations. A method to perform gain compression measurements using a millimeter-wave vector network analyzer (VNA) extender as a variable signal source is also presented in detail.

2.3.1 Design Technology and Layout Considerations

The *G*-band SiGe LNAs are designed and manufactured in the IHP SG13G2 platform to achieve the best attainable NF at these frequencies using SiGe HBTs. The all-aluminum back-end-of-line (BEOL) of the SG13G2 process features five thin metallization layers (M1 through M5) and two thick layers (TM1 and TM2). Metal-insulator-metal (MIM) capacitors above M5 with a density of 1.5 fF/μm^2 are available, along with three polysilicon resistor variants.

The first step in the design process is to select the layout scheme. M2 is chosen as the ground plane to enable the routing of shielded bias lines on M1. Microstrip lines with

TM2 trace widths between 2 μm and 20 μm were EM-simulated using Sonnet and the results for each trace width were calibrated to the Agilent Advanced Design System (ADS) two-terminal physical transmission line component to create length-scalable microstrip models that enabled rapid design of matching elements. Numerous layout components over M2 such as mitered bends, series capacitors, decoupling capacitors, and signal bondpads were also EM-simulated prior to the schematic design process to minimize the need for further EM simulations that disrupt the schematic-level design flow.

When designing at millimeter-wave frequencies, the SiGe HBT input and output via transition parasitics must be considered during all stages of the design process. A transition between M1 and TM2 compatible with multiple SiGe HBT sizes is designed using a 15 × 15 arrays of vias between M1 and M5 to obtain a near-optimal balance between f_T and f_{max} at the TM2 top metal layer [36,37]. The transition is designed for a wide separation of over 5 μm between the input-side and output-side transitions. Coupling between neighboring transitions is found to be negligible due to this wide separation and is therefore not considered here. Figure 2.11 shows the layout of the via transition along with a pi-model fitted to the EM-simulated results from 110–220 GHz, and Figure 2.12 shows the close agreement between the EM-simulated performance and the calculated performance of the lumped-element model. The series resistance of 0.72 Ω is lower than that reported in [62], where narrow arrays are used.

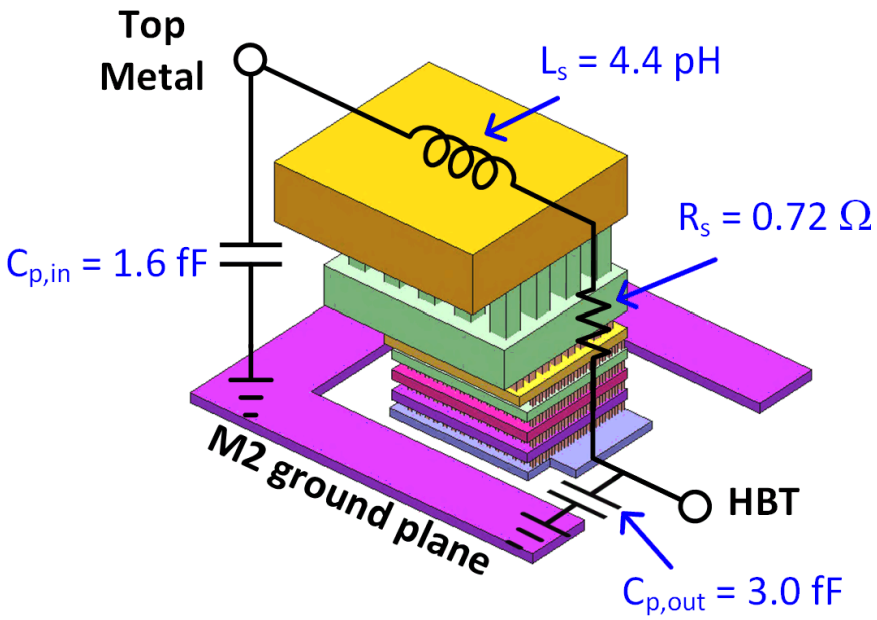

Figure 2.11: **Three-dimensional model of the input/output via transition designed for the amplifying SiGe HBTs, showing parasitic element values fitted to the 110–220 GHz EM-simulation results [4] © 2016 IEEE.**

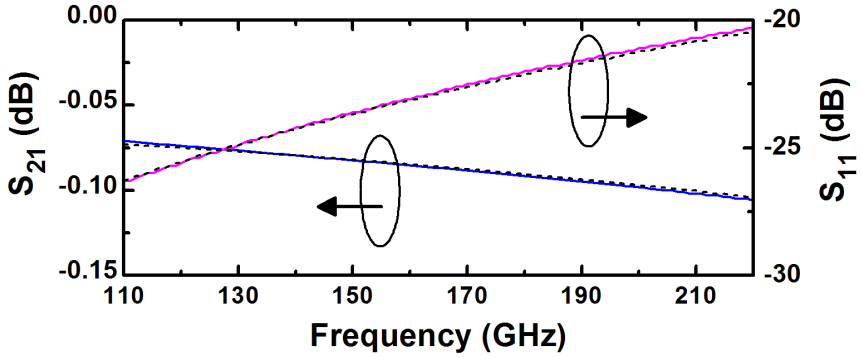

Figure 2.12: **Calculated performance of the lumped-element via transition model (dashed) compared to the EM-simulated performance (solid) [4] © 2016 IEEE.**

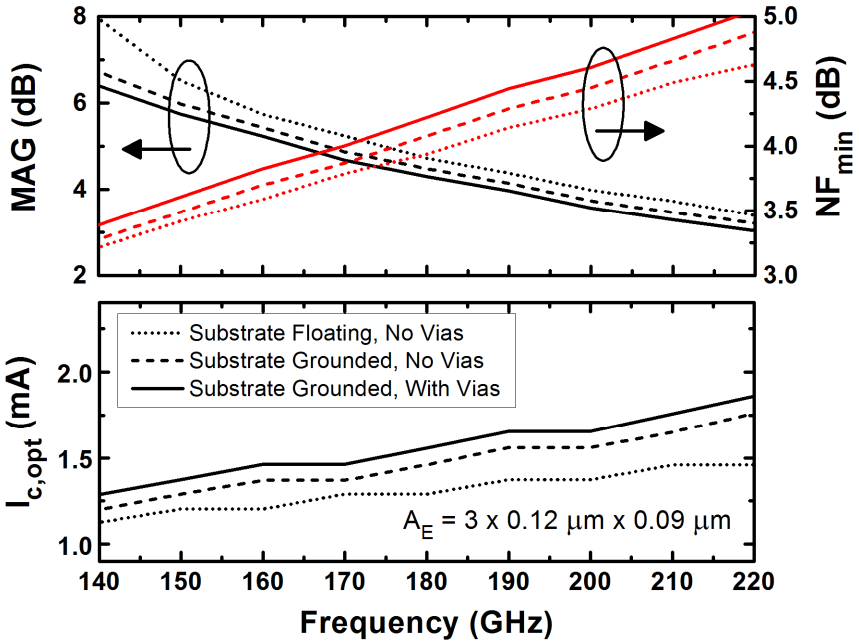

Figure 2.13: Simulated *MAG* and NF_{min} of a CE SG13G2 HBT biased at $I_{c,opt}$ across *G*-band, showing the impact of the substrate network and via transitions on the transistor performance [4] © 2016 IEEE.

The impact of the parasitic substrate network can be significant in millimeter-wave LNAs. The SG13G2 SiGe HBTs are not surrounded by deep trench isolation, making them sensitive to the placement of substrate contacts. Placing substrate contacts far from the SiGe HBTs ensures a high impedance collector-to-substrate loss path, but such a path is difficult to model at high frequencies. Surrounding the SiGe HBT with grounded substrate contacts increases the loss through the substrate, but simplifies modeling.

To illustrate the substantial impact of these parasitics on the attainable noise performance of a CE SiGe HBT, Figure 2.13 shows the simulated maximum available gain (*MAG*) and minimum NF (NF_{min}) at the optimal noise measure bias current ($I_{c,opt}$) across 140–220 GHz. As frequency increases, the reduced gain due to these parasitics necessitates an increased bias current, with higher associated NF_{min}, to minimize the cascaded noise contribution. At 180 GHz, grounding the substrate reduces the optimal *MAG* of 4.7 dB to

4.5 dB and increases $I_{c,opt}$ from 1.3 mA to 1.5 mA and the associated NF_{min} from 3.9 dB to 4.1 dB. Despite this reduced performance, the local substrate is grounded in these designs to maximize simulation accuracy at the expense of performance. The via transitions further reduce the *MAG* to 4.3 dB while increasing the $I_{c,opt}$ to 1.6 mA and the NF_{min} to 4.2 dB. The impacts of the substrate connection and via transitions in the *G*-band are quite significant, and should be considered from the very beginning of the design process.

2.3.2 LNA Design

Two multi-stage amplifiers were designed—one using only cascode-configured SiGe HBTs and the other using only CE SiGe HBTs. Cascode pairs achieve higher gain and reverse isolation than CE SiGe HBTs, but at millimeter-wave frequencies, the noise of the common-base (CB) transistor significantly increases the NF versus that of a CE SiGe HBT. Furthermore, cascode pairs often require lossy stabilizing networks or impedance mismatching to ensure stable operation. CE SiGe HBTs are generally more stable at millimeter-wave frequencies, but the gain of each transistor is low. The goal of these designs is to explore which transistor configuration yields lower NF and better overall performance when exclusively used in a multi-stage *G*-band SiGe HBT LNA.

2.3.2.1 Cascode Amplifier

In order to minimize the NF of the cascode LNA, the size of the CE transconductor HBT in the input stage was selected first to balance gain and noise matching. The emitter length of the SG13G2 SiGe HBTs is not variable, so the number of emitter stripes (N_E) were varied to explore this tradeoff. Three emitter stripes were found to be optimal.

Next, the sizing of the CB SiGe HBT and the bias current were co-selected. Figure 2.14 shows the effect of the CB SiGe HBT sizing on the associated gain and NF_{min}

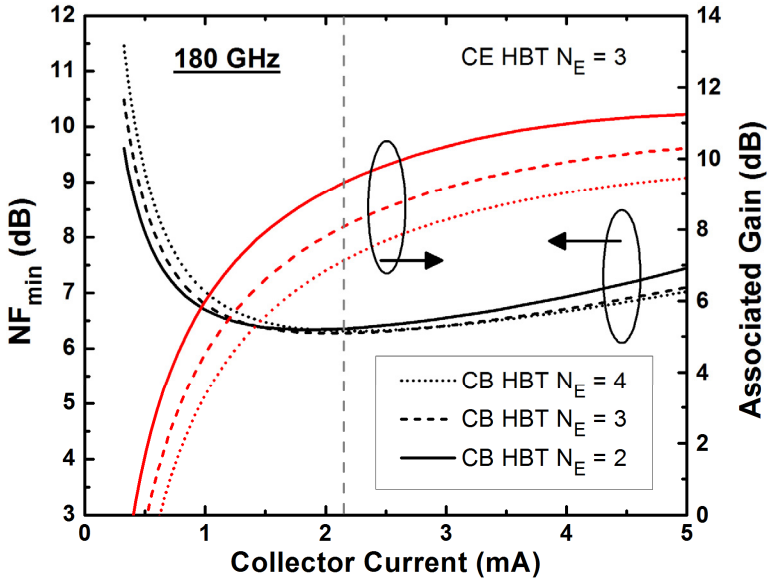

Figure 2.14: Simulated NF_{min} and associated gain of a SiGe HBT cascode at 180 GHz, showing that reducing the emitter area of the common-base (CB) HBT increases the gain by 1 dB while only slightly increasing NF_{min} [4] © 2016 IEEE.

of the first-stage cascode at 180 GHz. When a two-emitter CB SiGe HBT is used and the cascode is biased at the selected current of 2.15 mA, the three-emitter CE SiGe HBT is operated at 38 percent of peak f_{max} while the CB SiGe HBT is operated at 57 percent of peak f_{max}. This increases the associated gain by 1.2 dB versus that of a matched three-emitter cascode, whereas the NF_{min} increases by less than 0.1 dB.

The optimal gain and noise impedances of the first stage of the cascode LNA were evaluated to determine if inductive emitter degeneration was necessary to sufficiently balance the gain, NF, and input matching. Figure 2.15 shows that the optimal noise impedance Γ_{opt} and conjugate input impedance Z_{in}^{*} of the input stage cascode transistor core converge as frequency increases. At 180 GHz, matching directly to Γ_{opt} trades off only 0.5 dB of available gain (G_A). This tradeoff was deemed acceptable, so the emitter of the CE SiGe HBT was directly connected to the ground plane in layout.

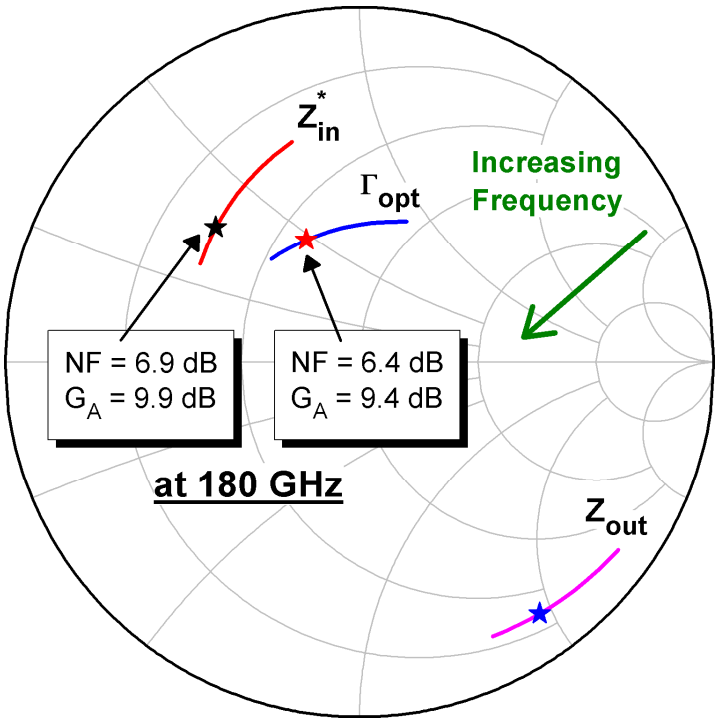

Figure 2.15: Simulated Z_{in}^*, Γ_{opt}, and Z_{out} of the transistor core of the input stage of the cascode LNA from 110–220 GHz, showing that Z_{in}^* and Γ_{opt} converge as frequency increases [4] © 2016 IEEE. The values at 180 GHz are starred.

Figure 2.16 shows a simplified schematic of the full three-stage LNA. A 2.0 V bias (*VUB*) was applied to the base of each CB SiGe HBT through a 28 Ω resistor and a 200 fF decoupling capacitor to prevent any oscillations at these sensitive nodes [53]. Biasing was applied to the base of each CE SiGe HBT through a 2.5 kΩ polysilicon resistor fed into the M1 level of the via transition at each CE SiGe HBT input. The input was matched using a series microstrip line and the shunt capacitance provided by the input signal pad over the M2 ground plane.

The SiGe HBTs in the second and third stages were each sized to match the input resistance to the output resistance of the preceding cascode. Interstage matching networks were implemented using series microstrip lines, MIM capacitors, and shunt stubs

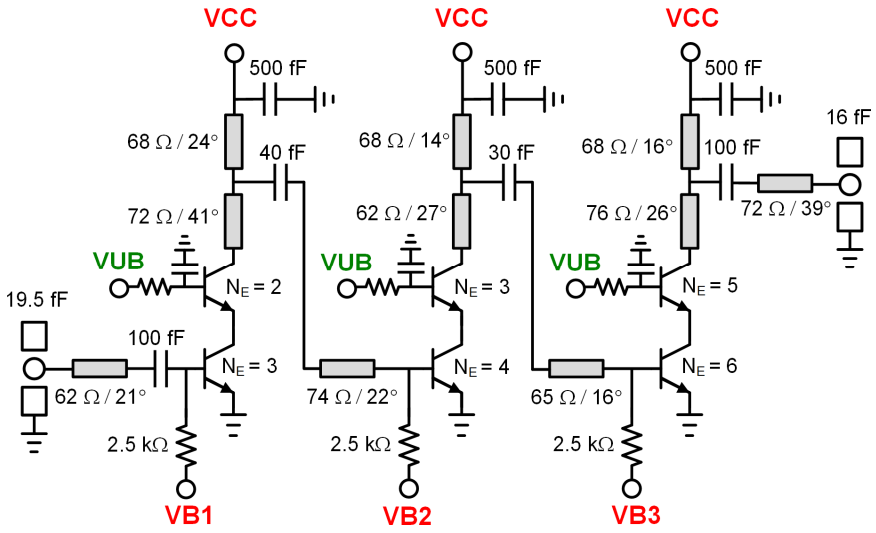

Figure 2.16: Simplified schematic of the full three-stage cascode *G*-band LNA [4] © 2016 IEEE.

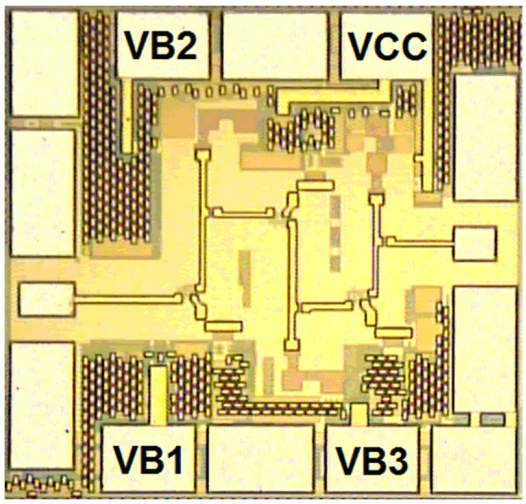

Figure 2.17: Die photograph of the fabricated three-stage *G*-band cascode LNA. The size of the chip, including bondpads, is 0.6 mm × 0.57 mm [4] © 2016 IEEE.

terminated by 500 fF MIM capacitors. The collector bias *VCC* is supplied to each shunt stub through small resistors and decoupling capacitors to ensure stability at low frequencies. On-chip resistor dividers generate the *VUB* for each stage and consume 0.5 mA each.

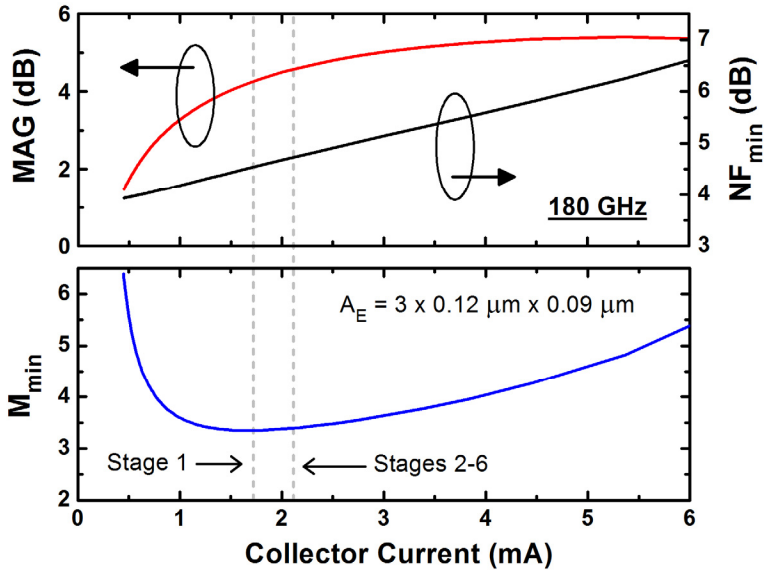

Figure 2.18: Simulated *MAG*, NF_{min}, and M_{min} at 180 GHz of a CE SiGe HBT with via transitions and resistive input biasing, showing the bias currents selected for each LNA stage [4] © 2016 IEEE.

A photograph of the fabricated LNA is shown in Figure 2.17. The LNA has a simulated 3-dB bandwidth of 136–196 GHz with matching centered at 180 GHz and a peak gain of over 24 dB. The simulated NF ranges between 7.4–8.8 dB across the band. The power consumption is 28 mW from a 2.2 V supply.

2.3.2.2 Common-Emitter Amplifier

The first stage of the CE LNA was designed using three-emitter CE SiGe HBTs, which were again found to provide the best balance between gain and noise matching. The low gain of the CE SiGe HBTs in *G*-band necessitates a multi-stage amplifier design, so the amplifying stages were designed to optimize the noise measure *M* and therefore minimize the cascaded NF of the amplifier [63,64]. Figure 2.18 shows the simulated *MAG*, NF_{min}, and minimum noise measure M_{min} versus bias current for the three-emitter CE SiGe HBT with via transitions and resistive input biasing at 180 GHz. The first stage was biased at 1.7 mA where the *MAG* is 4.2 dB, the NF_{min} is 4.5 dB, and the M_{min} is 3.35. This low

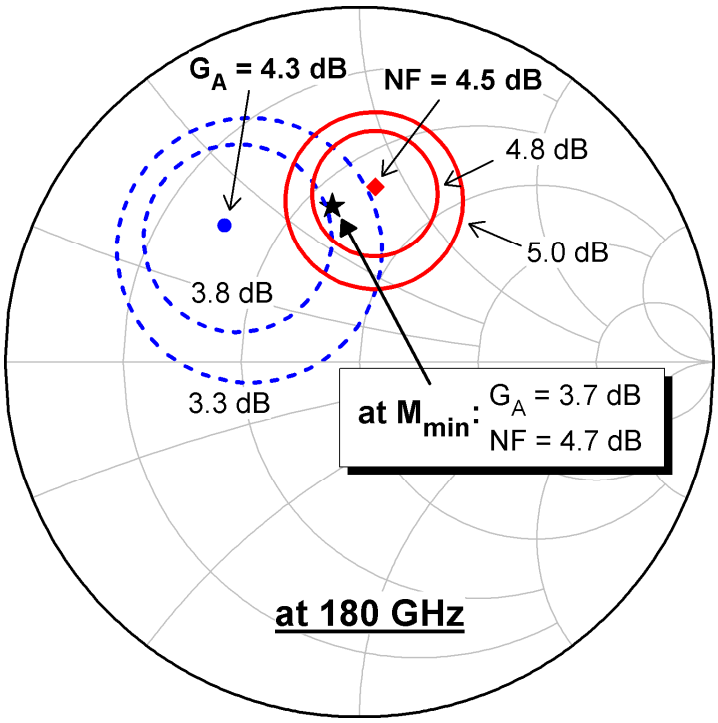

Figure 2.19: Simulated 180 GHz available gain and noise circles of the first stage transistor core of the CE LNA biased at 1.7 mA, showing the selected matching impedance for minimum noise measure M_{min} [4] © 2016 IEEE.

first-stage gain only partially suppresses the noise of the subsequent CE amplifying stages, so the noise contributions of the following stages were considered throughout the design process. All subsequent amplifying stages were also designed using three-emitter CE SiGe HBTs to optimally balance their gain and noise matching and were biased at 2.1 mA to obtain 0.4 dB of additional *MAG* versus the first stage with a M_{min} penalty of less than 0.1 for each stage.

Figure 2.19 shows the 180 GHz NF and G_A circles of the first stage transistor core of the CE LNA. The input match was selected for M_{min} [63]. With this optimal match, the available gain of the input stage is 3.7 dB, with an NF of 4.7 dB. Inductive emitter degeneration was considered to reduce the tradeoff between gain and noise, but was not used to avoid increasing M_{min} due to reduced gain and via transition losses on the emitter.

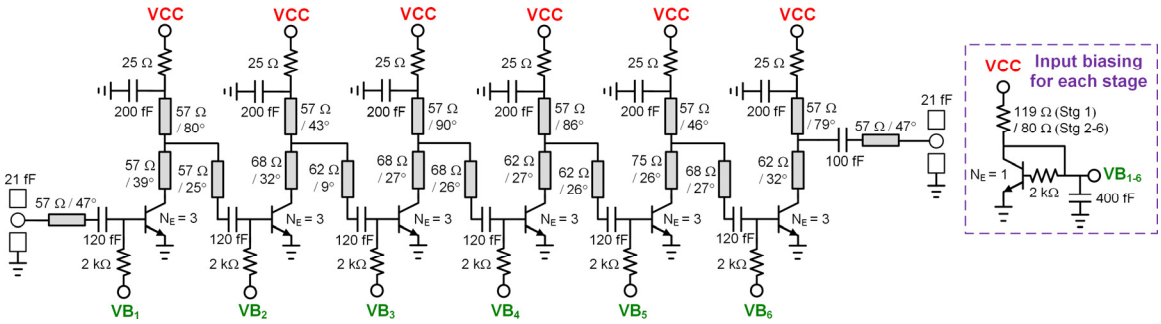

Figure 2.20: Simplified schematic of the six-stage *G*-band CE LNA [4] © 2016 IEEE.

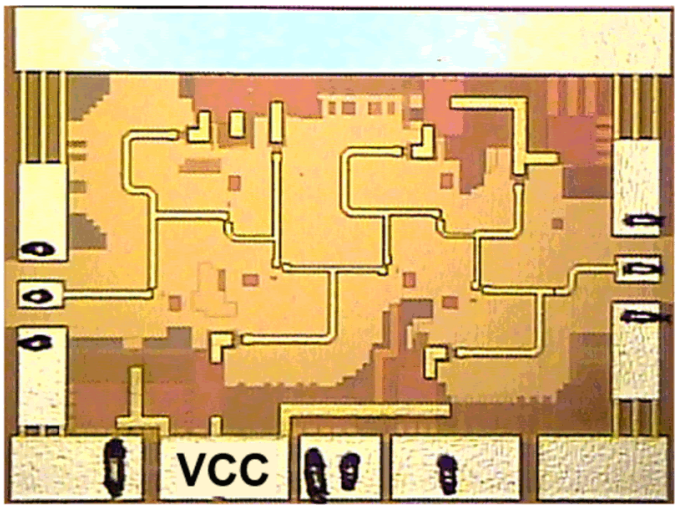

Figure 2.21: Die photograph of the fabricated six-stage *G*-band CE LNA. The size of the chip, including bondpads, is 1.02 mm × 0.75 mm [4] © 2016 IEEE.

Figure 2.20 shows a schematic of the full six-stage LNA. On-chip current mirrors supply the input biasing for each stage. A 120 fF DC-blocking MIM capacitor was integrated into the input via transition to each amplifying SiGe HBT, and interstage matching was implemented using on-chip microstrip lines. Both the input and output matching incorporate the shunt capacitance from the signal bondpads. The matching networks and gain have a wideband response, so the shunt stubs were terminated using 200 fF shunt capacitors and 25 Ω series resistors that present sufficiently resistive impedances in the lower frequency range to ensure stable operation.

A photograph of the fabricated CE LNA is shown in Figure 2.21. The amplifier has a simulated optimally matched bandwidth (return loss ≥ 10 dB) of 164–191 GHz. Across this band the simulated gain is 21–22 dB and the NF is 7.4–7.7 dB. The power consumption is 16.1 mW from a 0.97 V supply.

2.3.3 S-Parameter Measurement

The S-parameters of the amplifiers were measured on-chip using an Agilent E8361C network analyzer with an N5260A millimeter-wave controller and frequency extenders. Measurements were first performed from 110–180 GHz using two OML V06VNA2-T/R extenders along with Cascade Microtech i170 Infinity waveguide probes. The input-side OML module contains a variable waveguide attenuator before the coupler, which was adjusted to prevent gain compression of the LNAs. S_{11} and S_{21} were separately measured across *G*-band using a V05VNA1-T/R module on the input and a receive-only V05VNA1-T module on the output, along with 75 μm pitch GGB Model 220 Picoprobes. The G-band measurements were performed using a 10 dB waveguide attenuator on the input to prevent unintended gain compression of the LNAs, and although on-wafer calibrations were performed with this attenuator in place, the measured *G*-band S_{11} magnitudes are overly optimistic and have low dynamic range (especially near 147 and 188 GHz). The G-band data are useful for validating the 110–180 GHz results, however.

Figure 2.22 shows the measured versus simulated S-parameters of the cascode LNA. The S_{21} response was more narrowband than simulated, and the center frequency was shifted down to 158 GHz where the peak gain is 24.0 dB. The S_{22} peak shifted 10 percent down in frequency and S_{11} was degraded from simulation, ranging between -3.8 dB and -6.8 dB across the 3-dB bandwidth of 137–177 GHz. The reduced

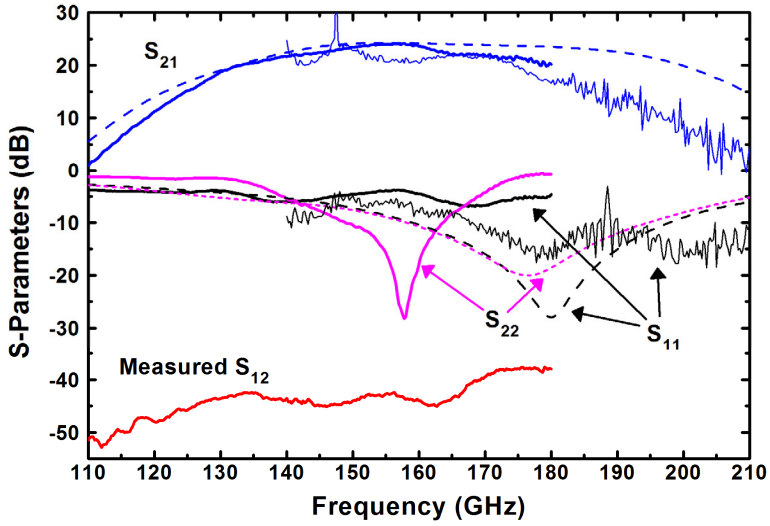

Figure 2.22: Measured (solid) and simulated (dashed) S-parameters of the *G*-band cascode LNA [4] © 2016 IEEE.

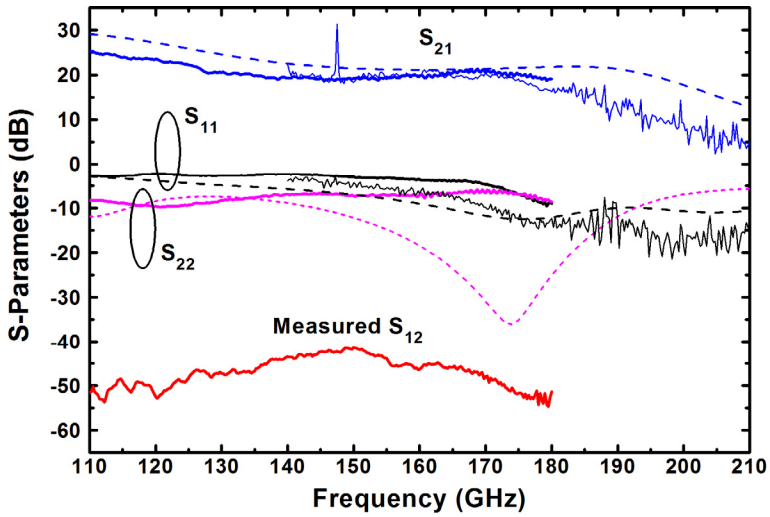

Figure 2.23: Measured (solid) and simulated (dashed) S-parameters of the *G*-band CE LNA [4] © 2016 IEEE.

bandwidth versus simulation and the shifted output match indicate that either or both of the SiGe HBT collector-substrate and collector-base capacitances are larger than modeled. The stability was evaluated from the measured 110–180 GHz results using the μ-factor test, and the amplifier was unconditionally stable up to 173 GHz and stable at 50 Ω across all of

110–180 GHz. The G-band measurements contain calibration artifacts at 147 and 188 GHz, but indicate that the LNA has more than 10 dB of gain up to 197 GHz.

The measured versus simulated S-parameters of the CE LNA are shown in Figure 2.23. The S_{21} peak in the desired band was 21.0 dB at 171 GHz, and dropped to 17.2 dB at 183 GHz. Both the input and output return losses are better than 6.0 dB above 173 GHz, as indicated by the 110–180 GHz measurements. The μ-factors calculated from the 110–180 GHz data indicate unconditional stability across that range. The measured *G*-band S-parameters again contain measurement artifacts near 147 and 188 GHz and show that the gain is greater than 10 dB up to 196 GHz.

Both amplifiers exhibit similar performance shifts from simulation, which are potentially caused by discrepancies between the physical versus EM-simulated passive elements as observed in [62]. Another potential error source is insufficient grounding of the silicon substrate surrounding the SiGe HBTs. Each SiGe HBT amplifier core is closely surrounded by a 2 μm wide ring of vias between the M2 ground plane and the substrate, which may not be sufficiently wide to completely ground the local silicon. Furthermore, the foundry-provided VBIC models of the SiGe HBTs were only validated up to 50 GHz and the accuracy of these models in the *G*-band is uncertain.

2.3.4 On-Wafer Noise Figure Measurement

2.3.4.1 Blackbody Noise Source Design

NF measurements were performed using the Y-factor method. To the best of the authors' knowledge, there are no commercially-available active noise sources above 170 GHz, so hot and cold *G*-band noise was generated using physical blackbody noise sources following [65] and [66]. Hot and cold noise powers were presented to the input of

each LNA by pointing a horn antenna at two sheets of ECCOSORB® HR-25 millimeter-wave absorber foam [67], with one sheet at ambient temperature and the other immersed in liquid nitrogen (LN_2 = 77.3 K).

Blackbody noise sources in laboratories are often implemented by pointing an antenna downwards into a LN_2-filled metal bucket containing absorber. This approach is not optimal for use with on-wafer measurements. The constrained environment of typical probe station setups necessitates long lengths of lossy waveguide to transition between the probe and the antenna, especially because it must be possible to switch between hot and cold noise sources without altering the RF probe contact. The ratio between the effective hot and cold noise powers, $P_{\mathrm{H,eff}}$ and $P_{\mathrm{C,eff}}$, presented to the input of the on-wafer device under test (DUT), assuming perfect matching and antenna efficiency, is given by

$$\frac{P_{\mathrm{H,eff}}}{P_{\mathrm{C,eff}}} = \frac{T_{\mathrm{amb}}}{\frac{77.3\ \mathrm{K}}{L} + \left(1 - \frac{1}{L}\right) T_{\mathrm{amb}}} \tag{2.1}$$

where T_{amb} is the ambient temperature (300 K) and L is the combined IL of the wafer probe and the waveguide sections between the probe and the antenna. Input-side ILs significantly reduce the noise power ratio at the DUT input, and the noise added by the DUT further reduces this ratio at the DUT output which results in a small Y-factor (< 0.3 dB in these measurements) which is challenging to accurately measure due to random noise fluctuations. To minimize the sensitivity to these random fluctuations, it is essential to construct and position the blackbody noise sources in a way that minimizes the length of lossy waveguide required to transition from the input probe to the antenna pointing at the LN_2-immersed absorber.

The novel blackbody noise source implementation designed for these measurements enables short waveguide lengths between the wafer probe and the antenna

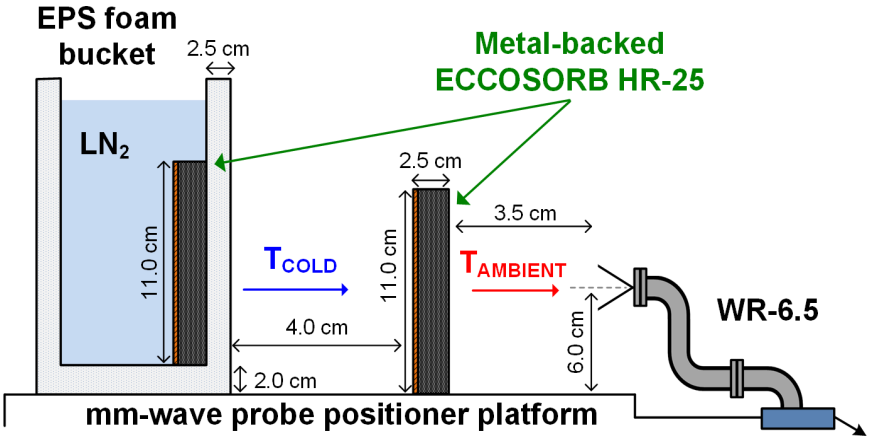

Figure 2.24: Diagram of the blackbody noise source configuration for the WR-6.5 NF measurement setup. The lightweight sheet of ambient HR-25 is removed and replaced to perform cold and hot measurements, respectively. The length of each HR-25 sheet is 15.5 cm [4] © 2016 IEEE.

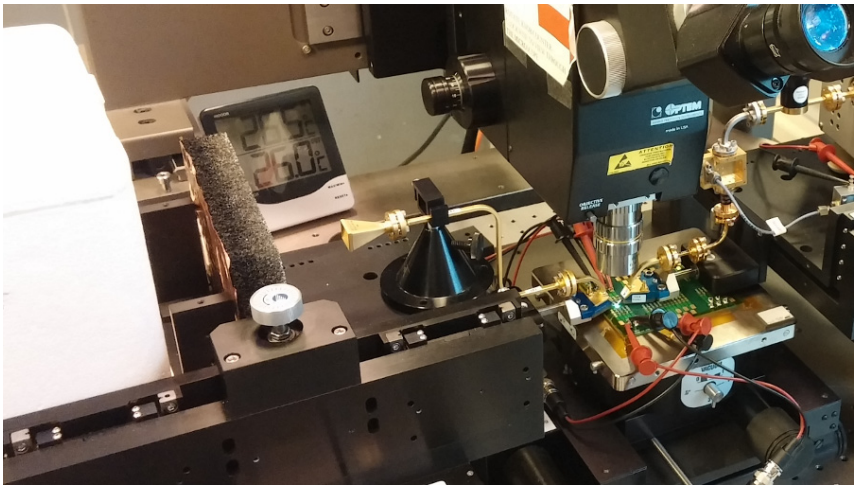

Figure 2.25: Photograph of the blackbody noise source configuration for the WR-6.5 NF measurement setup [4] © 2016 IEEE.

in a low-cost and simple way by leveraging the millimeter-wave optical properties of EPS foam. Due to equipment constraints, two separate configurations were used. The first configuration utilized entirely WR-6.5 components and was used to perform NF measurements from 145–176 GHz. A diagram of the WR-6.5 configuration is shown in Figure 2.24, and a photograph is shown in Figure 2.25. A sheet of metal-backed HR-25

was pressed against the inside wall of a bucket made of low-density (19.5 g/L) EPS foam, which is nearly transparent up to submillimeter-wave frequencies [68]. The LN_2-filled bucket was placed directly on the open platform probe positioner and the target was viewed through the side wall of the bucket by a 24 dBi rectangular horn antenna (Quinstar QWH-DPRR00). A fan continuously blew air on the viewing wall of the bucket during measurement to prevent the buildup of condensation, which would scatter the emitted cold noise power. The ambient sheet of HR-25 which served as the hot target is lightweight and could be placed on the positioner platform in front of the cold target while probed down without altering the probe contact. With this target configuration only a single E-plane waveguide S-bend was required to transition between the antenna and probe. The mean IL of this WR-6.5 S-bend, determined by terminating the bend with a waveguide short and dividing the measured return loss by two, is 1.2 dB across 145–176 GHz.

A separate configuration was used for 170–210 GHz measurements and utilized entirely WR-5.1 components. The measured mean IL of the available WR-5.1 S-bend was 2.2 dB across this band, which was deemed unacceptably high for these measurements. Therefore, a modified noise source configuration was utilized for the WR-5.1 measurements as shown in Figure 2.26 and Figure 2.27. The cold target was modified for viewing through the bottom of an EPS bucket, and the S-bend was replaced with a short 90° WR-5.1 E-plane bend which has a measured mean insertion loss of only 0.6 dB across 170–210 GHz. During measurement, the microscope was moved away from the DUT and the noise targets were manually held a short distance above the horn to ensure that the emitted radiation from the noise targets was the only radiation observed by the main lobe of the 22 dBi conical horn antenna (Virginia Diodes WR5.1CH).

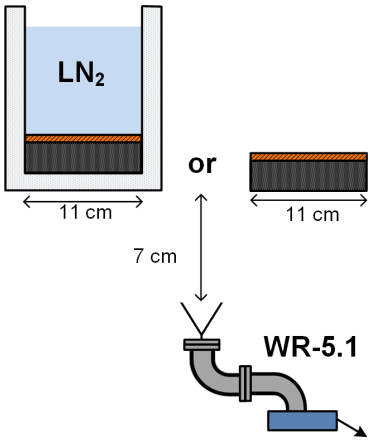

Figure 2.26: Diagram of the blackbody noise source configuration for the WR-5.1 NF measurement setup. The blackbody noise sources were manually held above the horn during measurement [4] © 2016 IEEE.

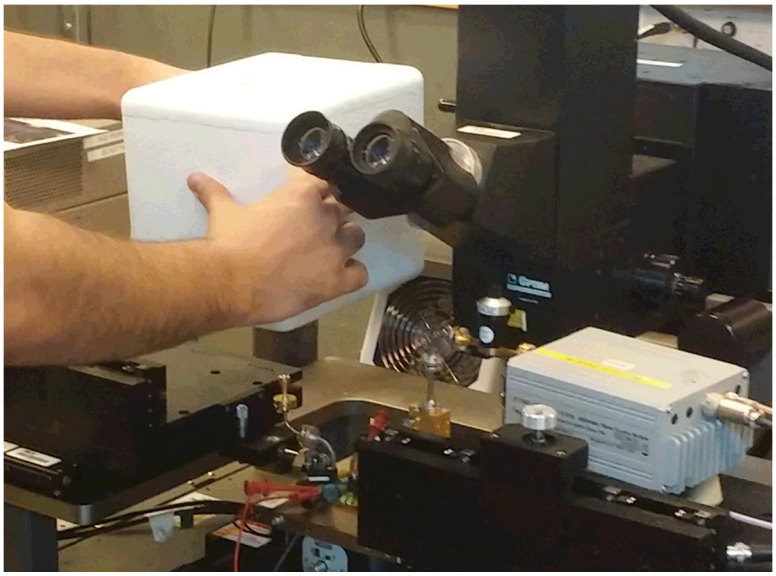

Figure 2.27: Photograph of the WR-5.1 NF measurement setup [4] © 2016 IEEE.

2.3.4.2 Probe Loss Measurements

Both pairs of WR-6.5 and WR-5.1 probes were characterized by calibrating the network analyzer to the waveguide input of the probe, measuring the S_{11} when probed on known on-wafer open, short, and load structures, and extracting the two-port S-parameters of the probe from these results using Focus Microwaves' Load-Pull Explorer software. The extracted S-parameters of the input-side wafer probes are shown in Figure 2.28. The

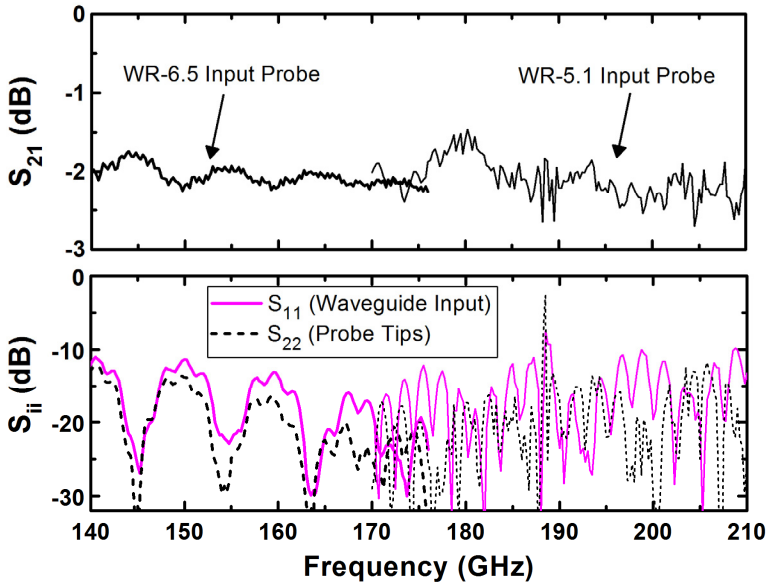

Figure 2.28: Measured S-parameters of the input-side wafer probes used for *G*-band NF measurements [4] © 2016 IEEE.

measured S_{21} ranges between -1.75 and -2.25 dB for the WR-6.5 probe and between -1.46 and -2.71 dB for the WR-5.1 probe. The total mean input fixture losses were 3.2 dB for the WR-6.5 setup and 2.7 dB for the WR-5.1 setup, resulting in on-wafer input noise power ratios of 1.9 dB and 2.2 dB, respectively. Neither of the input probes were ideally matched, making the noise measurements sensitive to the return losses of the LNAs. The measured frequency-dependent ILs were used to correct for the fixture losses, however no corrections were made for impedance mismatches.

2.3.4.3 Noise Measurements

A diagram of the NF measurement setup is shown in Figure 2.29. The double-sideband receiver consists of a Virginia Diodes WR-5.1 subharmonic mixer followed by an RF Bay LNA-700 IF amplifier with a nominal gain of 40 dB and NF of 1 dB at the fixed IF of 350 MHz. Filtering, power detection, and integration were performed by an Agilent E4446A PSA spectrum analyzer. Each noise power measurement at each frequency was

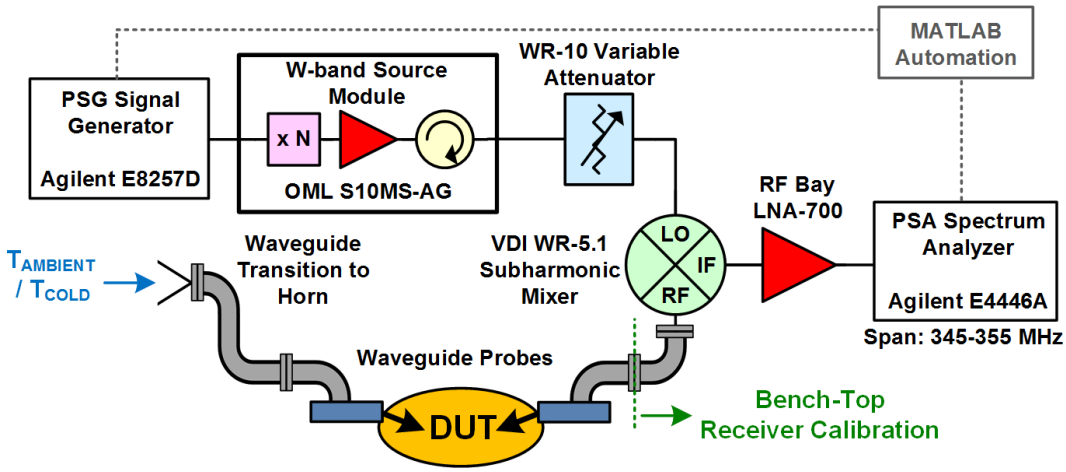

Figure 2.29: Diagram of the on-wafer Y-factor NF measurement setup [4] © 2016 IEEE.

integrated across the 10 MHz IF bandwidth over a sweep time of 1 s with no trace averaging. Custom MATLAB code performed LO frequency sweeping, power measurements, and data processing. Four hot/cold sweeps were performed for each DUT measurement, and the noise temperature and linear gain at each frequency were averaged across the four sweeps. Measurements were first performed across 145–176 GHz using WR-6.5 components with a taper to the WR-5.1 mixer input, and separately from 170–210 GHz using entirely WR-5.1 components.

The noise calibration was validated by measuring an impedance standard substrate thru structure. The measured gain and noise temperature from the Y-factor results are shown in Figure 2.30. The measured Y-factor gain at each frequency point is within ±1.0 dB across 149–209 GHz, and the mean of the measured gain across all frequency points is 0.15 dB. The mean noise temperature across all frequency points is -95 K, which may indicate a small bias in the LNA NF results. However, this bias may be partially caused by inaccuracies in the measured loss of the output probe or the receiver noise calibration, each of which is mitigated when measuring the LNAs. The calibration quality is worst

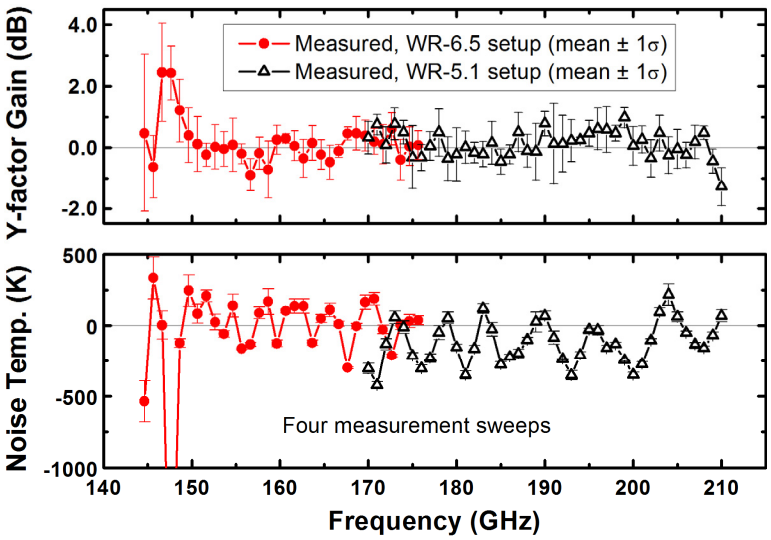

Figure 2.30: Measured gain and noise temperature of an impedance standard substrate thru structure [4] © 2016 IEEE. The displayed measurement points represent the mean of the four measurements at each frequency point plus or minus one standard deviation (σ). The thin horizontal lines represent the nominally expected 0 dB gain and 0 K noise temperature.

below 150 GHz, which is near the bottom of the operating bands for both the WR-5.1 mixer and the WR-10 LO source module.

Figure 2.31 shows the measured versus simulated NF of the *G*-band cascode LNA. Between 145 and 165 GHz, in the midband range of the LNA, the mean NF is 8.2 dB. The NF steadily rises as the LNA gain rolls off, and the NF is 10.0 dB at the intended design frequency of 183 GHz. The mean NF across the 165–200 GHz sensing band is 10.1 dB. The measured NF exhibits a downward frequency shift from simulation similar to that exhibited by the measured S-parameters (Figure 2.22). The faster roll off of the measured versus simulated NF is expected due to the reduced bandwidth observed in the S-parameter measurements. The increased NF in the midband range of the LNA is potentially caused by inaccuracies in the modeling of the SiGe HBTs and polysilicon resistors in the *G*-band,

discrepancies between the EM-simulated versus fabricated passive structures, or a small probe contact resistance.

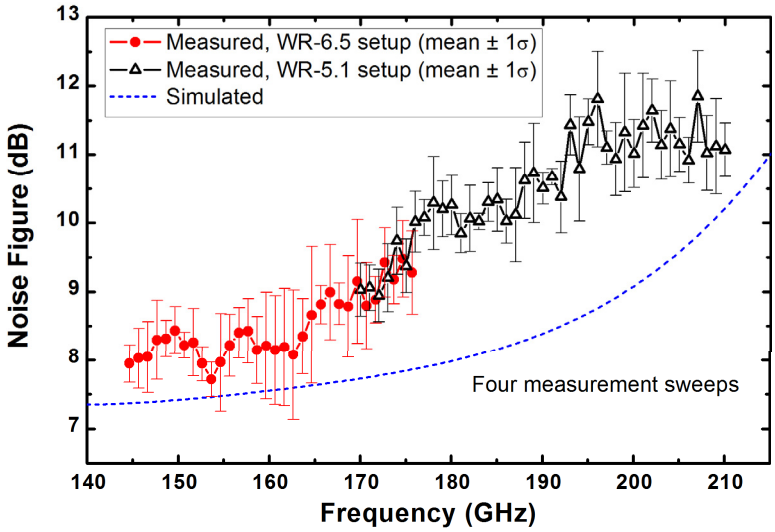

Figure 2.31: Measured and simulated NF of the *G*-band cascode LNA. The displayed measurement points represent the mean of the four measurements at each frequency point plus or minus one standard deviation [4] © 2016 IEEE.

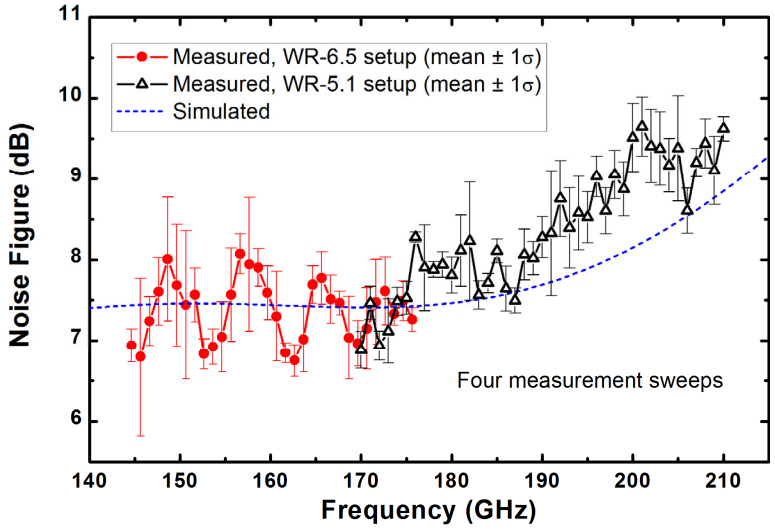

Figure 2.32: Measured and simulated NF of the *G*-band CE LNA. The displayed measurement points represent the mean of the four measurements at each frequency point plus or minus one standard deviation [4] © 2016 IEEE.

The measured versus simulated NF of the CE LNA is shown in Figure 2.32. The ripple below 170 GHz is primarily caused by the impedance mismatch between the reflective DUT input and the imperfectly matched probes. This LNA is more reflective than the cascode LNA input in this range, hence the larger observed ripple. The average NF is 7.4 dB between 145–175 GHz, which agrees well with simulation. The NF increases to 7.6 dB at 183 GHz and remains below 9 dB up to 200 GHz. Across the 165–200 GHz sensing band, the mean NF is 8.0 dB. The NF roll off occurs at a lower frequency than simulated, but matches the downward frequency shift observed from the measured S-parameters. Furthermore, the rate of the NF roll off matches simulation and is more gradual than that of the cascode LNA due to the wider matching bandwidth of the CE SiGe HBTs. The NF of the CE LNA more closely matches simulation than the cascode LNA, which indicates that the contributed noise of the CB SiGe HBTs in the cascode amplifier is higher than simulated while the noise parameter modeling of the CE devices is relatively accurate.

The NF data quality could be improved in future measurements by using a quasi-optical chopping setup to compensate for $1/f$ drift in the receiver. Alternatively, a noise source with a higher excess noise ratio (ENR), when commercially available, could be used to obtain a higher Y-factor and reduce the sensitivity to receiver drift. However, the quality of these measurements could be best enhanced by improving the input matching of the LNAs and using better-matched RF probes.

2.3.5 Gain Compression Measurement

The 1-dB compression point (P_{1dB}) of each amplifier was characterized to verify sufficient linearity for remote sensing applications. Figure 2.33 shows a block diagram of

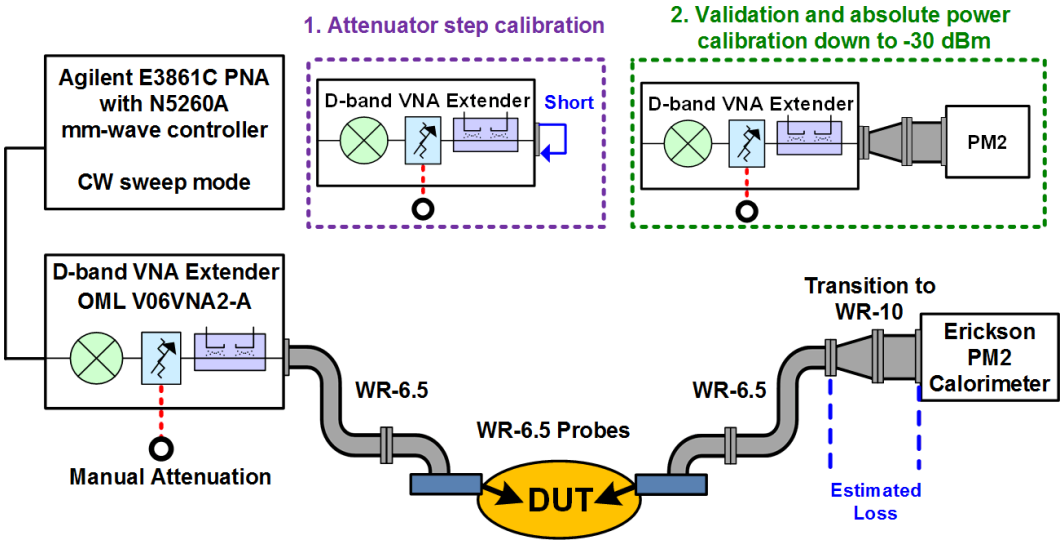

Figure 2.33: Block diagram of the on-wafer *G*-band gain compression measurement setup, showing the main power calibration steps [4] © 2016 IEEE.

the measurement setup along with the power calibration methodology. The OML V06VNA2-T/R-A VNA extender was driven in the single-frequency CW mode, and the source power was varied by adjusting the manual attenuator built in to the VNA extender. The nominal source power of the D-band extender with zero attenuation, as specified by OML, is -10 dBm. The output power was measured by an Erickson PM2 calorimeter through a Virginia Diodes WR-6.5 to WR-10 taper and a 2.5 cm long WR-10 straight section. Only one tapered transition was available, so the insertion loss of the taper could not be directly measured. The combined IL of the taper and the WR-10 section was therefore estimated per the manufacturer's suggested method using

$$\text{Loss (dB)} = 0.5 \times f + 0.35 \tag{2.2}$$

where f is the frequency in THz [69].

The minimum specified input power to the Erickson calorimeter is -30 dBm; however, it is desirable to calibrate down to at least -40 dBm to reliably measure the small-signal gain of these LNAs with simulated input-referred P_{1dB} as low as -28 dBm. This

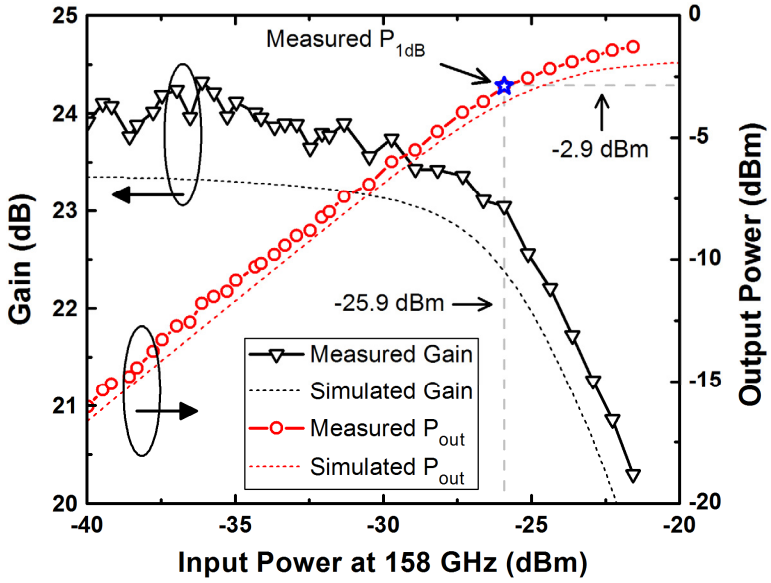

Figure 2.34: Measured and simulated gain and output power of the *G*-band cascode LNA versus 158 GHz input power [4] © 2016 IEEE.

calibration was achieved by first connecting a waveguide short to the VNA extender output and manually adjusting the attenuator while recording the raw response of the VNA reference receiver (R1). Using this method, the attenuator was calibrated across a range of 0–34 dB with excellent repeatability. Next, the PM2 was connected to the VNA extender output to determine the absolute output power of the VNA extender across the measurable power range and validate the attenuator step calibration. The attenuator was stepped through the same dial positions used in the VNA receiver response measurements, and the attenuation steps measurable down to -30 dBm using the PM2 matched the receiver response results to within ±0.40 dB. Due to the excellent agreement, the attenuation steps extending below -30 dBm were validated. A final calibration verification was performed with the waveguide S-bends and probes in place while probed down on an on-wafer thru structure to verify the accuracy of the WR-6.5 and wafer probe ILs.

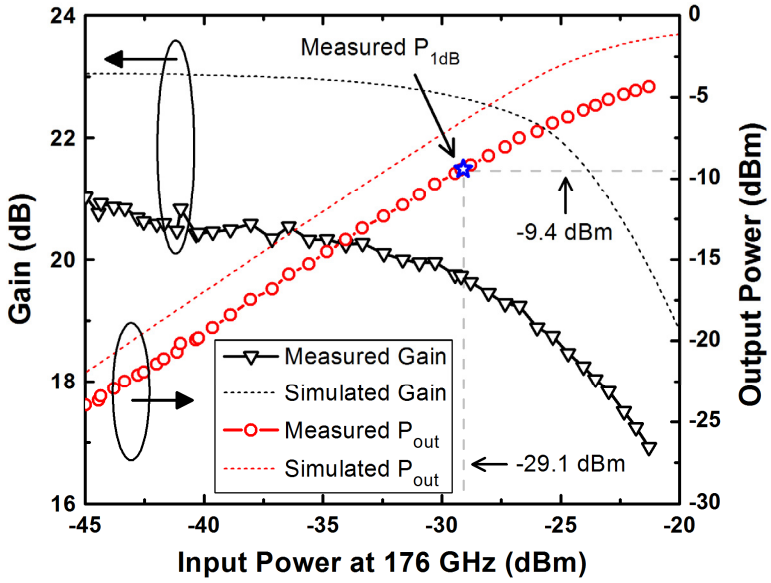

Figure 2.35: Measured and simulated gain and output power of the *G*-band CE LNA versus 176 GHz input power [4] © 2016 IEEE.

The cascode LNA was measured at 158 GHz to obtain the best possible impedance matching (S_{11} = -4.0 dB, S_{22} = -27.8 dB) and minimize reflection-induced errors. The results, shown in Figure 2.34, indicate that the measured input-referred P_{1dB} and output-referred P_{1dB} of the LNA are -25.9 dBm and -2.9 dBm, respectively. These closely match the simulated input-referred P_{1dB} of -26.0 dBm and output-referred P_{1dB} of -3.6 dBm. The measured gain, although higher than simulated due to the downward frequency shift from simulation (see Figure 2.22), closely matches the measured S_{21}, which implies that these results are accurate to within a few tenths of a decibel. Some uncertainty is present due to the imperfect DUT input matching at 158 GHz along with the estimated IL of the taper and the WR-10 straight section.

The measured S-parameters (Figure 2.23) of the CE LNA indicate optimal matching above 180 GHz. However, the output power of the WR-6.5 VNA extender and the insertion loss of the WR-6.5 probes significantly degrade above 176 GHz, so 176 GHz

was the selected frequency for this measurement. The measured and simulated results are shown in Figure 2.35. The measured input-referred P_{1dB} and output-referred P_{1dB} are -29.1 dBm and -9.4 dBm, respectively, which are lower than the simulated values of -25.3 dBm and -3.2 dBm. The measured small-signal gain, 2 dB lower than simulated due to the frequency shift from simulation, is roughly 0.5 dB larger than the measured S_{21}, which indicates increased uncertainty for this amplifier measurement.

One potential cause of the reduced output-referred P_{1dB} from simulation is the imperfect matching of the LNA at 176 GHz (S_{11} = -7.1 dB, S_{22} = -6.8 dB) in conjunction with the unknown matching of both the PM2 power meter and the VNA extender operating beyond its specified bandwidth. Additionally, due to the low reverse isolation of the CE SiGe HBTs at *G*-band, any changes in the output impedance under large-signal conditions will cascade through the CE stages and degrade the interstage matching, potentially significantly altering the amplifier performance. The large-signal input and output impedances of the CE SiGe HBTs at millimeter-wave frequencies may not be well modeled, so this effect can partially explain the observed discrepancy.

2.3.6 Summary

Two SiGe HBT LNAs for *G*-band radiometers have been presented. The cascode LNA achieves a mean NF of 8.2 dB from 145–165 GHz, while the CE LNA attains a mean NF of 8.0 dB across the 165–200 GHz passive sensing band. This performance was achieved by carefully optimizing the transistor core layouts and considering the design tradeoff space for NF with low-gain transistors. Optimized designs with corrected impedance matching and higher-impedance local substrate connections for the SiGe HBT cores would likely yield improved performance. The CE topology appears preferable to the

cascode topology for NF-constrained millimeter-wave applications, and is markedly less sensitive to frequency shifts from simulation than the cascode topology.

The measured performance of these amplifiers is benchmarked versus similar *G*-band amplifiers in Table 2.2. The *G*-band amplifiers presented here achieve the lowest measured NFs to date for SiGe HBT amplifiers at these frequencies, whereas the measured linearity and power dissipation are highly competitive. However, the NF of these LNAs is significantly higher than the 3.4 dB packaged NF achieved by the state-of-the-art InP HEMT LNAs [70] which are being used in the TEMPEST CubeSats [17] and were previously used in the RACE CubeSat [13]. SiGe LNAs cannot yet match the noise performance of the best GaAs and InP LNAs, however, the NF of the SiGe LNAs demonstrated here is close to the SSB NF of *G*-band DSB mixers [71] which are still being used in radiometers on CubeSats such as MiRaTA [15]. SiGe amplifiers warrant consideration for use in millimeter-wave radiometers where integration, 1/*f* noise, and total-dose radiation tolerance are important considerations.

Table 2.2: Comparison to similar published *G*-band LNAs [4] © 2016 IEEE.

Reference	Freq. (GHz)	Gain (dB)	NF (dB)	P_{DC} (mW)	Technology	Peak f_T / f_{max} (GHz)
[72]	140	23	5.8	12	130 nm SiGe HBT	300 / 500
[73]	140	30	6.2	45	90 nm SiGe HBT	300 / 350
[74]	156	26	8.5†	67	250 nm SiGe HBT	230 / 350
This (cascode)	158	24.1	8.2	28	130 nm SiGe HBT	300 / 500
[75]	160	24	8.9†	59	130 nm SiGe HBT	300 / 350
[76]	165	35	8.25†	92	130 nm SiGe HBT	270 / 330
This (CE)	183	17.2	7.6	16.1	130 nm SiGe HBT	300 / 500
[77]	200	16.9	9.4*	18	130 nm SiGe HBT	300 / 500
[78]	210	15	13*	151	250 nm SiGe HBT	280 / 435
[79]	233	22.5	12.5*	68	130 nm SiGe HBT	300 / 500
[80]	150	19	4	29	50 nm GaAs mHEMT	375 / 500
[64]	165	20	4.4	44	50 nm GaAs mHEMT	370 / 375
[81]	180	22	4.9#	-	35 nm InP HEMT	400 / 1100
[70]	183	17	3.4#	-	35 nm InP HEMT	400 / 1100
[64]	183	17	6.5	32	50 nm GaAs mHEMT	370 / 375
[82]	183	24.5	3.5	24	50 nm GaAs mHEMT	370 / 670
[83]	210	16	4.8	24	50 nm GaAs mHEMT	400 / 420
[84]	210	18	11†	44.5	32 nm SOI CMOS	250 / 320
[42]	232	35.2#	5.0#	50	35 nm GaAs mHEMT	515 / >1000

*Simulated †System measurement #Packaged module

CHAPTER 3

WIDEBAND IF AMPLIFIER AND SQUARE-LAW DETECTOR

3.1 Introduction

Millimeter-wave radiometers for atmospheric sounding are usually implemented using a heterodyne receiver architecture. In these systems, it is desirable to downconvert wide millimeter-wave frequency bands, often spanning over 10 GHz, to lower microwave frequencies where physically realizable IF filters can separate the wideband downconverted noise into multiple separate narrow channels which are separately detected. The noise detected in each channel is related to the radiation emitted by the atmosphere within a specific altitudinal distribution, and this relationship is defined by a distinct weighting function for each channel. It is desirable to measure the millimeter-wave radiation near an atmospheric resonance frequency within a large number (tens to hundreds) of narrow frequency bands, which each have distinct yet overlapping weighting functions. By measuring the emitted radiation within a large number of channels, the separate weighting functions for each channel can be used to obtain high-resolution vertical profiles of the atmosphere. An instrument implemented using this technique, known as hyperspectral sounding, can potentially obtain atmospheric profiles of similar quality to those obtained using combined data from modern microwave and infrared sounders at a much lower cost [85,86].

Efforts are underway to demonstrate a hyperspectral microwave sounding unit with low size, weight, and power consumption for future use on CubeSats. MIT Lincoln Laboratory is developing compact IF receiver modules that have an input IF bandwidth of

18–29 GHz for this purpose [86,87,88]. Low temperature co-fired ceramic (LTCC) filters are used to perform this channelization within a highly compact volume, making such IF processors sufficiently small for use on CubeSats [15]. This IF amplifier uses wideband amplifier MMICs to provide not only gain, but also isolation between the reflective filters. The power consumption of each of the GaAs pHEMT amplifiers used for this purpose is around 200 mW, so only a limited number of amplifiers can be used due to system power constraints. Low-power amplifiers which cover the entire IF bandwidth would simplify the implementation of many-channel modules and/or reduce the power consumption of each IF module. Additionally, the square-law power detectors which detect the noise power in each channel are manually constructed and tuned using discrete diodes [89,87]. An improved detector for these modules would be an integrated circuit that covers the entire IF bandwidth, so one detector MMIC could be fabricated and used in every channel.

This chapter presents the design of an 18–30 GHz SiGe HBT IF amplifier and a square-law detector for these IF receiver modules. SiGe technologies are well-suited for and producing many wideband low-power amplifier MMICs with low chip-to-chip performance variability due to the properties of silicon fabrication. SiGe HBTs are also capable of implementing square-law detectors with excellent $1/f$ noise and high responsivity. These detectors would improve the integration and reduce the IF and video gain required in these systems, potentially enabling further power reductions in the IF module. The performance of these circuits demonstrates the ability of custom SiGe RFICs to enable improved atmospheric soundings using CubeSat-compatible instruments. The IF amplifier and detector presented in this chapter are both developed in the GlobalFoundries

0.13 μm BiCMOS8HP technology, a mature process which offers SiGe HBTs with peak f_T/f_{max} of 210/290 GHz.

3.2 Low-Power IF Amplifier

3.2.1 Design

The SiGe HBT IF amplifier was designed to achieve at least 15 dB of gain across the target bandwidth of 18–30 GHz with an NF less than 5 dB and the minimum possible DC power consumption. To ensure that the wideband amplifier maintains linear behavior while amplifying relatively high noise powers, the amplifier was designed to achieve an output-referred P_{1dB} greater than 0 dBm. Meeting each of these specifications typically involves trading off one or more of the other specifications, so to achieve all of these specifications simultaneously requires a combination of multiple performance-enhancing techniques.

A schematic of the amplifier is shown in Figure 3.1. Two amplifying stages were utilized to achieve the desired gain. The first stage uses a cascode topology to obtain the majority of the required gain and to set the NF of the amplifier. The emitter length of the common-base (CB) SiGe HBT is shorter than that of the common-emitter (CE) SiGe HBT, so for a fixed collector current, the CB SiGe HBT is driven at a higher current density than the CE device, which increases the voltage gain of the cascode. Series resistors are connected to the base of the CB device to prevent oscillations [53]. The second stage is implemented using a CE SiGe HBT to add some additional gain and enable a wideband output match, as CE SiGe HBTs have lower output capacitance than cascoded SiGe HBTs.

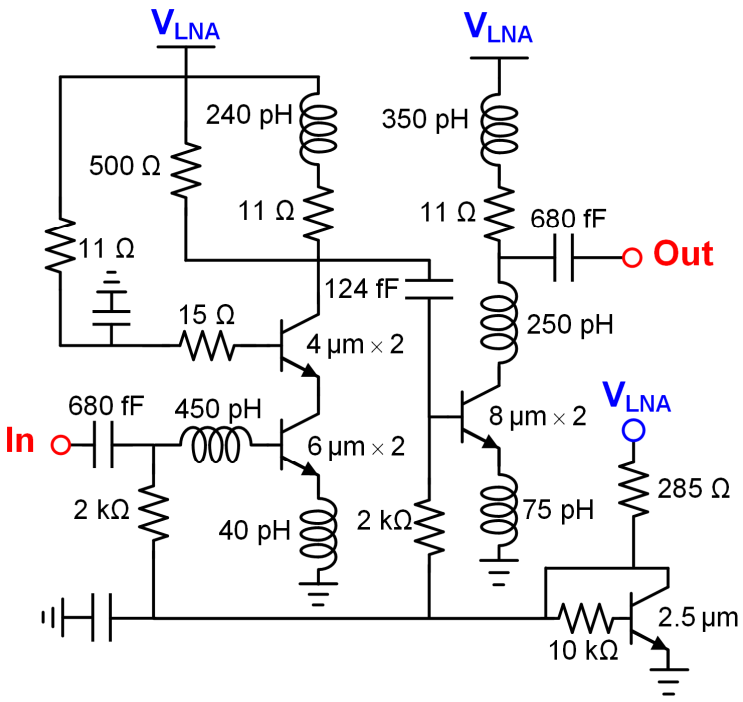

Figure 3.1: Schematic of the wideband and low power SiGe HBT IF amplifier.

Two 8 μm SiGe HBTs are used in parallel to enable a relatively large current swing for the output stage.

Both stages share a common supply voltage to enable simple biasing with low power dissipation. The maximum supply voltage with this configuration is limited by the breakdown voltage of the second-stage CE HBTs, which is slightly larger than the nominal BV_{CEO} of 1.8 V. The minimum supply voltage is limited by the cascode stage. Simulations indicate that the lowest supply voltage which keeps both of the cascode SiGe HBTs in the forward-active mode of operation is 1.8 V. The performance of SiGe HBTs, however, is not significantly degraded in the weakly saturated mode of operation [90,91], and simulations indicate that the performance of the cascode stage is not significantly reduced when a supply voltage drops to as low as 1.2 V. A nominal supply voltage of 1.4 V is selected as a compromise between performance and power dissipation. A shared current

mirror, implemented using a single SiGe HBT with a short emitter length of 2.5 μm, is used to enable simple control of the amplifier biasing. The mirror was designed for the same nominal supply voltage as the amplifying SiGe HBTs, so only a single DC supply is required to power this amplifier.

A small amount of emitter inductance was used in each stage to reduce the tradeoff between noise and gain matching without significantly degrading the noise measure of each stage. To achieve the desired bandwidth, a resistor was connected in series with each of the shunt peaking inductors used in the interstage and output matching networks. These resistors slightly decrease both the P_{1dB} and the collector voltage presented to each amplifying stage, however, 11 Ω was found to provide a sufficient balance between the bandwidth and performance. All passive components were designed and modeled using Sonnet, and all bias lines used small series resistors and multiple sizes of MIM capacitors to ensure low-frequency stability. A photograph of the fabricated chip is shown in Figure 3.2.

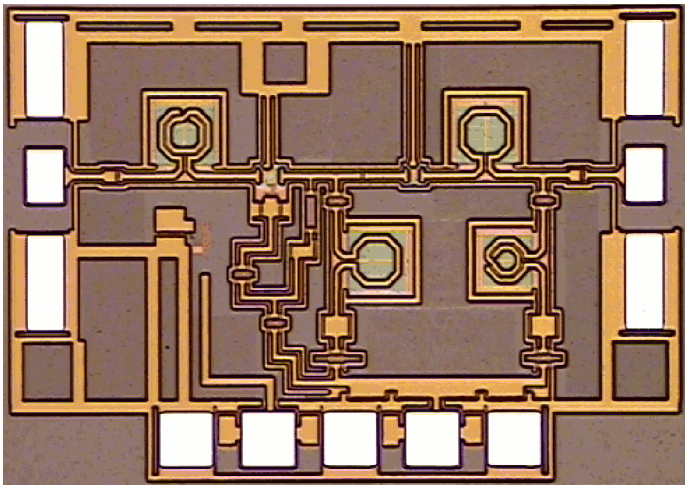

Figure 3.2: Photograph of the fabricated SiGe HBT IF amplifier. The size of the chip, including bondpads, is 1.22 mm × 0.85 mm.

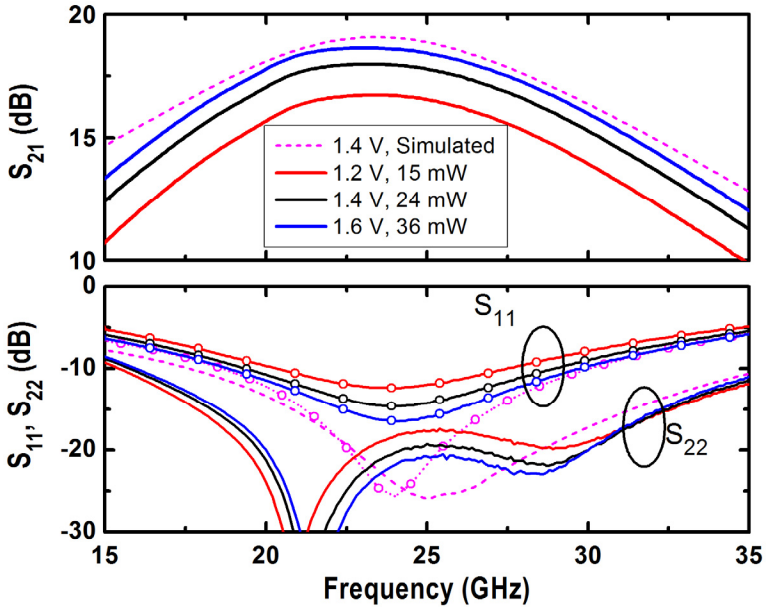

Figure 3.3: Measured and simulated S-parameters of the SiGe HBT IF amplifier.

3.2.2 Measurement

The S-parameters of the IF amplifier were measured on-chip across multiple bias points using an Agilent E8363B VNA and GGB wafer probes. The measured and simulated results are shown in Figure 3.3. Although the measured and simulated peak gain frequencies are in close agreement, the peak gain is 1 dB lower than simulated. At the nominal bias voltage of 1.4 V, the peak gain is 18 dB at 23.9 GHz and the 3-dB bandwidth is 17.4–30.4 GHz. The input and output return losses are better than 7.9 dB and 13.0 dB, respectively, across the bandwidth.

The NF of the amplifier was measured across frequency using the cold-source measurement method described in Section 2.2.2. The measured and simulated NFs are shown in the upper half of Figure 3.4. The measured NF agrees well with simulation and does not significantly vary with bias. The NF is better than 3.5 dB across the target 18–30 GHz bandwidth at all bias points, and the mean NF across the band is 3.1 dB when

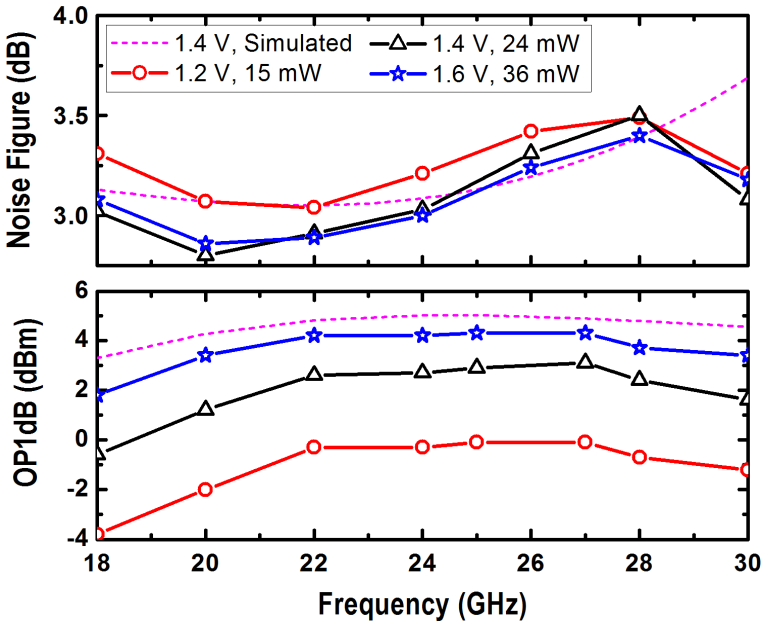

Figure 3.4: Measured and simulated NF and output-referred P1dB of the SiGe HBT IF amplifier.

biased at 1.4 V. The measured output-referred P_{1dB}, shown in the lower half of Figure 3.4, is 2–3 dB lower than simulated. The P_{1dB} strongly varies with bias as expected due to the reliance of the output voltage and current swings on the DC operating points of each stage. The mean output-referred P_{1dB} values across the band when biased at 1.2 V, 1.4 V, and 1.6 V are -1.0 dBm, 2.0 dBm, and 3.7 dBm, respectively.

3.2.3 Summary

This section presented the design of a wideband and low-power IF amplifier for power-constrained hyperspectral millimeter-wave radiometers. The amplifier achieved a peak gain of 18 dB and a mean NF of 3.1 dB with a 54% bandwidth while only consuming 24 mW of power at the nominal bias point. The gain, NF, and P_{1dB} were balanced through careful design and biasing of the two amplifying stages, while the bandwidth was achieved

Table 3.1: Performance comparison to similar wideband microwave LNAs.

Ref	Technology	Bandwidth (GHz)	P_{DC} (mW)	Gain (dB)	Mean NF (dB)	P_{1dB} (dBm)
This	130 nm SiGe HBT	17.4–30.4 (54%)	24	18	3.1	2
[92]	180 nm SiGe HBT	16–24 (40%)	22.5	19	2.2	2
[93]	180 nm SiGe HBT	23–32 (33%)	13	12	5.4	-
[94]	130 nm SiGe HBT	3–26 (159%)	42.5	9	< 6.5	2.4
[95]	90 nm CMOS	1.6–28 (178%)	21.6	9.6	3.66	0
[96]	GaAs pHEMT	18–32 (56%)	195	15	3	12

through the use of resistors in series with the shunt peaking inductors in conjunction with inductive emitter degeneration.

The results from this amplifier are compared to the results of similar amplifiers in Table 3.1. This amplifier achieves similar performance with a wider fractional bandwidth compared to state-of-the-art SiGe and CMOS, and has superior gain and NF to ultra-wideband amplifiers in this frequency range. The power consumption is a factor of eight lower than that of the Analog Devices HMC519 pHEMT amplifiers [96] currently used in hyperspectral radiometer receivers [89,87]. These custom SiGe amplifiers can potentially enable major power savings in these IF receiver modules for power-constrained CubeSats or enable a greater number of IF channels for a given system power dissipation.

3.3 Square-Law Detector

The integrated SiGe HBT square-law detector was designed for a 3-dB bandwidth of 18–30 GHz, high responsivity, low noise-equivalent power (NEP), and the lowest attainable 1/*f* noise. Typical detectors used in these systems are constructed using zero-bias Schottky diodes [87,88], which exhibit very little 1/*f* noise because they are not biased. Active SiGe HBT detectors require biasing to obtain high responsivity, so their 1/*f* noise is

unavoidably higher than that of zero-bias diodes with no power applied. However, SiGe HBTs have the lowest 1/*f* noise of all high-frequency transistors [47], and SiGe HBT active detectors can potentially be designed to achieve levels of 1/*f* noise which are low enough that Dicke modulation is not required. This section presents the design, optimization, and characterization of such a detector for hyperspectral radiometer receivers. This work has been submitted for publication [5].

3.3.1 Design

Figure 3.5 shows a schematic of the power detector, which is implemented using a common-emitter SiGe HBT, Q_1, biased with a V_{CC} of 1.5 V through a large collector resistor, R_C. The value of R_C was selected to be 1 kΩ to achieve a high responsivity while ensuring that R_C could be implemented in a small area using a wide thin-film TaN resistor to limit the 1/*f* noise contribution from this resistor. Large shunt capacitors were connected to the collector to reject RF noise and harmonics at the output. A separate and identical DC reference path was included to enable tracking of the output voltage due to changing operating conditions. Dummy SiGe HBTs surround Q_1 and Q_2 to minimize the DC voltage offset between the output and reference paths. Bias voltages are applied to Q_1 and Q_2 through a current mirror to enable simple bias control. The current mirror transistor, Q_3, was implemented using two parallel SiGe HBTs to reduce its equivalent base resistance and its contribution to the output noise.

The emitter length of the SiGe HBT was selected to achieve the desired 18–30 GHz bandwidth. To attain a 50% bandwidth, the quality factor (Q) of the SiGe HBT input impedance (Z_{in}) should be equal to or less than 2. Figure 3.6 shows the simulated Q of Z_{in} and the responsivity at both 18 GHz and 30 GHz versus emitter length (L_{emit}) at a fixed

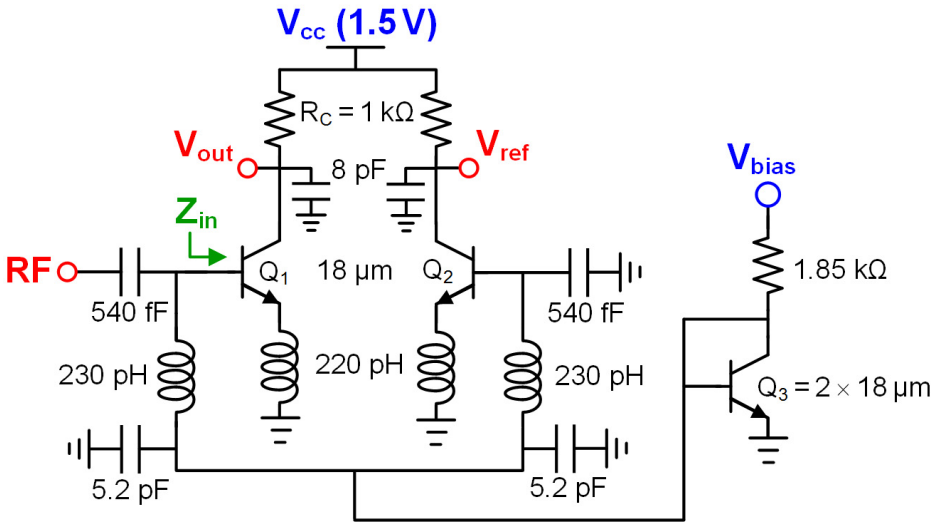

Figure 3.5: Schematic of the SiGe HBT square-law power detector [5].

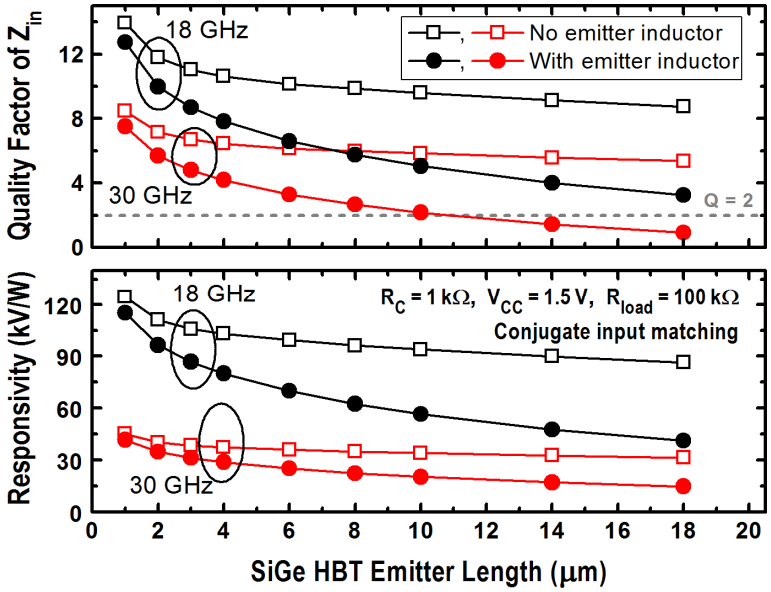

Figure 3.6: Simulated responsivity and quality factor of the input impedance (Z_{in}) of the SiGe HBT versus emitter length at a fixed collector current density $J_C = 75\ \mu A/\mu m^2$, with and without the 220 pH emitter inductor [5].

current density. The Q at the desired mid-band frequency, 24 GHz, lies between the 18 GHz and 30 GHz Q values. The Q decreases with increasing L_{emit}, but does not approach 2 at either edge of the band when using a maximum-size 18 μm SiGe HBT. Inductive emitter degeneration was used to improve Q (following [97]), and 220 pH was found to

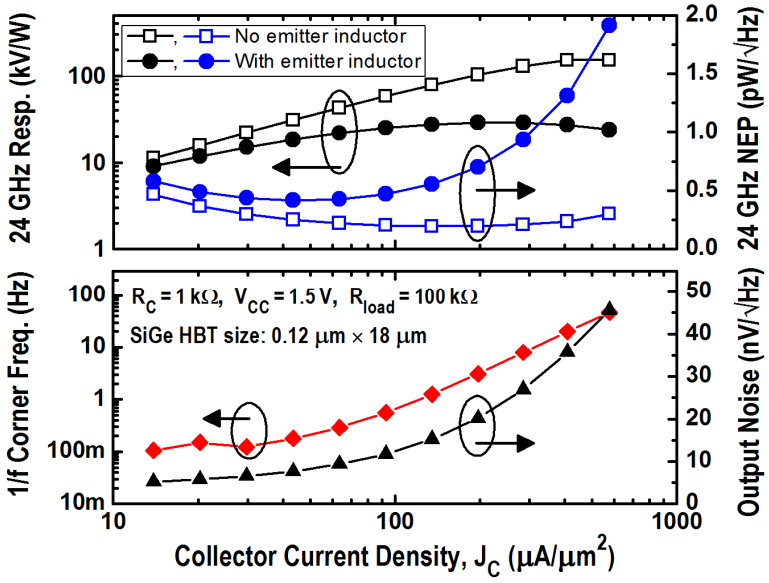

Figure 3.7: Simulated 1/*f* corner frequency, output noise voltage, and 24 GHz responsivity and NEP of the SiGe HBT versus current density. The impact of the 220 pH emitter inductance on the responsivity and NEP across bias is shown [5].

be sufficient. This inductance improves Q to 3.2 at 18 GHz, 1.9 at 24 GHz, and 0.9 at 30 GHz when L_{emit} is 18 μm. Although Q is greater than 2 in the lower portion of the band, Q is significantly below 2 at 30 GHz so the input match can be tuned for the lower portion of the band while still obtaining sufficient matching at 30 GHz. The emitter degeneration significantly reduces the responsivity, but this tradeoff is necessary to achieve the desired bandwidth.

The biasing was selected to achieve a low NEP while ensuring a low 1/*f* corner frequency. Figure 3.7 shows the simulated 1/*f* corner frequency, the mean output noise voltage in the white noise range (V_{no}), and the 24 GHz responsivity and NEP of the 18 μm SiGe HBT versus collector current density. With the emitter inductor in place, the mid-band NEP is minimized at a collector current density of 50 μA/μm^2. The TaN current

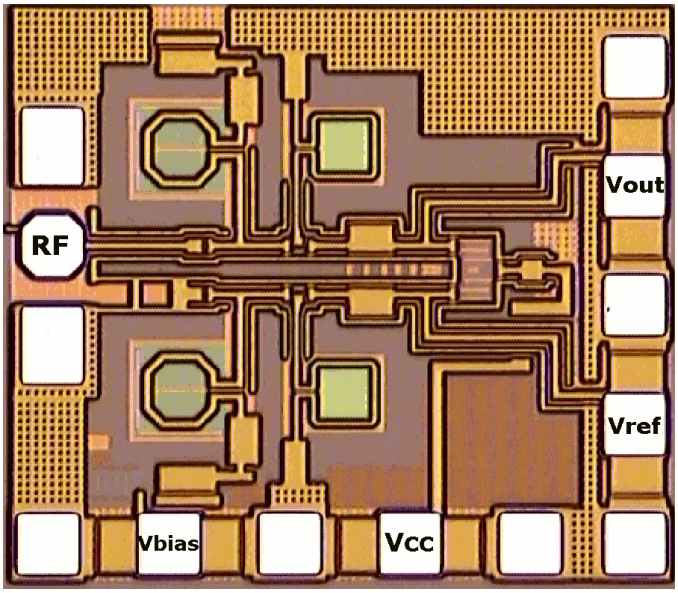

Figure 3.8: Microphotograph of the fabricated power detector, measuring 0.82 mm × 0.72 mm including bondpads [5].

mirror resistor was selected to be 1.85 kΩ to enable the current density to be varied between 35–160 μA/μm^2 with a V_{bias} ranging between 1.0–2.0 V.

The emitter-degenerated SiGe HBT was matched to 50 Ω using a 230 pH shunt inductor. Biasing is applied to the base of the SiGe HBT through this inductor to avoid using additional biasing resistors, which would add 1/f noise. Large shunt capacitors were used to establish an RF ground on each shunt inductor and to prevent RF noise from feeding through from Q_3 into Q_1 or Q_2. All passives were EM-simulated using Sonnet to ensure close agreement between measurement and simulation.

3.3.2 Measurement

A die photograph of the detector is shown in Figure 3.8. The S-parameters were measured on-chip using an Agilent E8363B VNA and GGB wafer probes. Figure 3.9 shows the measured and simulated S_{11} and S_{22} of the detector biased at V_{bias} = 1.4 V. The measured results closely agree with the simulated performance. The input return loss is greater than

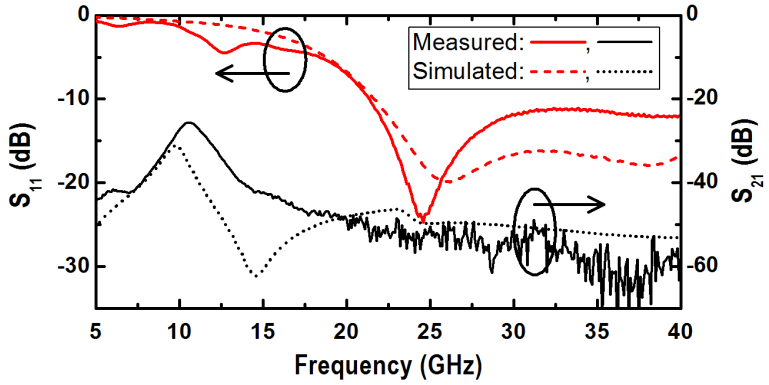

Figure 3.9: Measured and simulated S_{11} and S_{21} of the detector biased at V_{bias} = 1.4 V (I_C = 188 μA) [5].

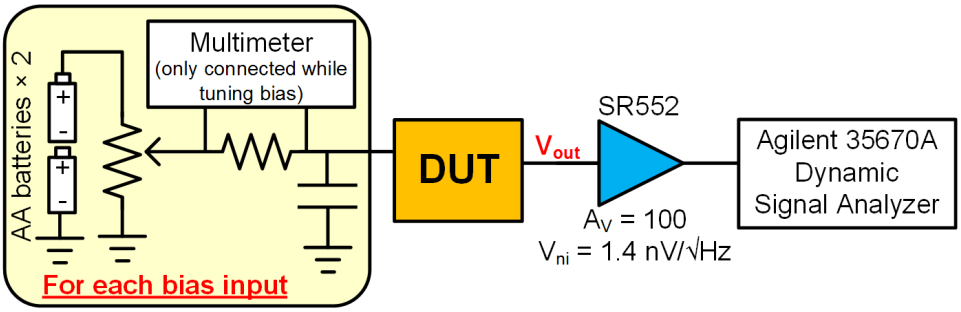

Figure 3.10: Block diagram of the 1/*f* noise measurement setup [5].

10 dB across 21.4 to >40 GHz, and the isolation between the input and output is greater than 45 dB.

Low-frequency noise measurements were performed in a screen room to obtain a clean spectrum. A block diagram of the 1/*f* noise measurement setup is shown in Figure 3.10. Biasing was applied using AA batteries, and voltage tuning was performed using a metal foil potentiometer. The output voltage V_{out} is connected to a SR552 low-noise voltage amplifier (following [98]), and a dynamic signal analyzer measured the low-frequency spectrum from 1 Hz to 100 kHz. The input noise voltage of the SR552 amplifier was subtracted out of the measured results. The SR552 amplifier limits the lower measurement frequency to 1 Hz, and the 1/*f* corner frequencies could not be determined by fitting a 1/*f*

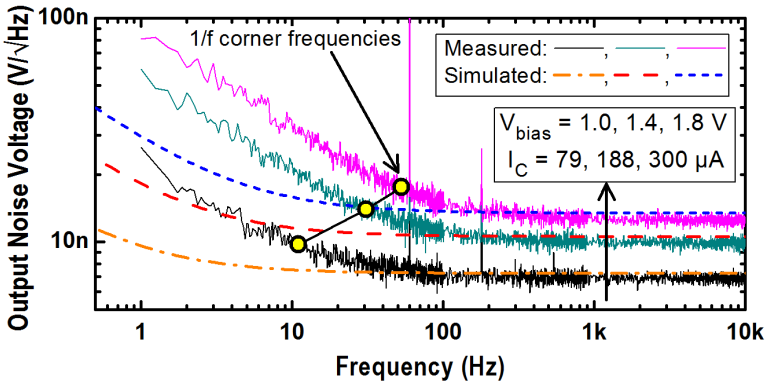

Figure 3.11: Measured and simulated low-frequency output noise spectrum of the detector across multiple bias points, showing the measured 1/*f* corner frequencies [5].

slope to the measured noise due to this lower bound. Therefore, all 1/*f* corner frequencies reported here were determined from the frequency at which the RMS 1/*f* noise equals the RMS white noise, that is, when the total noise is equal to $\sqrt{2} \times V_{no}$.

Figure 3.11 shows the measured low-frequency noise results. As V_{bias} is increased from 1.0–2.0 V, the mean value of V_{no} increases from 6.9–13.7 nV/√Hz, which is slightly lower than simulated. The measured 1/*f* corner frequencies, which increase from 11–63 Hz as V_{bias} increases from 1.0–2.0 V, are one order of magnitude higher than simulated. The design kit model guide shows close agreement between the modeled and measured 1/*f* noise of the SiGe HBTs and resistors, so it is possible that this excess 1/*f* noise is introduced by the metal film resistor used for current readout or by the metal foil potentiometer.

Figure 3.12 shows a block diagram of the responsivity measurement setup. The values of V_{out} and V_{ref} are measured using separate multimeters which are nulled out before each measurement to eliminate time-varying zero drifts. Despite the identical and symmetric layouts of the detector output and reference paths, a small millivolt-level DC offset was observed between V_{out} and V_{ref}. The responsivity data presented here is corrected for this offset.

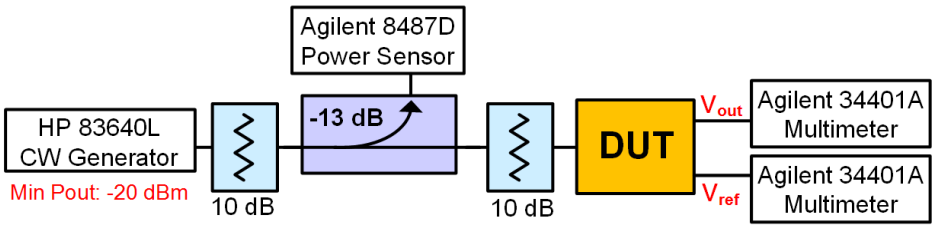

Figure 3.12: Block diagram of the responsivity measurement setup [5].

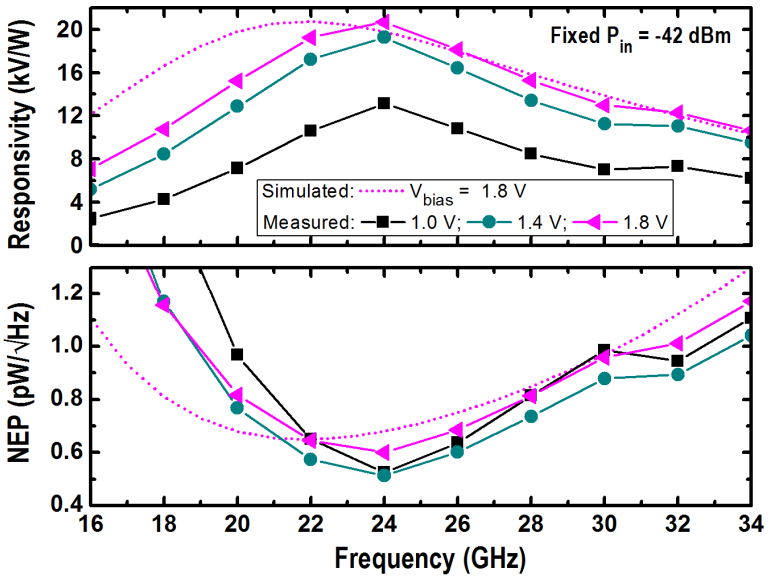

Figure 3.13: Measured and simulated responsivity and NEP of the detector across RF frequency for multiple values of V_{bias}, along with the simulated performance at V_{bias} = 1.8 V [5].

Figure 3.13 shows the measured and simulated responsivity and NEP versus RF frequency for multiple bias points. The peak responsivity shifted slightly upward in frequency, from 22 GHz in simulation to 24 GHz in measurement. The peak mid-band responsivity is greater than 13 kV/W for all values of V_{bias}. The bandwidth increases with increasing V_{bias}, ranging from 20–33 GHz at 1.0 V to 17–34 GHz at 2.0 V. The NEP is calculated by dividing V_{no} by the responsivity. At 24 GHz, the NEP is lower than 0.67 pW/√Hz for all V_{bias}. Across the bandwidth, the NEP is less than or equal to 1.3 pW/√Hz for all values of V_{bias}.

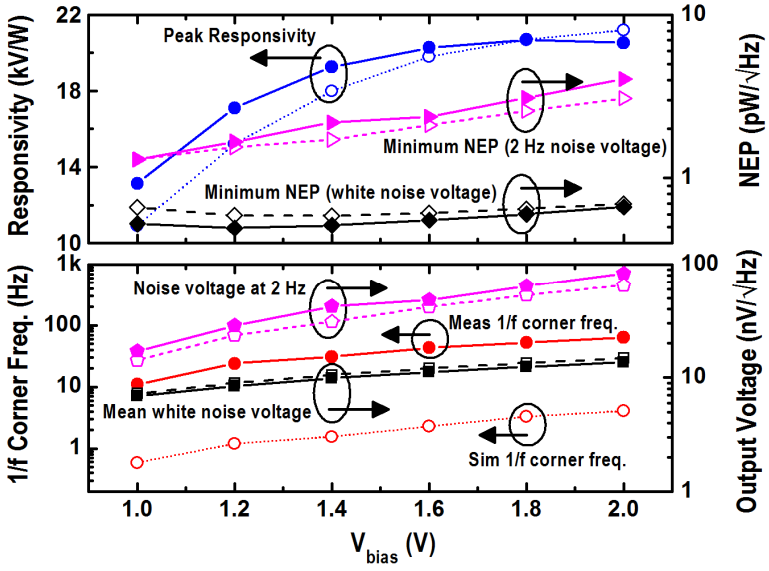

Figure 3.14: Measured (solid lines) and simulated (dashed lines) performance of the detector versus V_{bias} [5].

Figure 3.14 shows the measured and simulated performance versus V_{bias}. When V_{no} is considered, optimal NEP is obtained at a V_{bias} of 1.2 V. To illustrate the impact of the 1/*f* noise, the noise voltage at 2 Hz and the minimum NEP at 2 Hz are plotted as well. When considering the noise at 2 Hz, a reduced V_{bias} of 1.0 V yields the lowest NEP. However, the 1/*f* noise at all bias points is so low that the 2 Hz NEP is lower than 4 pW/√Hz for all values of V_{bias}. The results of this detector are compared to similar detectors in Table 3.2. The values listed for this detector correspond to the optimal NEP V_{bias} of 1.2 V. This detector has highly competitive performance across a wide fractional bandwidth, and to the best of our knowledge, achieves the best (lowest) 1/*f* noise performance to date of all transistor-based square-law detectors for radiometers.

Table 3.2: Comparison with similar transistor-based low-noise detectors [5].

Ref.	Technology	f_0 (GHz)	Bandwidth (GHz)	Resp. (kV/W)	Noise Voltage (nV/√Hz)	NEP (pW/√Hz)	1/*f* Corner Freq.
This	130 nm SiGe HBT	24	19.0 – 33.6 (56%)	17.1	8.45	0.49	24 Hz
[98]	130 nm SiGe HBT	94	≈ 84 – 104 (21%)	12	30	2.5	10 kHz
[99]	250 nm SiGe HBT	63	Broadband	28	125	4.4	200 Hz
[99]	250 nm CB SiGe HBT	63	Broadband	14	36	2.6	1 kHz
[100]	90 nm SiGe HBT	160	$135 – 170^{+}$ (>23%)	11	7	0.7	120 Hz
[97]	130 nm SiGe HBT	55	$<50 – 65^{+}$ (>26%)	0.7	1.4	1.75	200 MHz
[101]	65 nm CMOS	80	70 – 95 (30%)	0.2	<30	<150	>400 kHz
[102]	45 nm SOI CMOS	170	150 – 210 (33%)	3	30	8	10 MHz
[103]	250 nm InP DHBT E-B junction	180	-	3.3	6.3	1.9	1 MHz
[103]	250 nm InP DHBT	180	-	13.4	135	10	1 MHz

3.3.3 Summary

In this section, the design, optimization, and characterization of an active SiGe HBT microwave power detector for hyperspectral radiometers has been presented. A 1/*f* corner frequency as low as 11 Hz is attained by biasing the SiGe HBT at a low current density and carefully designing and deploying resistors. The detector achieves a bandwidth of 56% through the use of large transistors and inductive emitter degeneration. When biased at the optimal NEP bias point, the detector attains a peak responsivity of 17.1 kV/W with an NEP of less than 1.3 pW/√Hz across the entire bandwidth. For comparison, the detectors used in the hyperspectral radiometer prototype, which are constructed using zero-bias silicon Schottky diodes [104], achieve a responsivity of only 4 kV/W over a 5% bandwidth [105]. Each of those detectors consumes a large area of roughly 20 mm^2 on each PCB [87], whereas this SiGe detector consumes a chip area of only 0.59 mm^2. These results highlight the potential of SiGe HBT detectors to reduce the volume, improve the performance, and streamline the design and assembly of hyperspectral IF receiver modules.

CHAPTER 4

POWER EFFICIENT MILLIMETER-WAVE SIGE HBT FREQUENCY DOUBLER

4.1 Introduction

Downconversion mixers in millimeter-wave radiometer receivers must be driven by spectrally clean millimeter-wave local oscillator (LO) signals. These LO signals are usually generated using high-quality microwave signal sources that are multiplied up to the required frequency through the use of frequency multipliers. Typical frequency multipliers used in these millimeter-wave radiometers require high input drive power levels and have significant conversion loss. For example, the *G*-band frequency doubler offered by Virginia Diodes, Inc., a leading supplier of millimeter-wave and submillimeter-wave components, has a typical conversion loss of 10 dB and requires an input power greater than 13 dBm [106]. These high drive levels and conversion losses often necessitate the use of power-hungry amplifiers before and after each multiplier, which results in a high system power dissipation. This can be problematic for large-array applications and power constrained platforms such as CubeSats.

To illustrate the power burden imposed upon these systems by inefficient multipliers, the radiometer for the MicroMAS CubeSat consumes 800 mW of power, 650 mW of which is consumed by the generation a 0 dBm LO signal at 90 GHz to drive the 118 GHz downconversion mixer [107]. This power consumption increases when more mixers are utilized or higher frequency (more difficult to generate) LO signals are required. The developmental MiRaTA CubeSat has one *V*-band mixer and one *G*-band mixer, and

the generation of the millimeter-wave LO signals consumes 2 W—a significant percentage of the power consumed by the satellite [15]. If the conversion loss and input drive level of the multipliers in these systems could be reduced, the power consumption of these radiometers could be significantly reduced.

Active frequency multipliers can attain more efficient performance than the passive multipliers which are traditionally used in these radiometers. Frequency doublers, in particular, can produce multi-milliwatt output powers which are spectrally clean through the use of balanced topologies [108]. This chapter presents the design of an active SiGe HBT frequency doubler for driving *G*-band mixers. This doubler is specifically optimized for conversion gain with a low input drive level and DC power dissipation to achieve more efficient multiplication and demonstrate the potentially significant power savings enabled by the envisioned single-chip SiGe radiometer. This work has been published in [6].

4.2 Circuit Design

The frequency doubler was implemented in the IHP SG13G2 technology. Figure 4.1 shows the full schematic of the frequency doubler, and Figure 4.2 shows a microphotograph of the fabricated circuit. The doubler was designed using two CE SiGe HBTs in a balanced push-push configuration to obtain a strong second harmonic output with odd harmonic suppression. The collector voltage V_{CC} was selected to be 1.5 V to maximize the voltage swing and output power. Although 1.5 V is close to the SG13G2 HBT open-emitter breakdown voltage (BV_{CEO}) of 1.7 V, each SiGe HBT base was voltage-biased through a 33 Ω resistor, so the relevant breakdown voltage of each SiGe HBT as operated, BV_{CER}, is greater than 2.0 V.

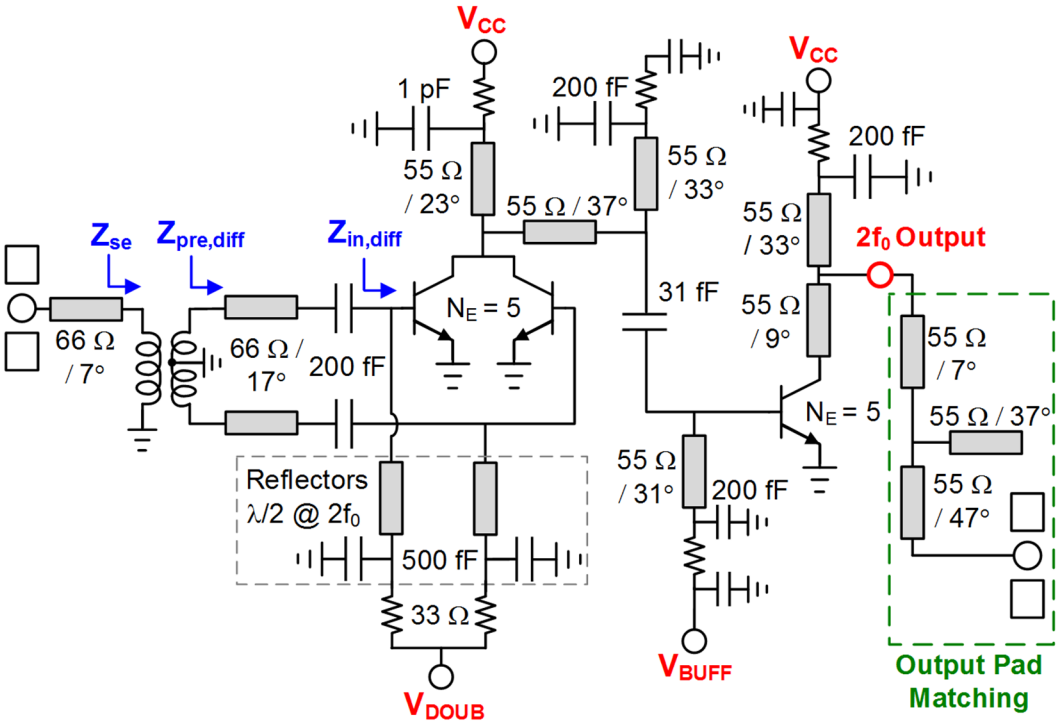

Figure 4.1: Schematic of the SiGe HBT frequency doubler [6] © 2016 IEEE.

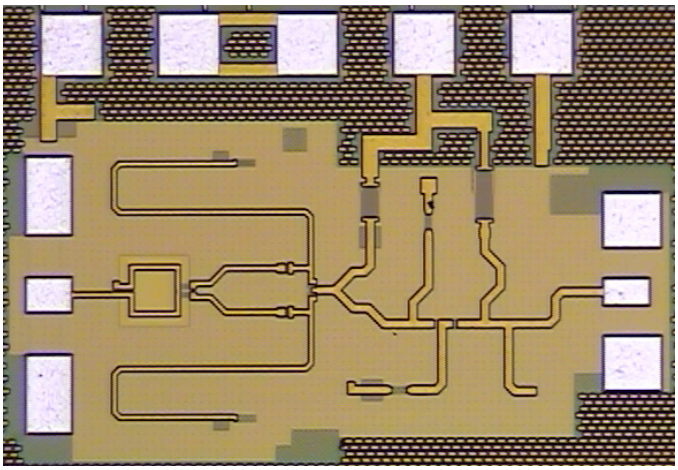

Figure 4.2: Die photograph of the fabricated SiGe HBT frequency doubler, measuring 0.57 μm × 0.85 μm, including bondpads [6] © 2016 IEEE.

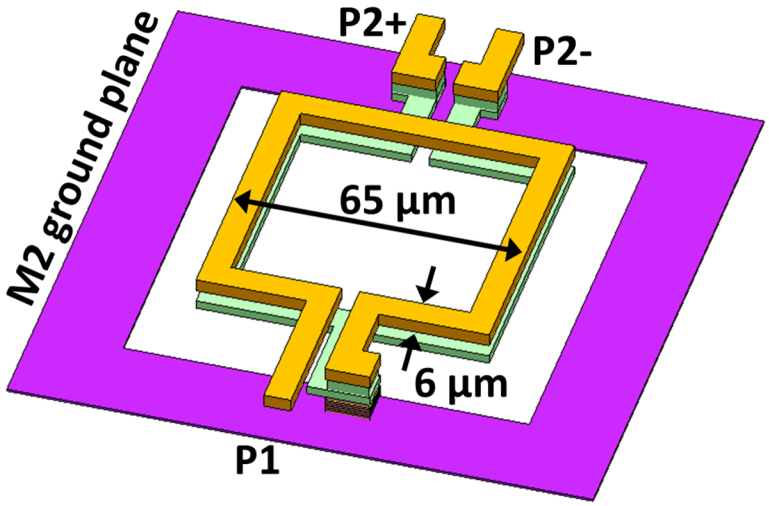

Figure 4.3: Three-dimensional model of the on-chip transformer balun [6] © 2016 IEEE.

In order to minimize the power generation requirements of components preceding the frequency doubler, small SiGe HBTs (A_E = 5 × 0.12 μm × 0.09 μm) were utilized to achieve second harmonic output power saturation with a low input drive power. The SiGe HBT base bias voltage V_{DOUB} was chosen to be 0.675 V (Class B operation) to balance the second harmonic output power and conversion gain. The push-push core was laid out using wide staggered rows of vias which were RC-extracted up to the top metal layer using Assura QRC. Microstrip tee junctions and second harmonic reflector stubs were placed at the input of each transistor to increase the output power and conversion gain following [109]. All microstrip lines were implemented using the thick top aluminum layer over a thin aluminum M2 ground plane.

The on-chip balun was implemented using a transformer topology to minimize the required chip area. As shown in Figure 4.3, the balun, designed using Sonnet, was implemented using a single-turn center-tapped stacked square spiral using the thick top

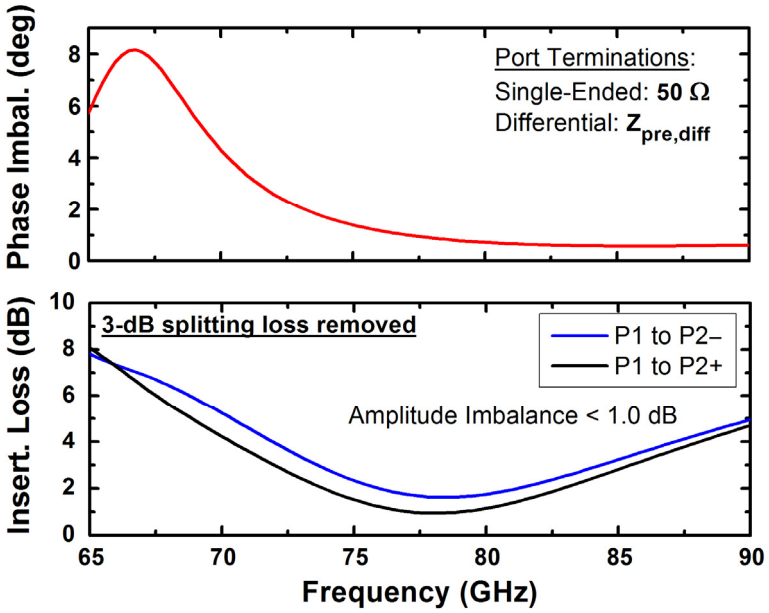

Figure 4.4: Simulated phase imbalance and signal path insertion losses of the transformer balun under the impedance matching conditions used in the doubler design [6] © 2016 IEEE.

metal layers. The dimensions were selected following [110] to optimize the IL, amplitude and phase imbalances, and bandwidth.

Input matching was completed by first pre-matching the differential input impedance $Z_{\text{in,diff}}$ of each SiGe HBT ($12.9 - j71\ \Omega$ at 76 GHz) to the impedance $Z_{\text{pre,diff}}$ ($6.3 - j33\ \Omega$ at 76 GHz) through a 200 fF DC-blocking MIM capacitor and a series microstrip line. The balun completes the input match to a single-ended input impedance (Z_{se}) of 50 Ω. Figure 4.4 shows that under these impedance matching conditions, the EM-simulated balun amplitude and phase imbalances are better than 1.0 dB and 4.5°, respectively, above 70 GHz. The signal path insertion losses of the balun, not including the 3 dB splitting loss, have minimum values of 1.63 dB and 0.95 dB at 78 GHz. The output of the push-push core was matched at the second harmonic using a short shunt stub

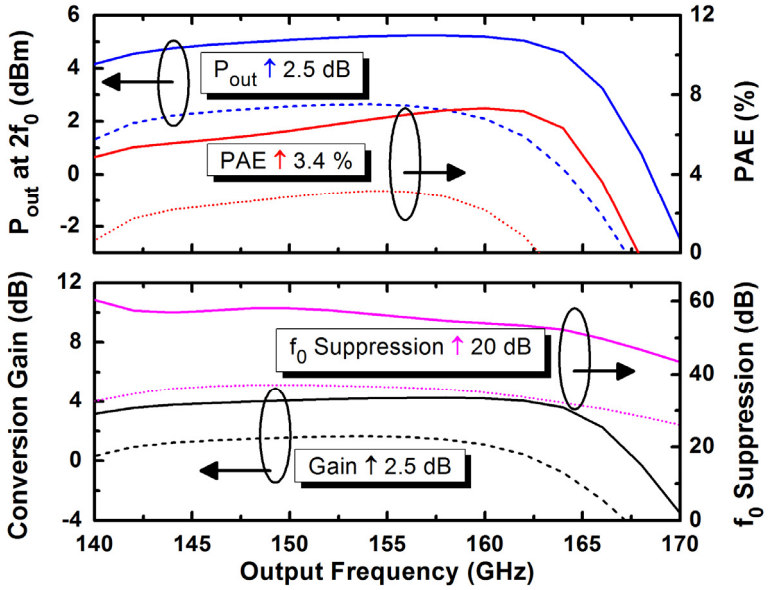

Figure 4.5: Simulated performance of the doubler with and without the output buffer stage (with P_{in} = 1 dBm) [6] © 2016 IEEE.

implemented using an on-chip microstrip line. Small resistors and decoupling capacitors were included on all bias lines to ensure stability.

The 500 GHz SG13G2 SiGe HBTs are well-suited for amplification in the upper D-band, and this amplification is a more power-efficient process than frequency multiplication. Therefore, for a desired fixed output power, higher conversion gain and power efficiency can be obtained by using a low-power doubling stage and output buffer than by using a doubling stage designed for a higher output power. A CE output buffer was implemented using a five-emitter SiGe HBT biased for peak f_{max} and sharing the push-push V_{CC} of 1.5 V. Figure 4.5 show that this buffer increases both the output power and conversion gain by 2.5 dB and the PAE by 3.4%. The tuned matching of the buffer increases the fundamental frequency suppression by 20 dB.

The buffer output was matched to 50 Ω on chip to enable monolithic receiver integration, so a matching section was designed to resonate the shunt capacitance of the

output bondpad, as shown in Figure 4.1. The simulated insertion loss of this network is 0.3 dB.

4.3 Doubler Measurements

The doubler circuit was characterized using wafer probes from GGB and Cascade Microtech. Return loss measurements were performed using Anritsu 3741A *W*-band extenders and OML V06VNA2-T/R *D*-band extenders. As shown in Figure 4.6, the

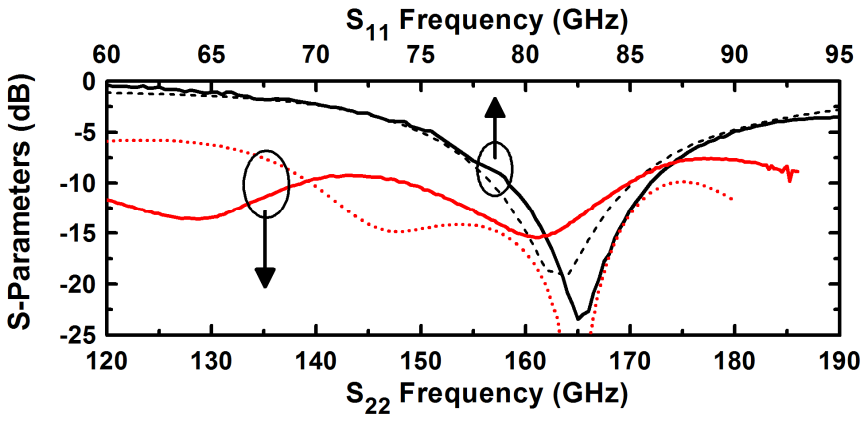

Figure 4.6: Measured (solid) and simulated (dashed) return loss of the SiGe HBT frequency doubler [6] © 2016 IEEE.

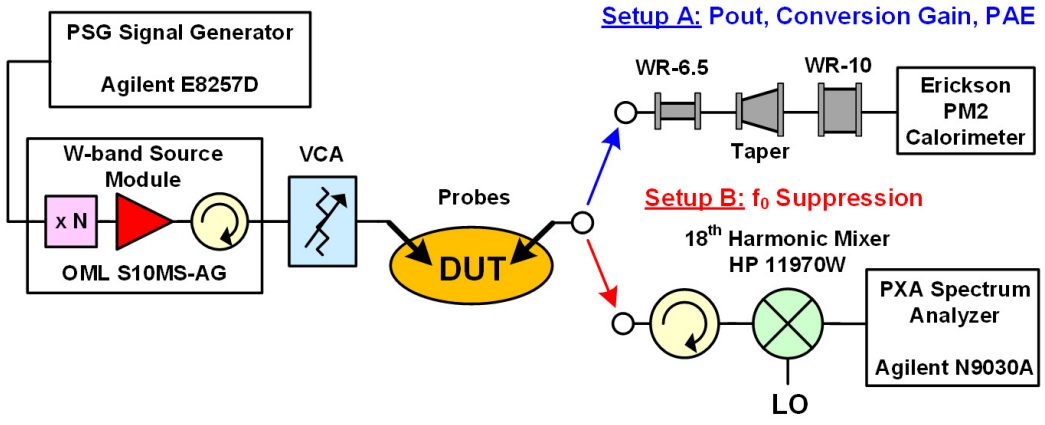

Figure 4.7: Block diagram of the swept-power measurement setup [6] © 2016 IEEE.

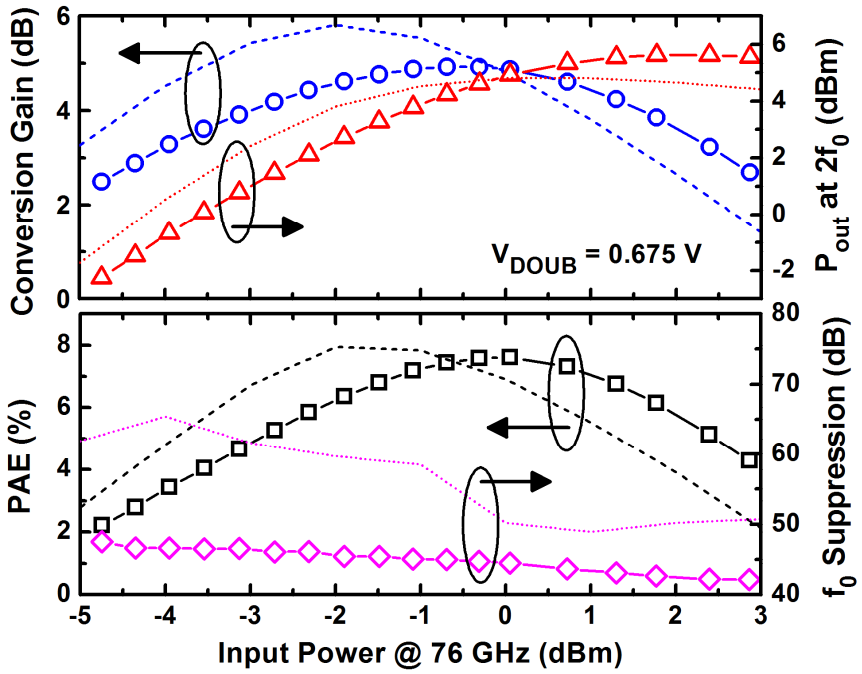

Figure 4.8: Measured (solid) and simulated (dashed) swept-power response with a 76 GHz input [6] © 2016 IEEE.

S-parameters agree well with simulation. The S_{11} is better than −5.0 dB across 76–90 GHz, and S_{22} is better than −9.0 dB below 172 GHz.

The swept-power measurement setup is shown in Figure 4.7. The input power was generated by a *W*-band source module and the input power was controlled by a voltage-controlled attenuator (VCA). The second harmonic output was measured using an Erickson calorimeter, and the fundamental frequency suppression was measured by down-converting the fundamental frequency to 300 MHz using a *W*-band harmonic mixer and detecting the amplitude using a spectrum analyzer.

The measured versus simulated swept-power response with a 76 GHz input is shown in Figure 4.8. Peak performance was obtained at a higher input power than simulated, but the overall agreement between measurement and simulation is close. A peak output power of 5.6 dBm is obtained with an input power of 1.8 dBm, and the peak

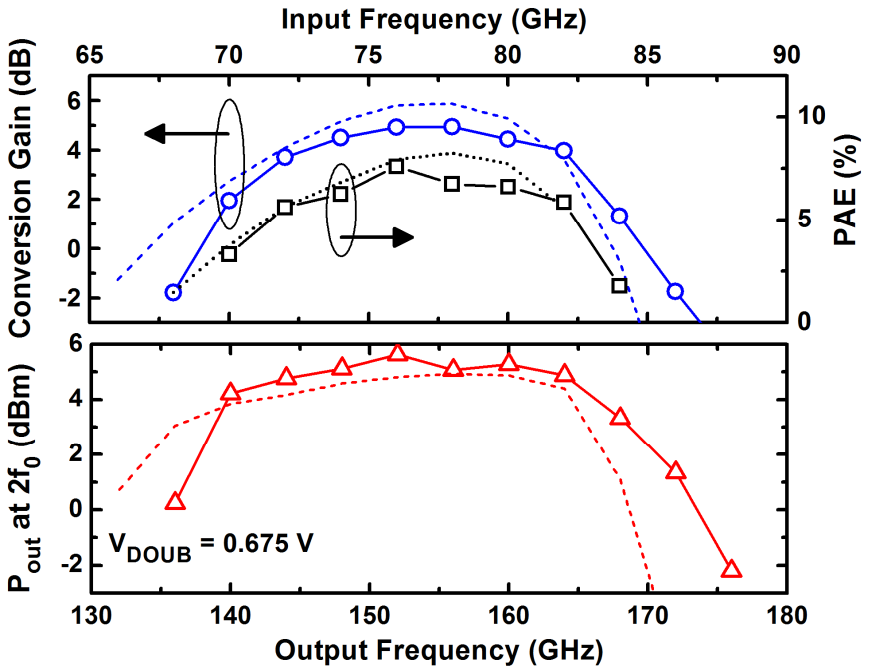

Figure 4.9: Peak measured (solid) and peak simulated (dashed) output power, conversion gain, and PAE versus frequency [6] © 2016 IEEE.

conversion gain of 4.9 dB is obtained with a −0.7 dBm input. The peak PAE of 7.6% is coincident with the peak conversion gain. The fundamental frequency suppression is lower than simulated, but is better than 42 dB across the power sweep.

The peak measured and peak simulated performance versus frequency are shown in Figure 4.9. Peak output power and conversion gain are obtained at 152 GHz, and the bandwidth is 138–170 GHz (20.8% fractional bandwidth). Figure 4.10 shows that the fundamental suppression across frequency with a 0 dBm input is better than 38.7 dB. The worst-case fundamental frequency suppression observed across all power and frequency sweeps is 37.0 dB.

Figure 4.11 shows the conversion gain and power-added efficiency (PAE) versus output power at 152 GHz for varying V_{DOUB}. A Class B V_{DOUB} of 0.650 V maximizes the output power, but a Class AB V_{DOUB} of 0.750 V yields more conversion gain for reduced

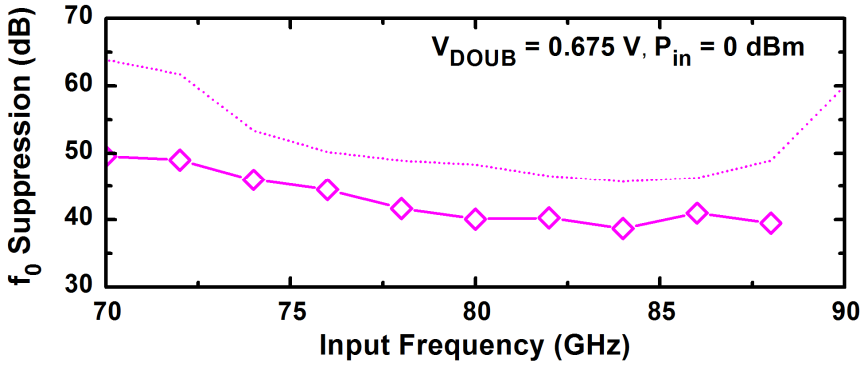

Figure 4.10: Measured (solid) and simulated (dashed) fundamental frequency suppression across input frequency (with P_{in} = 0 dBm) [6] © 2016 IEEE.

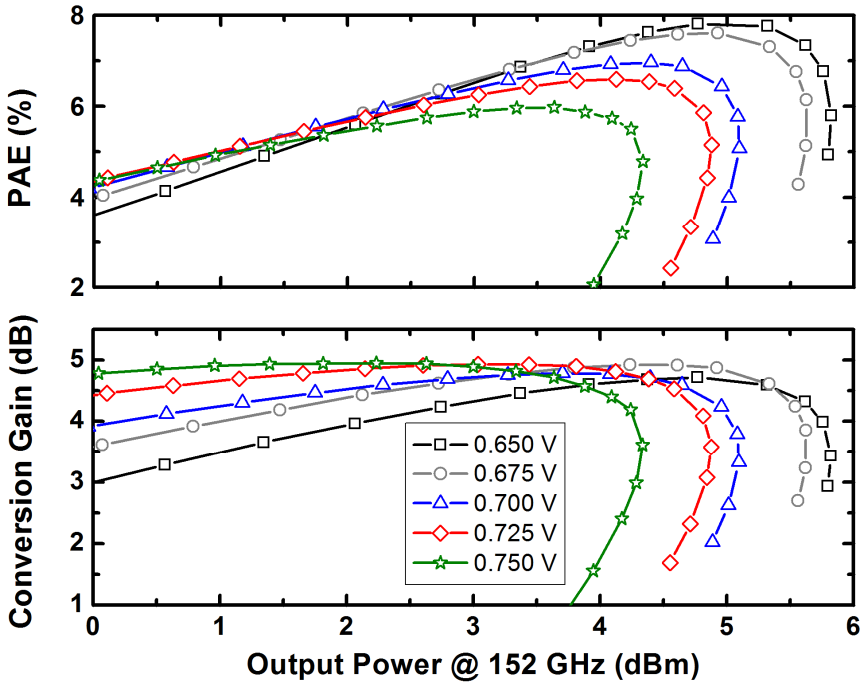

Figure 4.11: Measured conversion gain and PAE of the frequency doubler versus output power at 152 GHz, showing the impact of varying V_{DOUB} [6] © 2016 IEEE.

output powers. If the maximum output power is not required, V_{DOUB} can be increased to obtain higher conversion gain or more efficient operation for a given output power. Although the greatest overall efficiency is attained with an output power of 5 dBm, the

Table 4.1: Performance comparison with similar active frequency multipliers [6] © 2016 IEEE.

Ref.	Freq. (GHz)	Peak P_{out} (dBm)	Peak Gain (dB)	P_{DC} (mW)	Peak PAE (%)	Peak η_{total} (%)	Technology
This	138–170	5.6 / 5.9*	4.9 / 5.2*	36	7.6 / 8.4*	10.9 / 11.7*	130 nm SiGe HBT
[111]	124–138	-2.9	-3.2	7.2	-3.9	7.0	130 nm SiGe HBT
[112]	166–182	4.5	9.5	33.5	7.5	8.5	130 nm SiGe HBT
[113]	200–245	2	-15	35	-109.2	2.1	90 nm SiGe HBT
[114]	215–240	-1	13.5	630	0.1	0.1	130 nm SiGe HBT
[115]	135–160	3.5	-3	25	-11.1	7.5	45 nm SOI CMOS
[116]	119–135	10	7	45	17.8	26.0	250 nm InP DHBT
[117]	100–208	1.4	-7	14.4	-34.2	6.7	35 nm GaAs mHEMT
[118]	100–130	5	3	65	2.4	4.7	100 nm GaAs mHEMT

*Not including the simulated 0.3 dB insertion loss of the output pad matching section

efficient operation at reduced output powers enables flexible operation to satisfy the requirements of various systems.

This frequency doubler is benchmarked versus similar multipliers in Table 4.1. Many of the multipliers have conversion loss and negative PAE, so to ensure fair comparisons, we present both the peak PAE and the peak total power efficiency, which is given by

$$\eta_{\text{total}} = 100 \times \frac{P_{\text{out}}\,(\text{mW})}{P_{\text{in}}\,(\text{mW}) + P_{\text{DC}}\,(\text{mW})}. \tag{4.1}$$

To the best of the author's knowledge, this frequency doubler achieves the highest peak output power, fundamental frequency suppression, PAE, and total power efficiency of all *D*- and *G*-band SiGe HBT frequency doublers to date, and is competitive with the best III-V multipliers.

4.4 Summary

A 138–170 GHz SiGe HBT frequency doubler with a peak output power of 5.6 dBm has been presented in this chapter. The doubler achieves a peak conversion gain of 4.9 dB and a peak PAE of 7.6% through the use of a push-push frequency doubling stage optimized for low input drive along with a low-power output buffer. Although this doubler consumes DC power unlike passive multipliers, the DC power dissipation is only 36 mW at peak drive which is far lower than the hundreds of milliwatts consumed by typical power amplifiers which are needed when passive multipliers are used. A practical radiometer would need additional active frequency multipliers to produce the *E*-band input signal to this doubler, however, such multipliers would have higher conversion gain than this doubler due to their lower operating frequency, and these multipliers would need to generate an *E*-band output power of only 2 dBm. An all-SiGe active LO chain including this doubler would therefore be highly efficient and require only a low-power synthesizer, and would greatly improve the efficiency of radiometers for power-constrained CubeSats.

CHAPTER 5

INTEGRATED G-BAND SINGLE-SIDEBAND DOWNCONVERTER

5.1 Introduction

Compact and low-power IF subsystems can potentially enable high-quality soundings from CubeSats, as discussed in Chapter 3. Hyperspectral IF receiver modules are potentially compatible with a variety of millimeter-wave heterodyne receiver front-ends, provided that the front-ends perform single-sideband downconversion to the wide input bandwidth of the IF module. This concept is demonstrated by the Hyperspectral Microwave Atmospheric Sounder (HyMAS), an airborne instrument developed by MIT Lincoln Laboratory and NASA's Goddard Space Flight Center [86]. The HyMAS instrument performs all-weather sounding measurements through the use of millimeter-wave channels covering 108–119 GHz and 172–183 GHz. The noise in each millimeter-wave band is downconverted to an IF of 18–29 GHz for simultaneous channelization and detection by the compact hyperspectral receiver module. Each millimeter-wave receiver front-end is implemented using discrete waveguided components including a waveguide high-pass filter which performs image rejection, a passive subharmonic mixer, a passive frequency doubler, and an IF amplifier. The IF amplifier in each of the six receiver front-ends consumes 450 mW of DC power, and the LO generation consumes 8 W for each frequency band [88].

Significant reductions in the size and power consumption of these millimeter-wave receiver front-ends are needed to make these instruments suitable for use in the constrained payload of CubeSats. This chapter presents the design of a single-chip HyMAS-compatible

G-band single-sideband downconverter which is implemented using the IHP SG13G2 SiGe platform. The downconverter leverages the CE *G*-band LNA presented in Chapter 2 and the frequency doubler presented in Chapter 4 to achieve similar performance to the HyMAS *G*-band front-ends with significantly improved integration and power efficiency. The results of this work have not yet been submitted for publication.

5.2 Circuit Design

5.2.1 Downconverter Architecture

The *G*-band downconverter was designed to achieve a low NF and power dissipation with high mixer isolations and rejection of the noise in the image band. The downconverter consists of a front-end LNA, a mixer, and a frequency doubler, as shown in Figure 5.1. To achieve compatibility with the HyMAS system, the chip uses a fixed-frequency 77 GHz external LO to downconvert the 172–183 GHz upper sideband input noise to the 18–29 GHz IF bandwidth.

The core of the downconverter is a fundamental mixer implemented using a double-balanced topology to achieve high isolation between all ports. The balanced RF input to the mixer is generated using an on-chip Marchand balun to obtain a wide input bandwidth

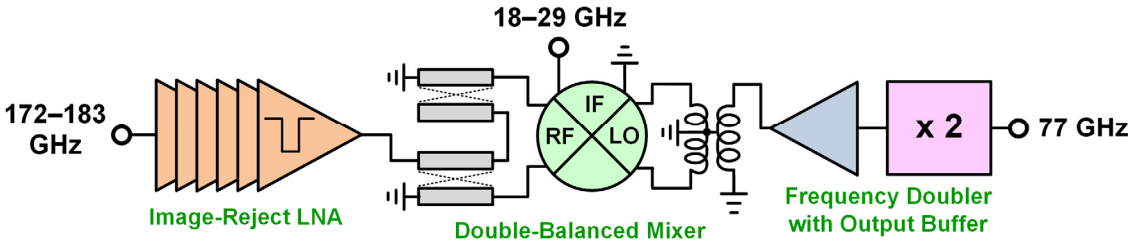

Figure 5.1: Block diagram of the SiGe HBT single-sideband downconverter.

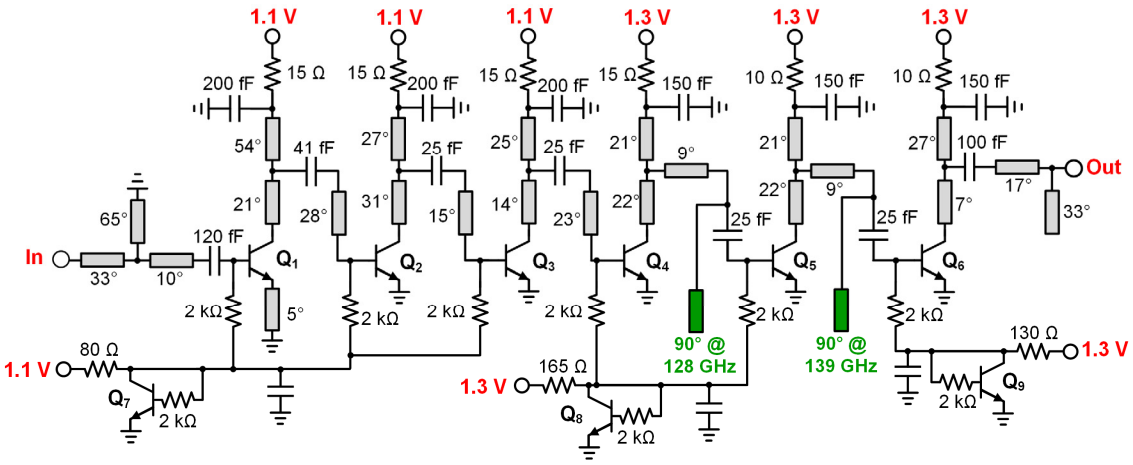

Figure 5.2: Simplified schematic of the *G*-band image-reject SiGe HBT LNA.

with low loss. The balanced LO input to the mixer is generated using a transformer-style balun to minimize the chip size while obtaining sufficient matching at 154 GHz. The mixer is driven by a power-efficient on-chip frequency doubler to emulate the operation of a subharmonic mixer without reducing the performance of the mixer. The LNA and frequency doubler (excluding the push-push doubling stage) were implemented using single-ended topologies to reduce the total power dissipation versus that of a fully differential system.

5.2.2 Image-Reject LNA

The front-end image-reject LNA is a modified version of the common-emitter (CE) *G*-band LNA presented in Section 2.3. A schematic of the modified six-stage LNA is shown in Figure 5.2. SiGe HBTs Q_1–Q_5 were implemented using the same three-emitter SiGe HBTs used in the previous CE LNA design, while Q_5 used a five-emitter SiGe HBT to enable a larger current swing and increased P_{1dB}. To improve the input matching from the original design, Q_1 utilized a small amount of inductive emitter degeneration which was implemented using a short microstrip trace. Each SiGe HBT was biased near peak f_{max}

to maximally suppress the noise of the last LNA stages and the mixer, although this slightly increased the NF of the LNA. The first three stages utilize shared current mirror biasing and a supply voltage of 1.1 V while the last three stages use a supply voltage of 1.3 V for an increased voltage swing.

Impedance matching was achieved through the use of on-chip microstrip lines implemented in the TM2 layer over the M2 ground plane along with small series MIM capacitors. The longest microstrip lines were meandered to reduce the chip area. The input matching network utilized 10 μm wide TM2 traces (Z_0 = 56 Ω) to minimize passive losses while all other microstrips used smaller 6 μm wide (Z_0 = 66 Ω) traces. To reduce the gain at lower out-of-band millimeter-wave frequencies without impacting the in-band NF, the shunt matching stubs at the collectors of Q_1–Q_6 were implemented using short trace lengths along with under-sized 150 fF AC-grounding MIM capacitors. These techniques slightly reduced the in-band gain, but suppressed undesired gain and ensure stable operation in the *W*-band frequency range.

The single-sideband downconverter requires image rejection to prevent noise from the undesired 125–136 GHz lower sideband from being folded into the 18–29 GHz IF bandwidth. The tuned matching networks of the LNA did not sufficiently reject the image band, so additional image rejection was required. To avoid the significant complexity, chip area, and power dissipation required to implement a double-balanced *G*-band image-reject mixer on-chip, image filtering was integrated into the *G*-band LNA. The fractional bandwidth of the image band is only 8.4%, so this filtering was implemented using simple quarter-wave open stub notch filters.

Notch filters using a variety of signal trace widths were laid out and EM-simulated to determine the optimal filter implementation. As shown in Figure 5.3, low-impedance traces achieve a deeper notch and a wider stopband than higher-impedance traces. However, the wideband lower-impedance traces are lossier and more reflective in the desired band than the narrowband high-impedance traces. Narrow 2 μm traces were used in the notch filters to minimize the impact of the filters on the LNA performance in the desired band. To ensure a conservatively wide image rejection bandwidth, two notch filters with offset frequencies were employed, one centered at 139 GHz and the other at 128 GHz as shown in Figure 5.4. The simulated gain of the LNA slowly rolls off in the image band with decreasing frequency, as shown in Figure 5.5, so the resonance frequencies of the notch filters were increased in frequency with respect to the edges of the image band to obtain high image rejection across a wider overall bandwidth.

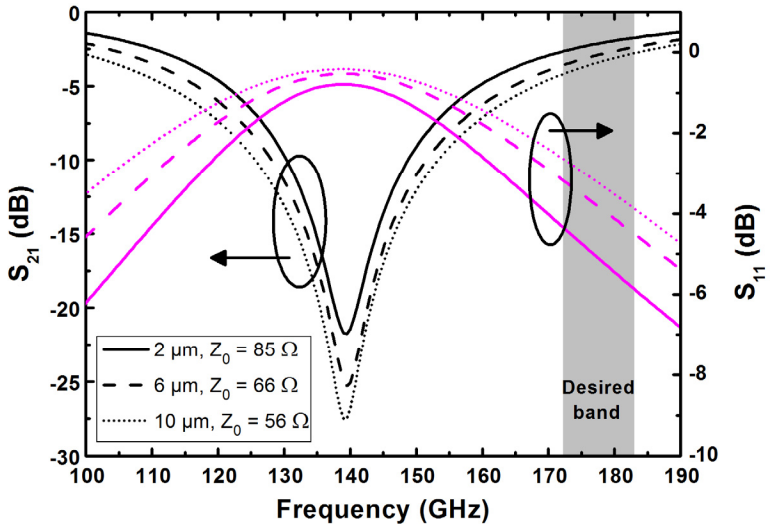

Figure 5.3: EM-simulated S_{21} and S_{11} of the 139 GHz quarter-wave open stub notch filter, showing the effect of the signal trace width on the filter response. The desired band is shaded.

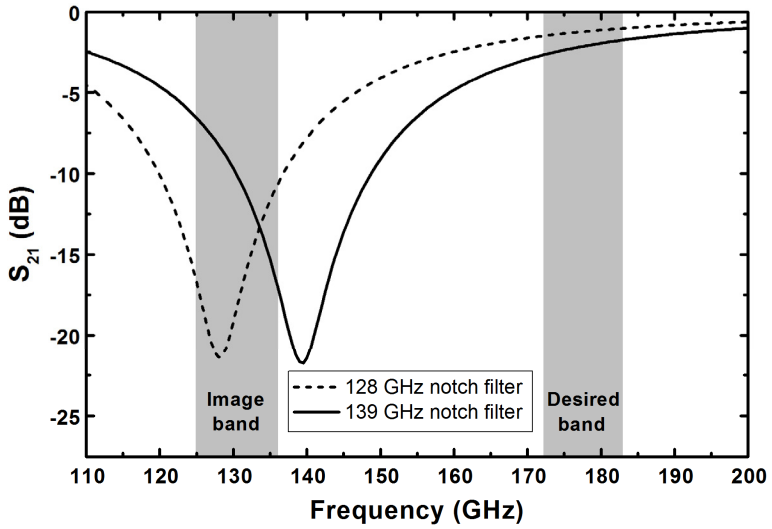

Figure 5.4: EM-simulated S_{21} of the two notch filters used in the image-reject LNA. The image band and desired band are shaded.

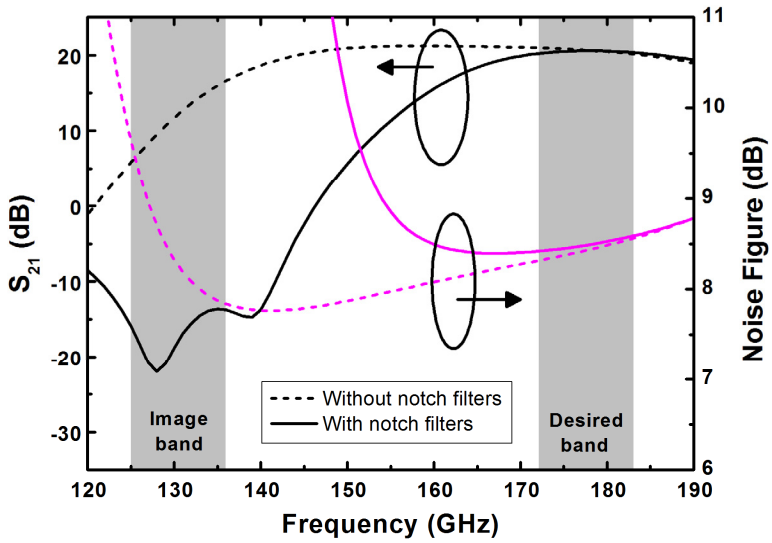

Figure 5.5: Simulated gain and NF of the *G*-band LNA with and without the embedded notch filters. The image band and desired band are shaded.

The notch filters were separately integrated into the last two interstage matching networks in the LNA, as shown in Figure 5.1. The 128 GHz filter was placed before the 139 GHz filter, as the 128 GHz filter introduces less loss into the desired band than the 139 GHz filter and therefore has less of an impact on the cascaded NF of the LNA. SiGe HBTs Q_5 and Q_6 provide isolation between the two filters and ensure a non-reflective

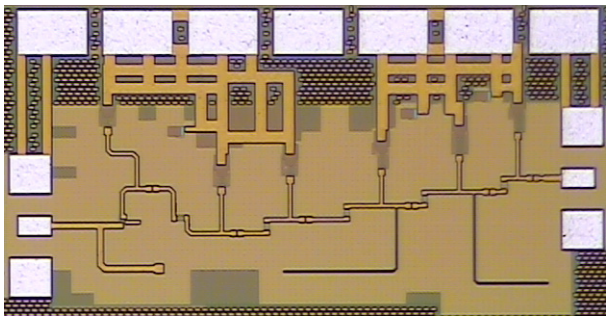

Figure 5.6: Die microphotograph of the standalone *G*-band image-reject LNA. The chip size is 1.06 mm × 0.53 mm with bondpads and 0.87 mm × 0.4 mm without bondpads.

output impedance in the rejected image bandwidth. The simulation results in Figure 5.5 show that the LNA rejects the entire image band by more than 34 dB, and 20 dB of image rejection is attainable with an IF frequency as low as 9 GHz. The filters increase the NF in the desired band by a mean of 0.06 dB and decrease the gain by a mean of 0.2 dB.

A die photograph of the fabricated standalone *G*-band image-reject LNA is shown in Figure 5.6. The LNA has a simulated bandwidth of 163–197 GHz with a peak gain of 20.6 dB at 178 GHz. The simulated NF ranges between 8.4–9.0 dB across the bandwidth, and the simulated input-referred P_{1dB} is -20 dBm at 180 GHz. The power dissipation of the full LNA is 46 mW.

5.2.3 Double-Balanced Mixer

The *G*-band mixer was implemented using a double-balanced Gilbert cell topology with resistive loads to achieve low NF and conversion loss with high isolation between all ports. A schematic of the mixer is shown in Figure 5.7. The SiGe HBTs in the mixing quad, Q_3–Q_6, were implemented using SiGe HBTs with two emitter stripes each to minimize the required LO drive level while avoiding the increased parasitic resistance and degraded performance of the minimum-size single-emitter SiGe HBTs.

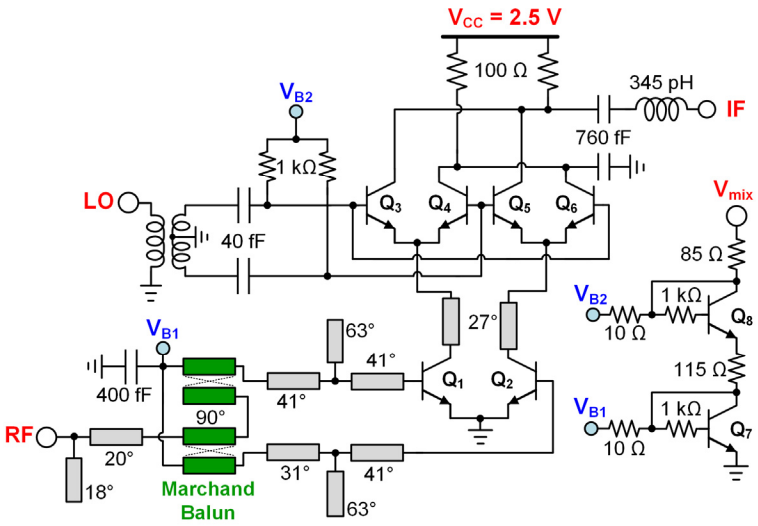

Figure 5.7: Schematic of the *G*-band SiGe HBT double-balanced mixer.

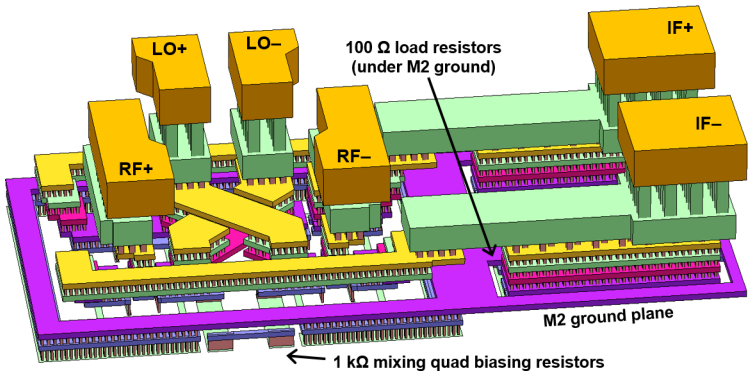

Figure 5.8: 3-D model of the SiGe HBT mixing quad layout.

The mixing quad layout was designed to minimize the resistive and inductive parasitics on the millimeter-wave RF and LO ports while maintaining symmetry to maximize the isolations. A 3-D model of the mixing quad layout is shown in Figure 5.8. The performance-critical *G*-band RF inputs used wide via transitions from top metal directly into the mixing quad core, while the less-critical LO inputs utilized a wide and symmetric crossing structure to minimize the delay between the SiGe HBTs driven by each LO input. The lower-frequency IF outputs were laid out using staggered vertical via transitions to reduce the coupling to the LO and RF via stacks and were routed horizontally

using shunt-connected M4 and M5 metallization to reduce the parasitic inductance and resistance. Due to the complexity of this layout, the mixing quad interconnects were modeled using RC parasitic extraction instead of Sonnet to avoid inaccuracies due to the use of internal ports at high millimeter-wave frequencies.

The two SiGe HBTs in the transconductance (g_m) stage, Q_1 and Q_2, were each implemented using four-emitter SiGe HBTs to maintain the same current density as the SiGe HBTs in the mixing quad while obtaining near-maximum gain from each device. Series microstrip lines were connected between the g_m stage and the mixing quad to increase the conversion gain following [120]. Bias voltages for each stage were generated by an on-chip current mirror which was implemented using single-emitter SiGe HBTs to minimize the power dissipation.

A particular challenge in the design of this mixer was achieving the desired single-ended IF output with an 18–29 GHz bandwidth. Converting the differential output to single-ended was necessary to enable compatibility with existing systems. Low-frequency passive combiner are physically large, while active differential combiners would increase the power dissipation and require tuning. To avoid these issues, one of the differential IF outputs was AC-grounded on-chip while the other was taken as the single-ended output. This method reduced the conversion gain by 3 dB, but enabled a wideband single-ended output without trading off power or chip area. The IF matching was attained by using 100 Ω load resistors in conjunction with a 760 fF DC-blocking MIM capacitor and a 345 pH series inductor. Through the use of this technique, the IF port achieves a simulated return loss of greater than 10 dB from 16–39 GHz.

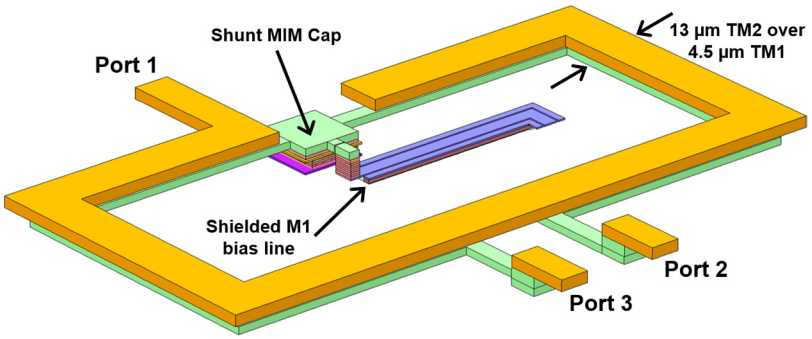

Figure 5.9: 3-D model of the *G*-band Marchand balun layout, not showing the M2 ground plane which is under the entire structure.

A wide matching bandwidth on the LO port was not required due to the fixed-IF operation, so the LO matching bandwidth was traded off for reduced area. Sufficient matching was obtained through the use of 40 fF series MIM capacitors and the winding inductance of a compact 154 GHz transformer balun implemented in an identical manner to the 77 GHz transformer balun used in the frequency doubler (see Section 4.2). The simulated 10 dB return loss bandwidth for the LO port is 147–170 GHz.

The matching network for the RF port was designed to achieve a wide RF bandwidth with low insertion loss. Each differential RF input was matched to 50 Ω using 66 Ω microstrip lines and open stubs. Single-ended to differential conversion was performed by a custom-designed Marchand balun, as shown in Figure 5.9. The balun was implemented using broadside-coupled TM2 over TM1 metallization, and the width of the signal trace in each layer was selected to achieve a 50 Ω Z_0 (13 μm for TM2 and 4.5 μm for TM1). The balun AC ground was implemented using a 400 fF shunt MIM capacitor, and the biasing for the g_m stage was routed under the M2 ground plane using shielded bias lines and injected at the AC ground node. The phase imbalance between the outputs of the Marchand balun is 10°, so a short meandered microstrip length was used to correct for this imbalance. As shown in Figure 5.10, the phase-corrected balun achieves EM-simulated

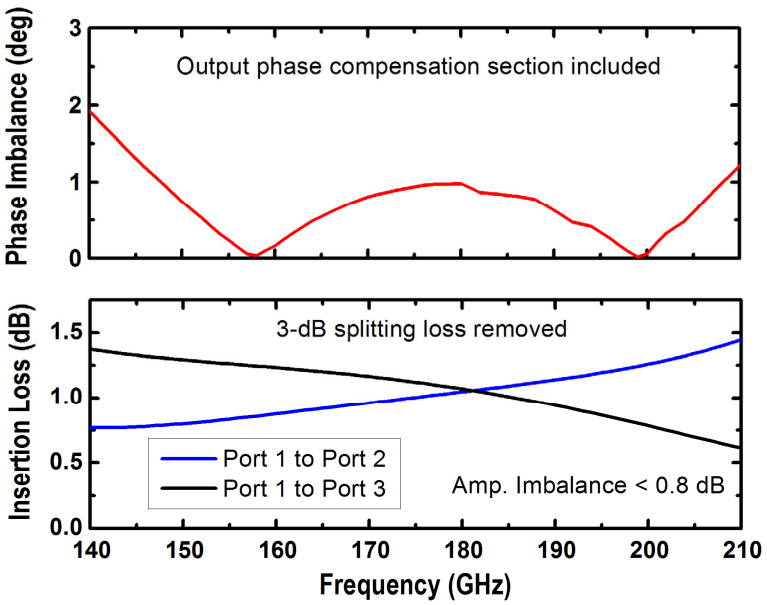

Figure 5.10: EM-simulated insertion loss and phase imbalance of the *G*-band Marchand balun.

amplitude and phase imbalances of better than 2° and 0.8 dB, respectively, across 140–210 GHz. The signal path insertion losses of this balun, not including the 3 dB splitting losses, are less than 1.5 dB. The single-ended input match was completed using an open stub, and the resulting simulated 10 dB return loss bandwidth for the RF port is 132–209 GHz.

The mixer was integrated with the frequency doubler presented in Chapter 4. A die photograph of the integrated mixer-doubler chip is shown in Figure 5.11. The simulated mixer has a midband conversion loss of 5 dB, a SSB NF below 18 dB from 167–183 GHz, and LO-to-IF and LO-to-RF isolations of greater than 48 dB and 50 dB, respectively. The simulated midband input-referred P_{1dB} of -7 dBm is sufficient for this application. The DC power dissipation of the mixer is 14 mW when driven at the optimal LO power level, which is dependent on the biasing of the frequency doubler.

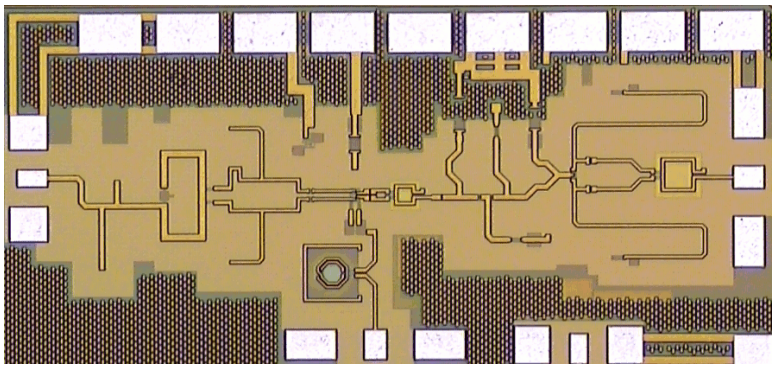

Figure 5.11: Die microphotograph of the integrated mixer and frequency doubler. The size of the chip is 1.49 mm × 0.70 mm including bondpads.

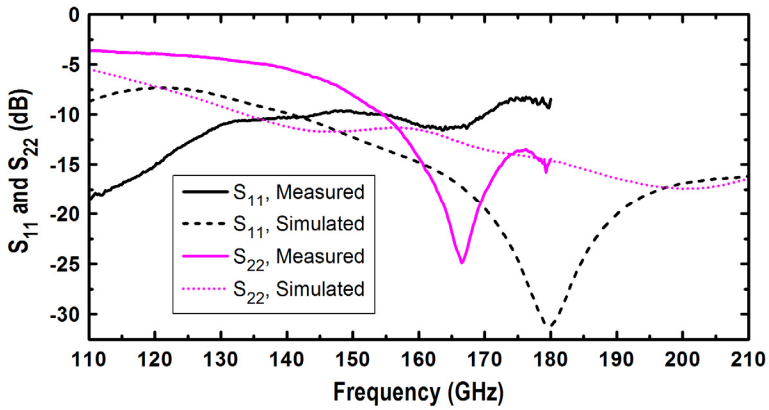

Figure 5.12: Measured and simulated S_{11} and S_{22} of the *G*-band image-reject LNA.

5.3 Measurements

5.3.1 Image-Reject LNA

The S-parameters of the LNA were measured on-chip using V06VNA2 D-band VNA extenders from OML, Inc. The measured and simulated S_{11} and S_{22} of the LNA are shown in Figure 5.12. The input and output return losses slightly differ from simulation, but are generally well-matched across 140–180 GHz. The S_{11} and S_{22} are better than -8 dB and -13 dB, respectively, in the measured portion of the desired 172–183 GHz band—a significant return loss improvement versus the previous *G*-band CE LNA (see Figure 2.23).

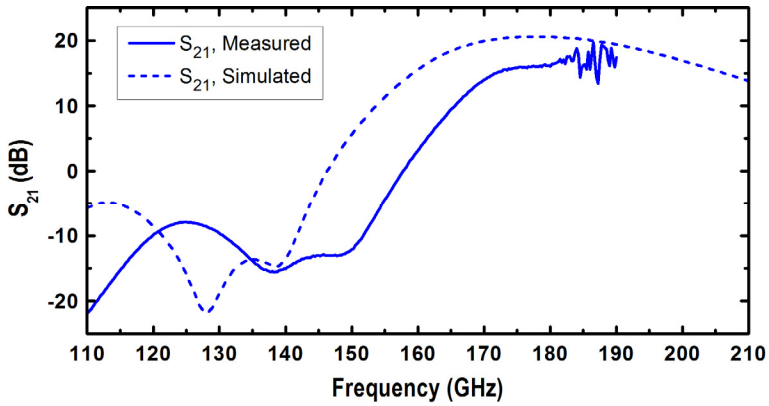

Figure 5.13: Measured and simulated S_{21} of the *G*-band image-reject LNA.

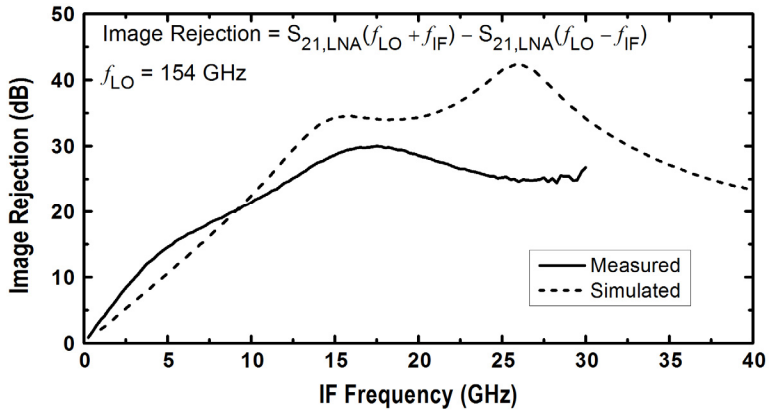

Figure 5.14: Measured and simulated image rejection of the *G*-band image-reject LNA versus IF frequency, assuming a 154 GHz LO.

Figure 5.13 shows the measured and simulated S_{21} of the amplifier. The measured S_{21} curve, including the resonant frequencies of the notch filters, shifted up in frequency from simulation by roughly 10 GHz, and the midband gain is reduced from simulation by more than 4 dB. The shifted resonance frequencies of the notch filters indicate inaccuracies in the modelling of the high-impedance microstrip lines, which are potentially due to the 2.5D nature of the Sonnet software or inaccuracies in the electromagnetic parameters of the substrate provided by the foundry. The reduction in the midband gain from simulation is partially caused by the in-band impact of the up-shifted notch filters. The measured versus simulated image rejection provided by the image-reject amplifier is shown in Figure

5.14. Although the notch filter resonance frequencies increased from simulation, the measured image rejection is greater than 20 dB for IF frequencies above 9 GHz and greater than 24 dB across 18–30 GHz. Despite the discrepancies between measurement and simulation, the amplifier sufficiently rejects the noise in the image band of the mixer.

The gain and NF of the image-reject LNA were measured on-chip across 160–210 GHz using the Y-factor method in a method similar to that described in Section 2.3.4. A 90° WR-5.1 E-plane bend with an upward-pointing WR-5.1 conical horn antenna was connected to the WR-5.1 input-side wafer probe. Manually-chopped measurements were performed one frequency at a time by holding sheets of downward-pointing ECCOSORB AN-72 absorber above the horn antenna, with one sheet at ambient temperature and the other in an LN_2-filled EPS foam bucket. The noise receiver is nearly identical to the one shown in Figure 2.29, with the only difference being the use of an Agilent N9030A PXA signal analyzer instead of an Agilent E4446A PSA spectrum analyzer.

The measured gain along with the measured and simulated NF are shown in Figure 5.15. The gain measured using the Y-factor method closely matches the measured S_{21}, and the LNA achieves a mean gain of 15.7 dB across 172–183 GHz with a 3-dB bandwidth of 169–199 GHz. The measured NF is less than 9.0 dB from 165–195 GHz, and the mean NF across 172–183 GHz is 8.6 dB. The close agreement between the measured and simulated NF indicates that the reduced midband gain from simulation is caused by inaccurate modelling of elements used in the last stages of the LNA, which have a small impact on the NF. In addition to the notch filters, errors in the modeling of the small-sized MIM capacitors used to AC-grounding the shunt stubs or the polysilicon resistors used to ensure low-frequency stability may contribute to this gain discrepancy.

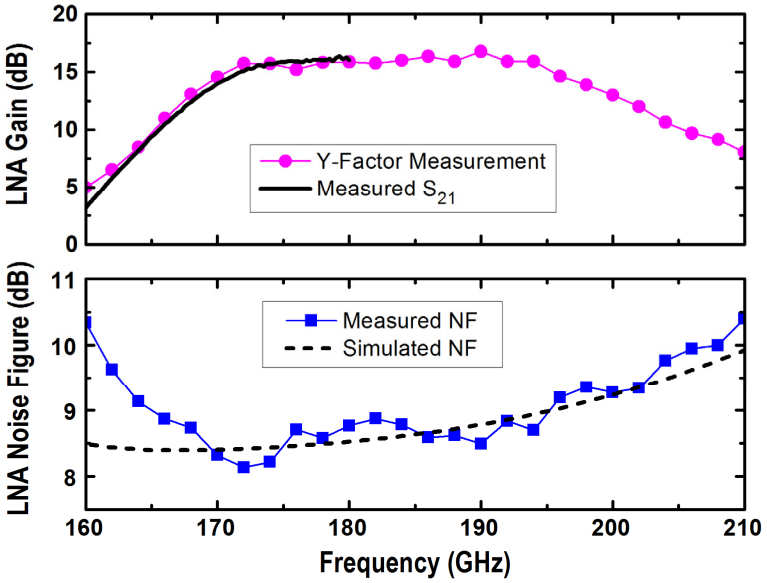

Figure 5.15: Measured gain along with the measured and simulated NF of the image-reject amplifier. The gain measured by the Y-factor method shows close agreement with the measured S_{21}.

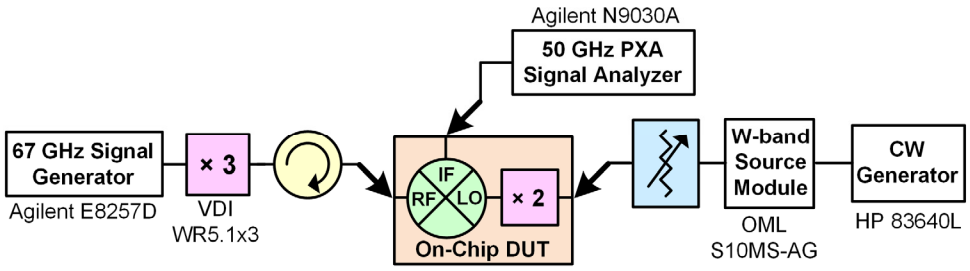

Figure 5.16: Block diagram of the mixer conversion loss measurement setup.

5.3.2 Integrated Mixer and Frequency Doubler

A block diagram of the measurement setup used to measure the conversion loss of the integrated mixer and frequency doubler is shown in Figure 5.16. The *G*-band RF input signal was generated using a WR5.1 tripler along with a 67 GHz signal generator. The fixed RF input power for the conversion loss measurements was selected to be -23 dBm, which is over 10 dB below the simulated mixer P_{1dB} of -10 dBm yet was high enough to be accurately calibrated using an Erickson PM2 calorimeter. The fixed 77 GHz LO was

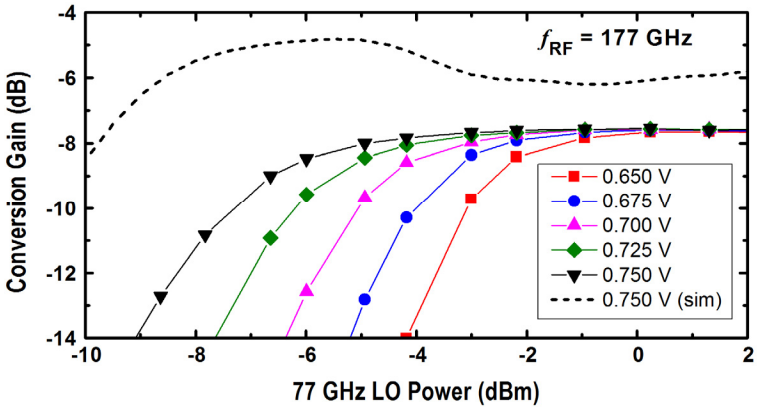

Figure 5.17: Measured conversion gain of the integrated mixer and frequency doubler at 177 GHz versus LO power for multiple values of the input bias voltage to the push-push frequency doubling stage, V_{DOUB}, along with the simulated performance at V_{DOUB} = 0.750 V.

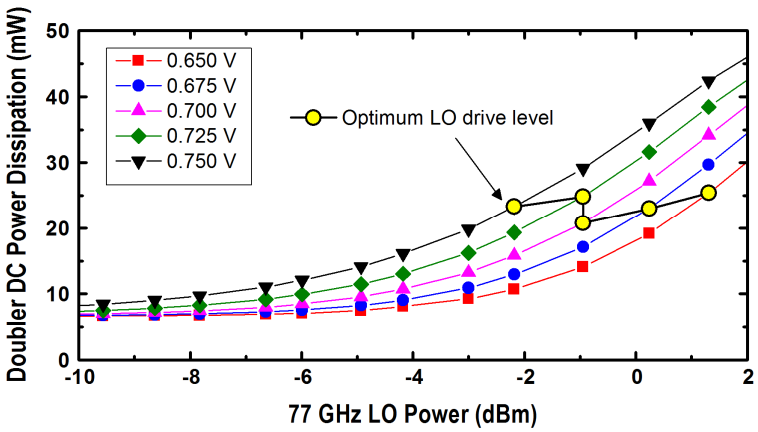

Figure 5.18: Measured DC power dissipation of the frequency doubler versus LO power for multiple values of V_{DOUB}. The optimum LO drive levels show that V_{DOUB} can be adjusted to reduce the LO power without increasing the DC power dissipation.

generated by an OML W-band source module along with a variable attenuator, and a 50 GHz Agilent N9030A PXA signal analyzer measured the high-frequency IF output.

Figure 5.17 shows the measured conversion gain of the integrated frequency-doubled mixer versus LO power at 77 GHz. To maximize the power efficiency of the frequency doubler and minimize the LO drive level, the conversion gain was measured versus LO power for multiple values of V_{DOUB}, the input bias voltage to the push-push

frequency doubling stage, following the analysis presented in Section 4.3. The conversion loss saturates at 7.6 dB for every value of V_{DOUB}, although the required LO power to achieve this saturated conversion loss decreases significantly with increasing V_{DOUB}. To evaluate which value of V_{DOUB} maximizes the efficiency, the DC power dissipation of the frequency doubler versus LO power and the optimum LO drive level for each value of V_{DOUB} are shown in Figure 5.18. The DC power dissipation of the doubler at the optimum LO drive level is nearly constant, therefore V_{DOUB} was selected to be 0.75 V to achieve the minimum saturated LO drive level of -2 dBm. At this drive level, the DC power dissipation of the frequency doubler is 23 mW.

The simulated results in Figure 5.17 show that the optimum LO drive level of -2 dBm is more than 3 dB higher than simulated. This discrepancy from simulation is potentially due to insufficient modeling of the parasitics in the complex mixing quad layout, which could not be accurately EM simulated and was modeled using RC parasitic extraction as described in Section 5.2.3. The increased LO drive level could also be caused by a shift from simulation in the relatively narrowband impedance match at the 154 GHz internal LO port of the mixer. The mixer was integrated with on-chip with the frequency doubler, and the return loss of the 154 GHz LO port could therefore not be measured.

The measured and simulated conversion loss of the frequency-doubled mixer across RF and IF frequency are shown in Figure 5.19. The conversion loss is 4 dB higher than simulated, but is lower than 10 dB across 159–194 GHz with a mean value of 8.6 dB across 172–183 GHz. The increased loss from simulation is potentially caused by inaccuracies in the modeling of the SiGe HBTs, the 100 Ω polysilicon load resistors, or the parasitics of the mixing quad layout.

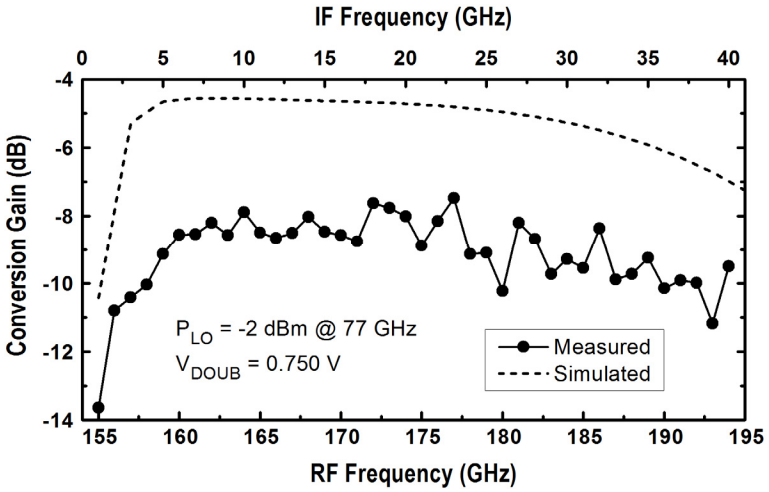

Figure 5.19: Measured and simulated conversion gain across frequency of the integrated frequency-doubled mixer.

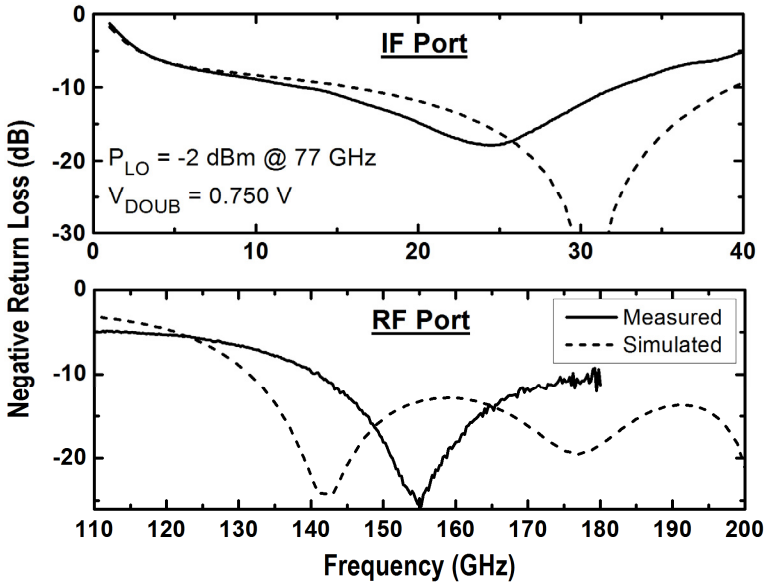

Figure 5.20: Measured and simulated return losses of the RF and IF ports of the mixer.

Figure 5.20 shows the measured and simulated return losses of the RF and IF ports of the mixer under optimal LO drive. The impedance matching of the IF port is shifted down in frequency from simulation, yet the return loss is better than 12 dB across 18–30 GHz. The return loss of the RF port shifted up in frequency from simulation and is greater than 10 dB across 172–180 GHz.

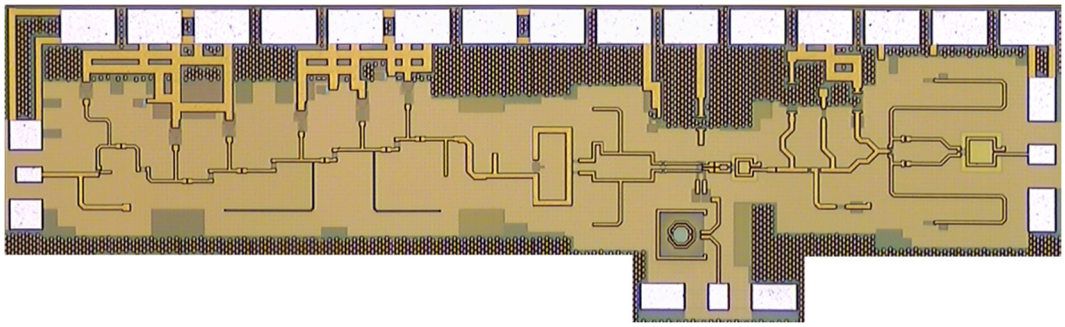

Figure 5.21: Die microphotograph of the integrated *G*-band single-sideband downconverter. The size of the chip is 2.37 mm × 0.70 mm.

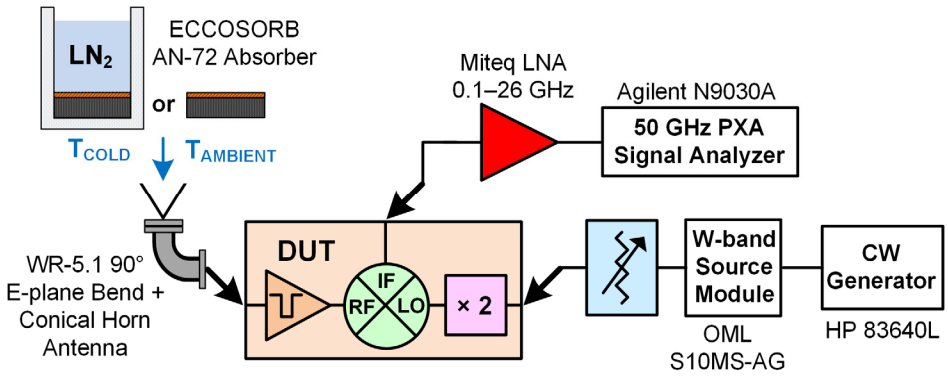

Figure 5.22: Block diagram of the Y-factor measurement setup used to characterize the integrated downconverter.

5.3.3 Integrated Downconverter

A photograph of the fabricated single-sideband downconverter chip is shown in Figure 5.21. The chip consumes 82 mW of DC power when driven with an LO of -2 dBm at 77 GHz. The conversion gain and SSB NF of the downconverter were measured using the Y-factor method, and a block diagram of the measurement setup is shown in Figure 5.22. The input noise was generated by the same hot and cold ECCOSORB AN-72 loads used to measure the image-reject LNA. The output noise at the IF port of the downconverter was measured by an Agilent N9030A PXA signal analyzer, and a 0.1–26 GHz LNA from Miteq was used to overcome the losses of the output cabling and the NF of the PXA. The SSB NF was measured for IF frequencies above 10 GHz, where the *G*-band LNA provides

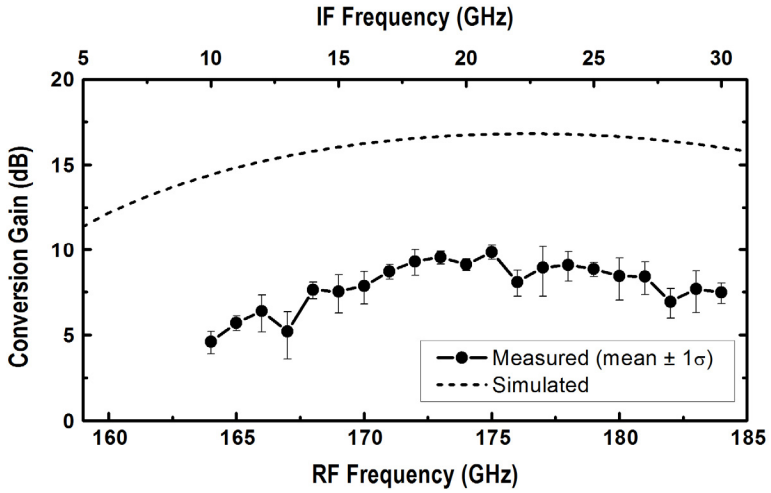

Figure 5.23: Measured and simulated conversion gain of the integrated downconverter across frequency. The displayed points represent the mean of the four measurements at each frequency point plus or minus one standard deviation.

more than 20 dB of image rejection. The IF LNA limited the upper IF frequency in measurement to 30 GHz. The measured Y-factor at every frequency was less than 0.25 dB, so to reduce the uncertainty, four manually chopped measurements were performed at each frequency point. The displayed data is the mean of the four measured values at each frequency, and the error bars represent one standard deviation.

The measured and simulated conversion gain of the integrated downconverter across frequency is shown in Figure 5.23. The gain is 8 dB lower than simulated, which was expected due to the 4 dB gain reductions from simulation observed in the measurements of the image-reject LNA and the frequency-doubled mixer. The mean measured conversion gain across the 172–183 GHz application bandwidth is 8.7 dB. The expected gain obtained by summing the mean measured gains of the standalone image-reject LNA and the frequency-doubled mixer across this bandwidth is only 7.1 dB, which indicates that integrating the mixer and LNA reduced losses by eliminating the bondpad-to-probe transitions at the LNA output and the mixer input.

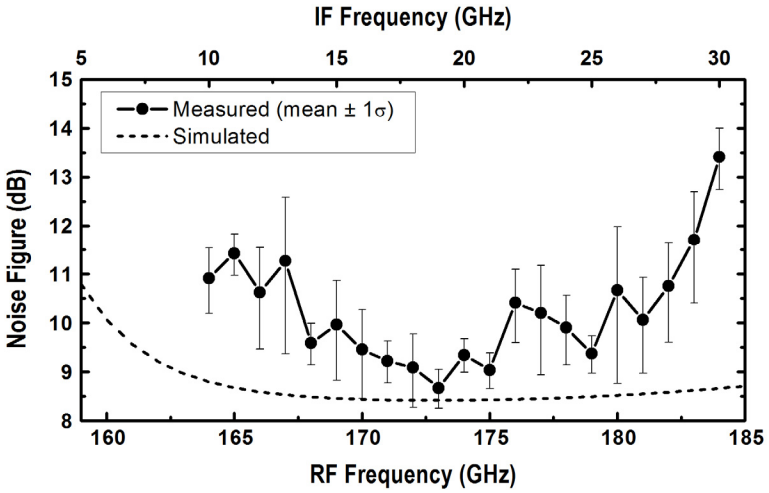

Figure 5.24: Measured and simulated NF of the integrated downconverter across frequency. The displayed points represent the mean of the four measurements at each frequency point plus or minus one standard deviation.

The measured and simulated NF of the integrated downconverter are shown in Figure 5.24. The uncertainty in the measured NF is higher than that of the image-reject LNA due to the higher system NF and the significantly increased IF measurement frequencies. The mean measured NF across the 172–183 GHz application bandwidth is 9.9 dB, while the simulated mean NF was 8.5 dB. This increase from simulation is caused by the reduced gain of the LNA in conjunction with an increased mixer NF due to the increased conversion loss from simulation. The simulated NF of the frequency-doubled mixer was less than 18 dB, whereas a cascaded analysis using the measured gain and NF of the downconverter and the image-reject LNA indicates that the SSB NF of the mixer is 20 dB. The conversion gain and NF of the downconverter could likely be improved with proper design optimizations.

Table 5.1: Performance comparison with similar state-of-the-art *G*-band downconverter MMICs.

Reference	This work	[74]	[120]	[78]	[121]
Topology	Image-reject LNA, mixer, LO × 2	LNA, IQ SHM, VCO, prescaler	LNA, mixer, LO buffer, IF VGA	LNA, subharmonic mixer	LNA, mixer, LO × 2, LO buffer
Technology	0.13 μm SiGe HBT	250 nm SiGe HBT	0.13 μm SiGe HBT	250 nm SiGe HBT	0.1 μm GaAs mHEMT
f_{max} (GHz)	450	350	450	435	300
RF BW (GHz)	172–183	150–162	170–205	202–230	196–204
IF BW (GHz)	18–29	Baseband	0.1–25	0–10	Baseband
External LO Freq. (GHz)	77	N/A (VCO)	190	110	100
External LO Power (dBm)	-2	N/A (VCO)	-20	0	-13
P_{diss} (mW)	82	490	122	216	270
Gain (dB)	8.7	35	47	16	7
NF (dB)	9.9 (SSB)	8.5 (DSB)	10.7 (DSB)	15 (DSB)	6.9 (DSB)
Area (mm^2)	1.66	0.90	1.24	0.66	4.0

5.4 Summary

This chapter presented the design and characterization of a monolithically integrated *G*-band single-sideband downconverter for hyperspectral humidity-sounding radiometers. Over 24 dB of image rejection is attained across the 172–183 GHz application bandwidth through the use of quarter-wave open stub notch filters integrated into the front-end *G*-band LNA. The mean SSB conversion gain and NF across the band are 8.7 dB and 9.9 dB, respectively, and both values can be improved with proper design optimizations. The chip achieves this performance with a 77 GHz LO drive level of only -2 dBm at which

the chip dissipates only 82 mW of power due to the use of a low-power active mixer which is driven by an optimally-biased power-efficient SiGe HBT frequency doubler.

The SiGe HBT downconverter is compared to similar monolithically integrated *G*-band downconverters in Table 5.1. To the best of our knowledge, this receiver front-end achieves the best SSB NF of all G-band SiGe HBT downconverters to date, and is competitive with the best demonstrated III-V downconverter MMICs. This SiGe MMIC demonstrates significant functionality while dissipating much less power than similar state-of-the-art downconverters, and although additional frequency multiplication and IF amplification would be needed to use this MMIC in practical radiometers, those blocks could be implemented on-chip with a small increase in the overall power consumption as demonstrated in Chapters 3 and 4.

The results of this work highlight the ability of cutting-edge SiGe HBT technologies to develop integrated and low-power millimeter-wave receiver front-ends with competitive performance to GaAs and InP receivers. SiGe HBT downconverters can potentially enable significant reductions in the SWaP of radiometer receivers for CubeSats. For example, the 118 GHz radiometer front-end launched on the MicroMAS CubeSat consists of three separate waveguide modules which contain two LNA MMICs, a weakly coupled noise diode, a HEMT diode mixer, and a resistive diode tripler. The receiver achieves 20 dB of gain with 5 dB NF, however, the packaged receiver has a volume of 2.5 in^2, a mass of 60 g, and requires 650 mW to generate the 0 dBm LO signal at 90 GHz [10,24,107]. Integrated SiGe receivers could improve the integration and the power efficiency of the frequency multiplication while achieving similar RF performance. However, the *G*-band receiver launched on JPL's RACE CubeSat [27] and the *G*-band

receivers in proposed for use in the TEMPEST CubeSats [17] utilize InP HEMT LNAs which have achieved packaged LNA NFs as low as 3.4 dB at 183 GHz [70]. The low NF of these LNAs can enable superior radiometric performance to the SiGe HBT LNAs and downconverters presented here. Therefore, until the *G*-band NF of SiGe HBTs becomes more competitive, the optimal approach to implement *G*-band receiver front-ends for CubeSats may be to one InP LNA to set the receiver NF followed by a low-power integrated SiGe downconverter to obtain the SWaP benefits enabled by SiGe.

CHAPTER 6

COMPACT AND LOW-LOSS 60 GHZ SIGE HBT SPDT SWITCHES

6.1 Introduction

Radiometer systems for scientific applications typically apply square-wave modulation to the input noise in order to eliminate measurement uncertainties due to short-term receiver gain fluctuations, as was discussed in Section 1.2. This functionality is often implemented by placing a single-pole double-throw (SPDT) switch at the front of the receiver, with one throw connected to the antenna and the other connected to a matched load at ambient temperature. A switch that performs this function is referred to as a Dicke switch. As shown in Equation 1.2, the modulation eliminates the $\Delta G/G$ term from the NEΔT equation. However, the addition of a lossy switch to the front-end of the receiver increases the T_{eff} of the receiver, which degrades the NEΔT. Minimizing the insertion loss (IL) of Dicke switches is essential to ensure a low receiver noise temperature. Furthermore, high isolation is desirable from these switches as well, as noise leakage from the switched-off path adds error into the input noise.

Millimeter-wave Dicke switches for applications requiring low IL are typically implemented using quarter-wave transmission lines with shunt PIN diodes [121] or FETs [122,123,124], which have low effective on-state resistances (R_{on}) with moderately high off-state resistances (R_{off}). The quarter-wave shunt topology enables excellent IL, but quarter-wave lines require a large chip area and are bandwidth-limiting. In IC switches, fabrication costs are proportional to the chip size, and there is usually a direct tradeoff between the size and the IL of monolithic switches.

This chapter explores the optimal design of compact and low-loss SPDT Dicke switches using SiGe HBTs. SiGe HBTs in the reverse-saturated configuration, where the emitter is used as the RF switching node to prevent parasitic losses through the substrate, have been shown to be excellent shunt switching devices that achieve a high R_{off} to R_{on} ratio [125]. The target application for these switches is the 60 GHz integrated temperature sounding radiometer that is currently being developed for the MicroNimbus CubeSat [127]. Two SiGe HBT Dicke switches have been designed to explore the size-performance tradeoff. The first switch utilizes a traditional quarter-wave shunt topology to achieve the lowest possible IL, while the second switch is implemented using a lumped-element pi matching network topology to achieve a much smaller size. The pi network switch has been submitted for publication [7]. Both switches are designed in the GlobalFoundries BiCMOS8XP technology, which is an enhanced-performance version of the BiCMOS8HP technology discussed in Chapter 3 that offers SiGe HBTs with peak f_T/f_{max} of 250/330 GHz.

6.2 Quarter-Wave Shunt Switch

The quarter-wave shunt switch was designed following the procedure in [125]. A schematic of the switch is shown in Figure 6.1, along with equivalent circuit models of the off-state and on-state shunt SiGe HBTs. To enable "thru mode" operation, reverse-saturated SiGe HBT Q_1 is turned off (nV_{sw} = 0 V) and is modeled as a large R_{off} in parallel with an off-state shunt capacitance (C_{off}). An inductive shunt stub resonates out C_{off}, and the 50 Ω quarter-wave section between Q_1 and the common port behaves as a low-loss matched transition between the input and output. At the same time, SiGe HBT Q_2 is turned on and behaves as a low-value R_{on}. The quarter-wave section between Q_2 and the common port makes this leg present a high impedance to the common port, so the leakage down the

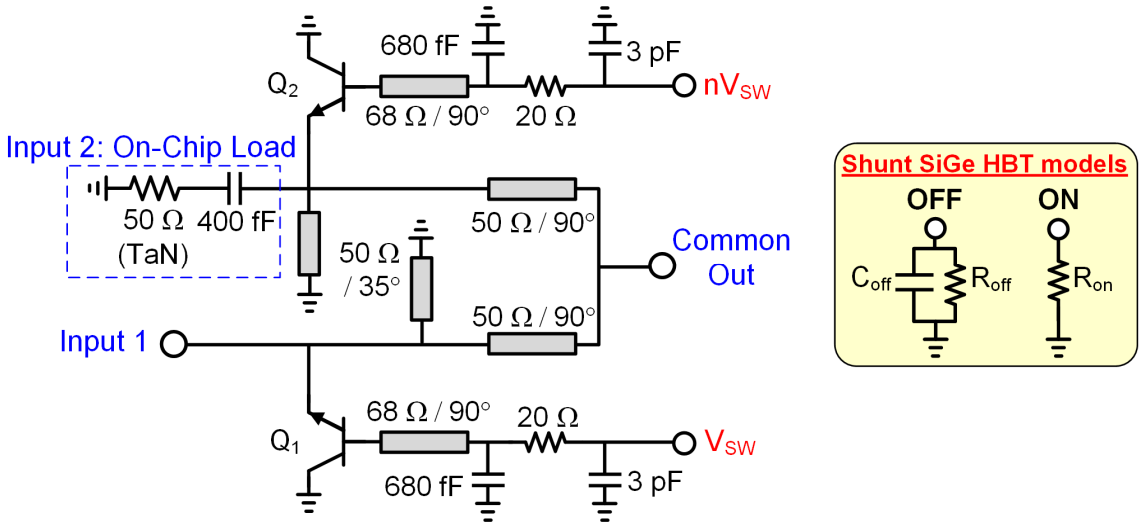

Figure 6.1: Schematic of the quarter-wave shunt SiGe HBT switch and equivalent circuit models of the off-state and on-state shunt SiGe HBTs.

"off" path of the switch is small. To minimize this leakage and prevent reductions in the IL and isolation, it is essential for R_{on} to be very low, to present as large of an impedance as possible to the common port. The loss in the "thru path" of the switch is largely due to the finite value of R_{off}, the IL of the 50 Ω quarter-wave section, and the loss of the shunt stub. To minimize the IL, a high R_{off} is clearly necessary. However a small C_{off} is also desirable, as shorter (more inductive) shunt stubs are lossier than longer (less inductive) shunt stubs, and the loss due to these stubs can be a significant portion of the overall IL.

The first step in the switch design was to design the SiGe HBT switching cells. Small-sized SiGe HBTs have a high R_{off}, however their R_{on} is relatively high as well. Therefore, the SiGe HBT emitter length must be appropriately selected to optimize the R_{on} and R_{off}. Two SiGe HBTs with a maximum emitter length of 18 μm were found to provide the best performance. To enable a simple transistor core layout, SiGe HBTs in a collector-base-emitter (CBE) configuration were used instead of standard collector-base-emitter-base-collector (CBEBC) devices. The via transitions between the emitter and the top metal

Table 6.1: Simulated performance of the quarter-wave switch cell at 60 GHz.

	R_{on}	R_{off}	C_{off}
SiGe HBTs only	2.4 Ω	2.7 kΩ	32 fF
Via transition parasitics included	2.8 Ω	1.3 kΩ	65 fF

layer and between collector and the ground plane were designed using wide arrays of vias to minimize the increase in R_{on} due to the parasitic resistances. The dense metallization near the SiGe HBTs was modeled using parasitic extraction, while the more inductive upper via transitions were EM-simulated using Sonnet. The impact of these via transition parasitics on the performance of the switch cell is summarized in Table 6.1.

It is essential to design the biasing network to present a high RF impedance to the base of each SiGe HBT. A high effective R_{off} is formed by the series combination of the off-state resistances of the emitter-base and collector-base junctions, and presenting a low impedance to the base would effectively bypass the off-state resistance of the collector-base junction and reduce the combined R_{off}, which would increase the switch loss. Therefore, the base of each SiGe HBT was biased using a quarter-wave transmission line to present a low DC resistance and a high RF impedance. A 20 Ω series resistor was included on each bias line to limit the DC current in the on-state following [125]. The EM-simulated bias line presents a frequency-dependent RF resistance to the base with a simulated maximum value of 1.3 kΩ at 61 GHz, which reduces the R_{off} of each switch cell from 1.3 kΩ to 950 Ω. The decrease in R_{off} due to the base biasing network could be reduced by using a large (> 1.3 kΩ) biasing resistor instead of a quarter-wave line, however, each SiGe HBT draws multiple mA of current in the on-state, and the voltage drop across such a large resistor would be significant.

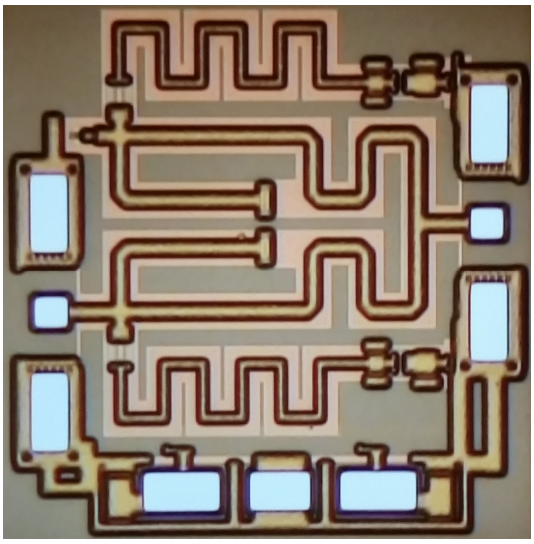

Figure 6.2: Microphotograph of the fabricated quarter-wave SiGe HBT switch, which measures 0.65 mm × 0.65 mm including bondpads and 0.48 mm × 0.53 mm excluding bondpads.

With the switch cell designed, the next step in the design process is to design the passive components. The top thick aluminum layer, AM, was used as the signal trace for the on-chip microstrip lines, and the top thin copper layer, MQ, was selected as the on-chip ground plane. The EM-simulated IL of a 50 Ω quarter-wave microstrip line, implemented using a 650 μm long and 13 μm wide AM trace over MQ, is 0.2 dB. The shunt stubs were implemented using the same 50 Ω AM over MQ traces, and a low-resistance connection between the end of each stub and the ground plane was achieved using multiple wide bar vias. The on-chip Dicke load was implemented using a 50 Ω TaN resistor and a 400 fF DC-blocking MIM capacitor, and has an EM-simulated return loss of greater than 20 dB between 44 GHz and 120 GHz. A microphotograph of the fabricated switch is shown in Figure 6.2. The size of the switch without bondpads is 0.48 mm × 0.53 mm. The on-chip microstrip lines were meandered to reduce the area, but still dominate the size of the chip.

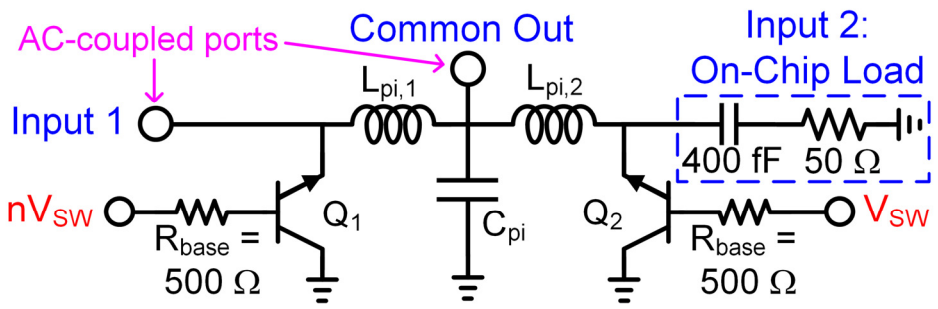

Figure 6.3: Schematic of the SiGe HBT pi-network switch [7].

6.3 Pi-Network Switch

The pi-network switch was designed to achieve similar performance to the quarter-wave switch with a much smaller physical size by using compact lumped-element passives instead of microstrip lines. Topologically, the pi-network switch, shown in Figure 6.3, is similar to the CMOS switch proposed in [127]. To enable "thru mode" operation, reverse-saturated SiGe HBT Q_1 is turned off ($nV_{sw} = 0$ V) and matching inductors $L_{pi,1}$ and the shared C_{pi} ($C_{pi} \approx 2C_{off}$) create a pi matching network which forms a compact and wideband transition between the input and the common ports. Simultaneously, Q_2 ($V_{sw} = 2.5$ V) is turned on and acts as a low R_{on}. The resonance formed by $L_{pi,2}$ and C_{pi} introduces a near-180° shift to R_{on}, which presents a high impedance to the common port and prevents signal leakage to the on-chip load. To enable "Dicke mode" operation, V_{sw} and nV_{sw} are swapped.

This topology presents a high DC impedance to the emitter of each on-state SiGe HBT, which prevents DC current flow through the emitter-base (E-B) junctions. The quarter-wave shunt switch avoids this situation through the use of the shunt stubs, which present a DC ground to the emitter of each SiGe HBT. Unlike FETs, which only require a positive V_{GS} with no current flow to achieve a low R_{on}, SiGe HBTs require forward current to flow through both *pn* junctions. Therefore, it may seem that a low R_{on} cannot be obtained

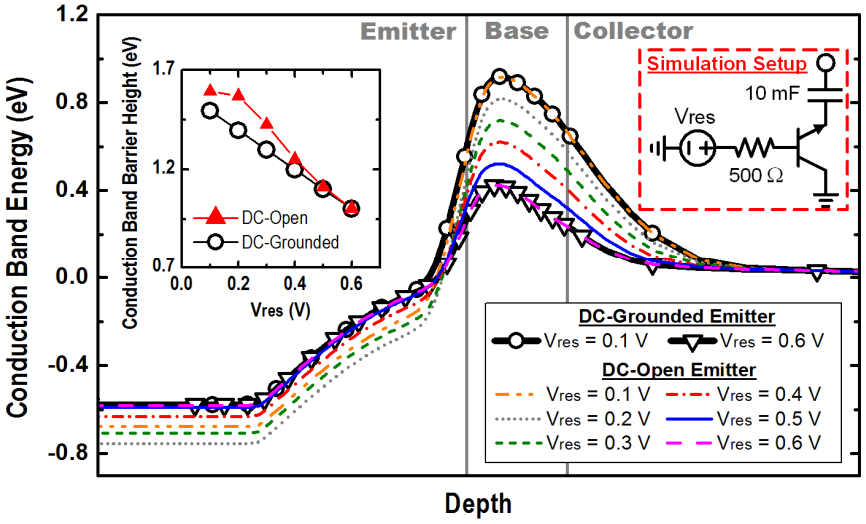

Figure 6.4: TCAD-simulated conduction band energy across bias of a reverse-saturated SiGe HBT for both the grounded and DC-open emitter configurations. The insets show the TCAD simulation schematic and the height of the E-B conduction band barrier versus bias [7].

using SiGe HBTs without presenting a low DC resistance to the emitter that allows for forward biasing of the E-B junction. However, circuit simulations show that a low R_{on} is obtained when a positive V_{BC} is applied, even though no current exits the emitter of the on-state SiGe HBT.

To validate this atypical behavior, physics-based Technology CAD (TCAD) simulations were performed on a calibrated 4th-generation SiGe HBT model with the emitter grounded and DC-opened (modeled using a series capacitor). Figure 6.4 shows the schematic used for TCAD simulations, along with the simulated conduction band energy and E-B barrier height versus bias. The conduction band energy at the emitter differs between the two configurations at low bias, but as the bias is increased the conduction bands of the open-emitter and grounded-emitter devices converge. A forward bias across the internal E-B junction is established on the open-emitter device at bias voltages above 0.5 V even though no current exits the emitter.

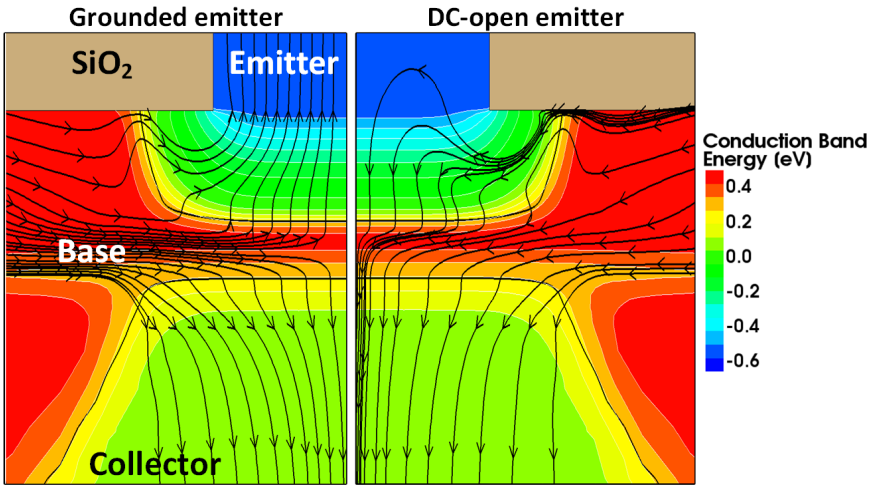

Figure 6.5: 2-D cross-section of the TCAD SiGe HBT biased at V_{res} = 0.6 V (I_B = 23 nA), showing simulated conduction band energy contours and streamlines of the internal electron current flow. The emitter is grounded for the left half-device and is DC-open for the right half-device [7].

Figure 6.5 shows a 2-D cross-section of the simulated SiGe HBT with conduction band energy contours and electron current flow streamlines for each configuration biased at 0.6 V, where the conduction bands are identical. In the open-emitter case, electrons flow from the base into the internal emitter at the spacer oxide interface and are swept back across the base into the collector, forward biasing the E-B junction. AC TCAD simulations indicate that the R_{on} of the DC-open emitter SiGe HBT is identical to that of the grounded emitter SiGe HBT due to this self-biasing effect. Therefore, presenting a high DC resistance to the emitter does not affect the performance of the SiGe HBT in this configuration.

The emitter length of each SiGe HBT was selected to balance R_{on}, R_{off}, and C_{off}, as shown in Figure 6.6. A large emitter area is required to reduce R_{on}, which improves the IL and isolation. However, increasing the device size increases C_{off} and necessitates an increased L_{pi}, which reduces the bandwidth and increases the loss of the physical inductors.

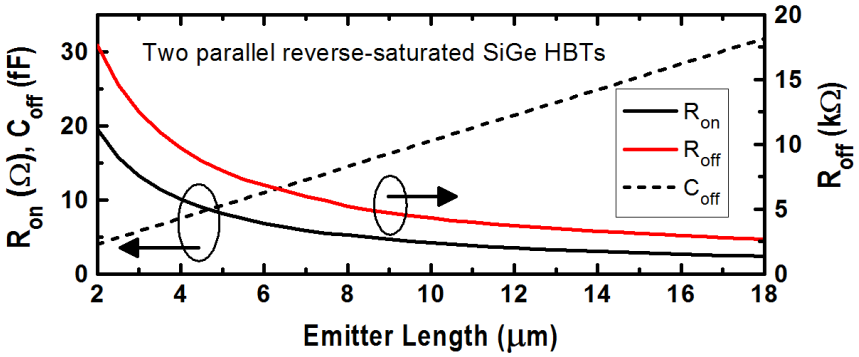

Figure 6.6: Simulated 60 GHz R_{on}, R_{off}, and C_{off} versus emitter length for two parallel shunt SiGe HBTs biased at a current density of 1.08 mA/μm^2 [7].

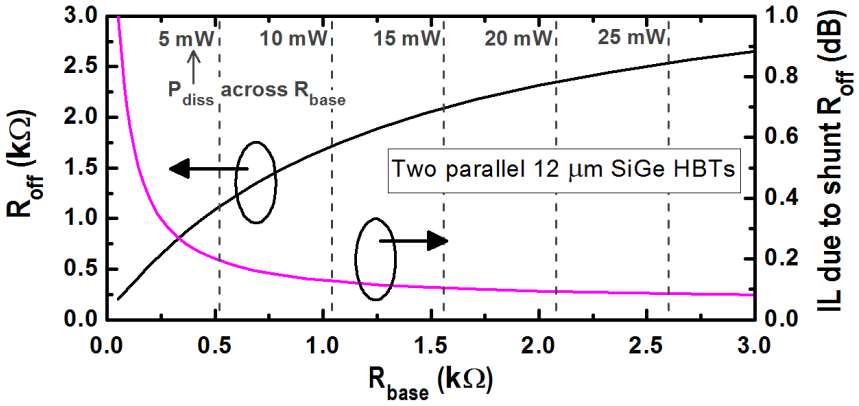

Figure 6.7: Simulated 60 GHz R_{off} and IL due to this shunt R_{off}, for the pi-network switch core versus R_{base} [7]. The dashed vertical lines mark the power dissipation across R_{base} at the fixed 3.1 mA bias current.

On-chip inductors are significantly lossier structures than 50 Ω on-chip microstrip lines, so the losses of the matching elements must be considered while selecting the emitter length of the SiGe HBTs. Two parallel 12 μm SiGe HBTs in a CBE configuration were found to be optimal.

To further reduce the size of the pi-network switch versus the quarter-wave switch, each SiGe HBT base was biased through a large biasing resistor (R_{base}) instead of a quarter-wave line [125]. Figure 6.7 shows how the R_{off} of the shunt SiGe HBT, the IL due to this shunt R_{off}, and the power dissipation across R_{base} at the selected bias current vary with R_{base}.

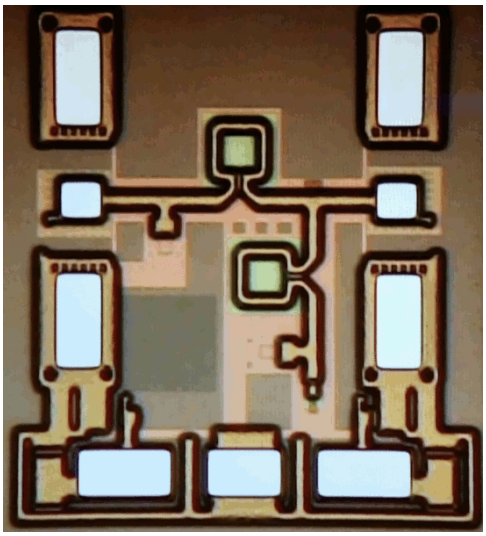

Figure 6.8: Microphotograph of the fabricated pi-network switch, which measures 0.48 mm × 0.52 mm including bondpads and 0.20 mm × 0.32 mm excluding bondpads [7].

An R_{base} value of 500 Ω was selected to keep the power dissipation low while allowing a small increase in IL.

All passive elements and the upper levels of the via transitions to the SiGe HBTs were modeled using Sonnet. At the top metal layer, each shunt SiGe HBT cell has a simulated C_{off} of 49 fF, R_{on} of 3.9 Ω, and R_{off} of 810 Ω at 60 GHz. The values of L_{pi} and C_{pi} were selected to be 106 pH and 90 fF to achieve optimal switch performance at 60 GHz, and the EM-simulated quality factors are 23.1 and 23.0, respectively, at 60 GHz. The Q of C_{pi} is limited by the parasitic resistance and inductance of the vias used to transition between the top metal layer and the upper plate of the MIM capacitor. A photograph of the fabricated pi-network switch is shown in Figure 6.8. The size of the switch without bondpads is only 0.20 mm × 0.32 mm—four times smaller than the quarter-wave switch.

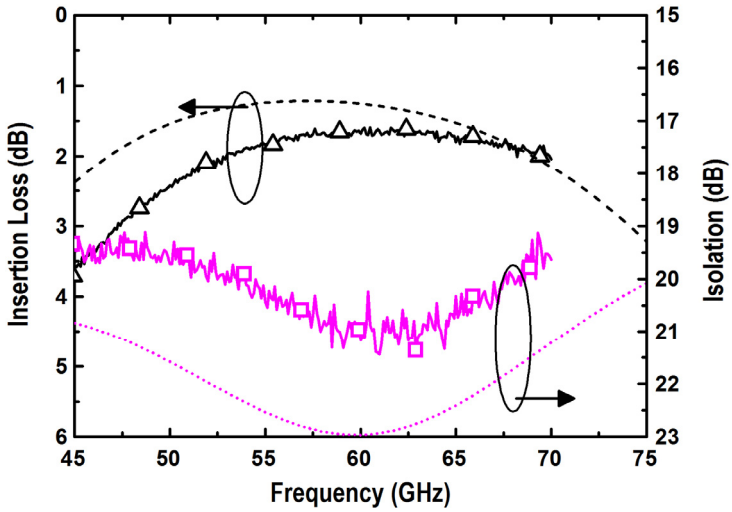

Figure 6.9: Measured and simulated IL and isolation of the quarter-wave SiGe HBT switch.

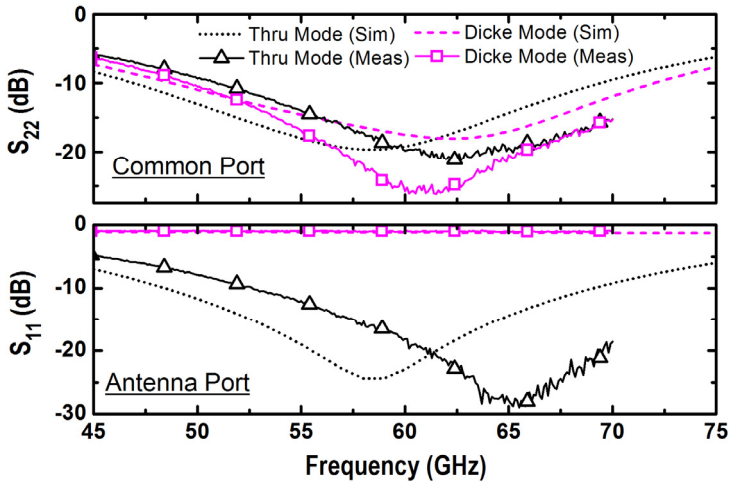

Figure 6.10: Measured and simulated return losses of the quarter-wave SiGe HBT switch in both modes of operation.

6.4 Switch Measurements

The S-parameters of each switch were measured up to 70 GHz using an Agilent E3861C PNA and GGB wafer probes. The bondpads were not deembedded out of the measurement results. The measured and simulated IL and isolation of the quarter-wave switch are shown in Figure 6.9. The IL is larger than simulated—the simulated minimum IL is 1.21 dB at 58 GHz, whereas the measured minimum IL is 1.60 dB at 60.2 GHz. The

mid-band switch isolation is 21 dB, which is degraded from the simulated value of 23 dB. The measured lower 3-dB cutoff frequency is 42 GHz, while the upper edge of the bandwidth is above the maximum frequency of the network analyzer. The measured and simulated return losses of the quarter-wave switch are shown in Figure 6.10. The matching is slightly shifted up in frequency from simulation, and the measured return losses are better than 10 dB from 53 GHz to above 70 GHz.

Figure 6.11 shows close agreement between the measured and simulated IL and isolation of the pi-network switch. The IL is better than 2.0 dB from 36–69 GHz, with a minimum of 1.48 dB at 58 GHz. The lower 3-dB cutoff frequency is 21 GHz, and the upper cutoff frequency is above 70 GHz. The isolation is greater than 20.0 dB from 33–65 GHz, with a peak of 22.1 dB at 49 GHz. The measured and simulated return loss in each mode of operation is shown in Figure 6.12. The matching shifted 4 GHz up in frequency from simulation. The return loss is greater than 9 dB from 34 GHz to beyond 70 GHz. There is a small difference between the return loss at the common port in each mode of operation, which is caused by the differing parasitic capacitances of the input bondpads and the on-chip load.

The results of these switches were unexpected. All components in the two switches were designed and modeled in exactly the same way, yet the IL of the pi-network switch closely agrees with the simulation results while the IL of the quarter-wave switch is significantly higher than simulated. The quarter-wave switch was expected to achieve a minimum IL 0.4 dB lower than that of the pi-network switch, whereas the measured results indicate that the measured minimum IL is actually 0.1 dB higher than that of the pi-network switch. One possible source of the measurement-to-simulation discrepancy is the modeling

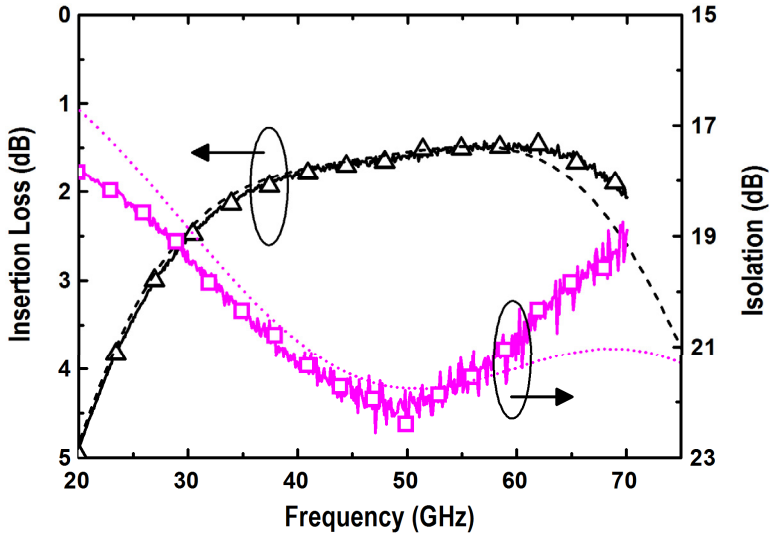

Figure 6.11: Measured and simulated IL and isolation of the pi-network switch versus frequency [7].

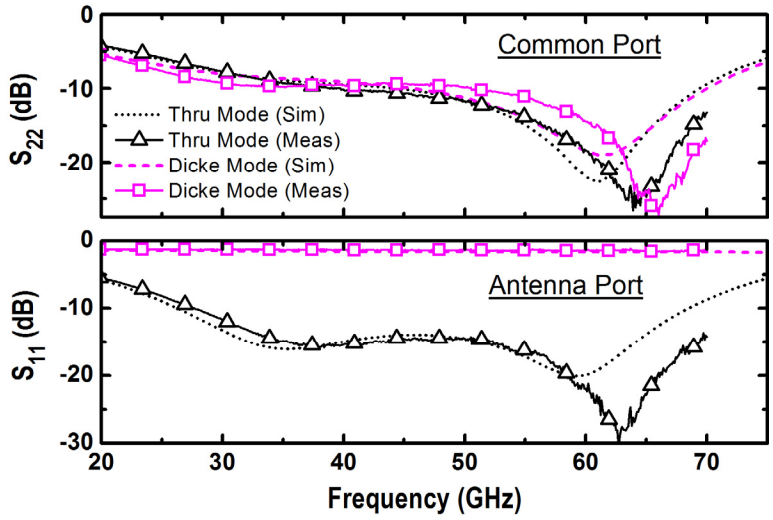

Figure 6.12: Measured and simulated return losses of the pi-network switch in both modes of operation [7].

of the 18 μm SiGe HBTs used in the quarter-wave switch. The SiGe HBT models are not calibrated for the reverse-saturated mode of operation, and because this 18 μm emitter length is the longest allowed by the design kit, it is possible that its modeling is less accurate than that of the 12 μm SiGe HBTs used in the pi-network switch. It is also possible that some inaccuracy exists in the modeling of the terminations of the shunt stubs in the quarter-

Table 6.2: Comparison to similar millimeter-wave SPDT switches [7].

Ref.	Technology	Topology	Freq. (GHz)	IL (dB)	Isol. (dB)	P_{DC} (mW)	Size (mm^2)
This	130 nm Rev. Sat. SiGe HBT	Pi-network	34–70+	1.5–2.1	19–22	7.8	0.064
This	130 nm Rev. Sat. SiGe HBT	λ/4 shunt	51–70+	1.6–2.3	19–21	4.4	0.254
[127]	130 nm CMOS	Pi-network	57–66	1.7–2.0†	>21.1	0	0.020
[122]	90 nm CMOS	λ/4 shunt	50–70	1.5–2.0†	>25	0	0.275
[123]	90 nm CMOS	Asymmetric λ/4 shunt	50–67	1.8–2.3†	>23 / >38	0	0.303
[124]	65 nm triple-well CMOS	Traveling-wave + slow-wave λ/4	17–100	2.6–4.5	15–25	0	0.421*
[121]	130 nm SiGe PIN diode	Series-shunt	51–78	2.0–2.7†	25–35	16.8	0.105
[128]	180 nm Diode-Tied SiGe HBT	Transformer	55–67	2.7–3.0†	13–16	8.1	0.043
[129]	GaAs PIN Diode	Unspecified Shunt	55–86	1.0–2.6	26–45	110	1.96*

*Area includes bondpads †Bondpads are deembedded

wave switch. With proper modifications, it is likely that the quarter-wave switch could achieve a lower measured IL than the pi-network switch.

6.5 Summary

This section presented two low-loss SPDT Dicke switches implemented using reverse-saturated SiGe HBTs. Table 6.2 compares the switches to similar 60 GHz SPDT switches. The bandwidth listed for each of the switches presented in this section corresponds to the frequency range for which the return losses at both ports are better than 9 dB. The quarter-wave switch achieves highly competitive performance to the state-of-the-art, and better performance can most likely be attained with proper optimizations. The pi-network switch achieves the lowest non-deembedded IL to date for silicon SPDT

switches at this frequency, along with a wide bandwidth and a highly compact size. The reverse-saturated SiGe HBTs enable improved IL with a reduced C_{off} compared to the CMOS pi-network switch presented in [127], resulting in a wider bandwidth for this switch. The TCAD analysis shows that when a high resistance is presented to a SiGe HBT emitter, internal current flow creates a self-biasing effect, and the transistor performance is not impacted. Therefore, SiGe HBTs are both capable of achieving superior switch performance to FETs and are also suitable alternatives to FETs for use in switching circuits with high-resistance nodes.

These switches compare favorably to those currently used in 60 GHz radiometers for CubeSats. At 60 GHz low-loss switches are available from commercial vendors, so custom-designed switches are not typically used in radiometers at this frequency. The 60 GHz receiver in the MiRaTA CubeSat uses an Analog Devices HMC-SDD112 GaAs PIN diode switch MMIC [129] as a front-end Dicke switch [130]. The IL and isolation of the HMC-SDD112 switch, which are included in Table 6.2, is better than that of the quarter-wave and pi-network switches presented here, however, the chip size is significantly larger and the power consumption is over 100 mW, far higher than that of the SiGe HBT switches. Additionally, the performance of this switch MMIC will reduce when packaged, whereas a SiGe radiometer chip could integrate a SiGe HBT switch with an LNA on the same die with virtually no loss between the two blocks.

CHAPTER 7

CONCLUSION

7.1 Summary of Contributions

The research presented in this dissertation leveraged SiGe HBT technologies to develop millimeter-wave receiver components for future space-based atmospheric sounding radiometers which require integration and power efficiency. Monolithically integrated SiGe components can potentially enable significant reductions in the size, weight, and power consumption of these instruments and enable economical production of radiometers for proposed constellations of Earth-observing CubeSats. The work presented in this dissertation explored the attainable performance of multiple key components of millimeter-wave radiometer receivers developed using best-in-class SiGe HBTs. The results highlight the ability of custom SiGe HBT integrated circuits to substantially reduce the SWaP of these receivers while enabling comparable radiometric sensitivity to receivers implemented using traditionally-used millimeter-wave components. The specific contributions of this work include:

1. The demonstration of ultra-low noise SiGe HBT LNAs for snow and ice sensing radiometers which achieve an NF as low as 1.10 dB at 18.7 GHz. The use of inductors with localized back-side etching was shown to improve the gain by 0.4 dB and the effective noise temperature by 10%.
2. The design and optimization of *G*-band SiGe HBT LNAs for humidity sounding radiometers which attained a mean NF as low as 8.0 dB across the 165–200 GHz

passive sensing band, which is the lowest measured NF to date for SiGe HBT amplifiers at these frequencies.

3. A wideband and low-power SiGe HBT IF amplifier for power-constrained hyperspectral millimeter-wave radiometers. The amplifier achieved a bandwidth of 17.4–30.4 GHz (54%) with a peak gain of 18 dB, mean NF of 3.1 dB, and output-referred P1dB of 2 dBm while consuming only 24 mW of power. The balanced-performance and low-power amplifier can potentially enable major power savings in IF receiver modules for power-constrained CubeSats or enable a greater number of IF channels for a given system power dissipation.
4. The design, optimization, and characterization of a 19–34 GHz SiGe HBT square-law detector for hyperspectral radiometers which achieves a record 1/*f* corner frequency as low as 11 Hz through careful transistor biasing and judicious use of resistors. These results highlight the ability of active SiGe HBT detectors to reduce the volume and improve the performance, and streamline the design and assembly of hyperspectral IF receiver modules.
5. A 138–170 GHz SiGe HBT frequency doubler with a peak output power of 5.6 dBm, peak PAE of 7.6%, and peak total power efficiency of 10.9%. Although this doubler consumes DC power unlike passive multipliers, the DC power dissipation is only 36 mW at peak drive which is far lower than the hundreds of milliwatts consumed by typical power amplifiers which are needed when passive multipliers are used. The output power and efficiency of this doubler shows the potential of an all-SiGe active multiplier chain to significantly reduce the power consumption of millimeter-wave heterodyne receivers.

6. The first monolithically integrated *G*-band single-sideband downconverter MMIC for CubeSat-based hyperspectral humidity sounding radiometers. The downconverter achieved a SSB NF of 9.9 dB and a DC power dissipation of only 82 mW, both of which are, to the best of our knowledge, the lowest values of all reported *G*-band silicon-based low-noise downconverter MMICs to date.
7. The demonstration of two low-loss SiGe HBT SPDT switches for 60 GHz radiometers. The 1.5 dB IL and 0.064 mm^2 area achieved by the pi-network switch shows that highly compact low-loss switches can be implemented using reverse-saturated shunt SiGe HBTs, and the TCAD analysis shows that SiGe HBTs are suitable alternatives to FETs for use in switching circuits with high-resistance nodes.

7.2 Future Work

7.2.1 SiGe for Earth-Observing CubeSats

The following list presents several ideas for extending this research:

1. First and foremost, although the *G*-band SiGe circuits presented here achieve excellent performance, SiGe circuits will not be used in actual systems unless they can maintain excellent performance after being packaged. Millimeter-wave components for radiometers are typically packaged in split-block waveguide enclosures, so low-loss waveguide-to-chip transitions need to be demonstrated with SiGe HBT circuits. Such transitions are inherently difficult to implement using silicon-based technologies, as silicon-based technologies use on-chip ground planes implemented in the BEOL due to the lossy nature of the silicon substrate,

whereas GaAs and InP technologies usually use the metallization on the bottom of the chip or the waveguide package surface for grounding. Additionally, the high dielectric constant of bulk silicon can cause cavity resonances in waveguide packages which are difficult to eliminate.

2. Active noise sources are commonly used in radiometers to perform frequent receiver calibration. These noise sources are typically implemented using weakly coupled diodes which are biased near avalanche breakdown. Implementing such a noise source on chip and integrating it with the receiver would enable frequent in-situ receiver calibration without the need for a lossy front-end Dicke switch. Numerous semiconductor devices are available in SiGe platforms that can potentially be used as avalanche noise sources, so the optimal design of integrated SiGe noise sources warrants investigation.
3. The millimeter-wave frequency doubler presented in Chapter 4 achieves excellent efficiency compared to typically-used passive millimeter-wave frequency multipliers, however, a complete LO generation chain needs to be demonstrated to assess the potential of custom SiGe circuits to enable power savings in real-world systems. A synthesizer should be implemented on-chip as well, as typical microwave signal sources used in CubeSats are power-hungry and generate more power than would be required by an efficient SiGe LO chain. Demonstrating a SiGe mixer which is monolithically driven by an efficiency-optimized LO synthesis chain would fully illustrate the potential of SiGe to reduce the power consumption and improve the integration of these systems.

4. The performance of the SPDT switches presented in Chapter 6 can potentially be significantly improved. The losses of the microstrip lines in the quarter-wave switch can be reduced through the use wider signal traces and moving the ground plane to a lower metallization layer. Slow-wave on-chip transmission lines can also potentially be used to reduce the IL and physical size of SiGe HBT switches [131,124]. Optimization of the SiGe HBT dimensions and the layouts of the SiGe HBT switching cores could also yield improved performance.
5. A particularly interesting study would be to use a detector with ultra-low $1/f$ noise to characterize the $1/f$ noise of RF circuit blocks, which could yield information on how to optimally design and bias those circuit blocks to minimize their gain variations ($\Delta G/G$, see Section 1.2) for use in radiometers.
6. Receivers in CubeSats are exposed to a wide range of operating temperatures due to the limited ability of CubeSats to provide thermal control and stabilization. Therefore, it is worth investigating biasing techniques to maximize the performance stability of these circuit blocks across temperature, to keep the receiver performance as constant as possible.

7.2.2 SiGe for Deep Space CubeSats

This dissertation focused on SiGe radiometer components for use Earth-observing CubeSats, which experience relatively benign operating conditions. CubeSat technologies continue to advance, and there is increasing interest in using CubeSats for observing other bodies in our solar system such as Europa, Mars, Venus, the Moon, and asteroids [132]. Microwave and millimeter-wave radiometers could be used to characterize the surfaces or atmospheres of these bodies. CubeSats for use in deep space must be capable of operating

in intense radiation environments with wide ranging temperatures and need to communicate over much longer distances than traditional CubeSats operating in low Earth orbit [133,134]. The extreme environments experienced by interplanetary satellites often requires sensitive electronics to be placed inside a vault which provides thermal control and radiation shielding. These vaults are typically not compatible with the constraints of CubeSats. Furthermore, these vaults are particularly problematic for radiometers, as placing receiver electronics inside a vault would require a long transition between an external antenna and the shielded electronics, and this transition would be lossy and have a significant thermal gradient. A radiometer implementation like this would suffer from suboptimal sensitivity.

SiGe HBTs can potentially yield significant benefits for CubeSats operating in these environments. SiGe HBTs are tolerant to multi-Mrad(SiO_2) doses of total-dose radiation (see Figure 1.3), and they can operate across wide temperatures ranging from less than 1 K to greater than 200° C [135]. Single-event effects (SEE) can be problematic in SiGe circuits, but SEE is an issue with all scaled semiconductor devices, and the development of SEE mitigation techniques for SiGe HBT circuits is an active research area [135,50]. To illustrate the capabilities of SiGe HBT circuits for extreme environments, a remote sensor interface (RSI) ASIC and a packaged remote electronics unit module which does not require shielding from the operational environment were developed under the NASA Exploration Technology Development Program using a standard SiGe BiCMOS platform. Through the use of radiation-hardening-by-design (RHBD) techniques, the RSI was demonstrated to function properly across temperatures from -180° C to +120° C and up to a radiation dose of 100 krad(Si) [136,137].

The potential of SiGe HBT technologies to develop radiation-hardened millimeter-wave radiometers and rugged sensor electronics for use in interplanetary CubeSats warrants further research. Rugged SiGe circuits could allow for shielding reductions in these CubeSats that would reduce costs and/or enable more data collection for a given payload volume. The inherent total-dose radiation tolerance of a SiGe radiometer could enable more data collection before radiation-induced failures occur. The performance of SiGe millimeter-wave radiometer components in the context of extreme environments should be explored as the first step towards developing SiGe radiometers for interplanetary CubeSats, with a particular focus on investigating SEE in these receivers and developing components which are minimally sensitive to SEE and can function effectively across wide temperature ranges. SEE are currently difficult to explore in millimeter-wave circuits due to the limited bandwidths of oscilloscopes. One possibility that is currently being explored is the potential use of high-frequency power detectors to identify and characterize SEE in millimeter-wave receivers [139].

REFERENCES

[1] C. T. Coen *et al*., "Integrated silicon-germanium electronics for cubesat-based radiometers," in *Proc. IEEE International Geoscience and Remote Sensing Symposium*, 2013, pp. 1286-1289.

[2] C. T. Coen *et al*., "Development of silicon-germanium circuits for high-frequency small satellite-based integrated radiometers," in *Proc. USNC/URSI National Radio Science Meeting*, 2014, pp. 1-1.

[3] C. T. Coen *et al*., "Ultra-low noise and low power 18.7 GHz radiometer LNAs in a 0.5 THz SiGe technology utilizing back-side etched inductors," in *Proc. IEEE Bipolar/BiCMOS Circuits and Technology Meeting*, 2014, pp. 191–194.

[4] C. T. Coen *et al*., "Design and On-Wafer Characterization of G-Band SiGe HBT Low-Noise Amplifiers," *IEEE Transactions on Microwave Theory and Techniques*, vol. 64, no. 11, pp. 3631–3642, November 2016.

[5] C. T. Coen *et al*., "A 19–34 GHz SiGe HBT Square-Law Detector with Ultra-Low 1/f Noise for Atmospheric Radiometers," in *European Microwave Integrated Circuits Conference*, 2017, under review.

[6] C. T. Coen *et al*., "A Highly-Efficient 138–170 GHz SiGe HBT Frequency Doubler for Power-Constrained Applications," in *IEEE Radio Frequency Integrated Circuits Symposium*, 2016, pp. 23–26.

[7] C. T. Coen *et al*., "A Compact, Wideband, and Low-Loss 60 GHz Pi Network SPDT Switch Using SiGe HBTs," *IEEE Microwave and Wireless Components Letters*, 2017, submitted.

[8] National Research Council, *Earth Science and Applications from Space: National Imperatives for the Next Decade and Beyond*. Washington, DC: The National Academies Press, 2007.

[9] B. Lambrigtsen *et al*., "A Baseline for the Decadal-Survey PATH Mission," in *IEEE International Geoscience and Remote Sensing Symposium (IGARSS)*, 2008, pp. III-338–III-341.

[10] W. J. Blackwell, "The Next Frontier: Nanosatellite Constellations for High-Resolution Microwave Earth Remote Sensing," in *93rd American Meteorological Society Annual Meeting*, 2013.

[11] D. Selva and D. Krejci, "A survey and assessment of the capabilities of Cubesats for Earth observation," *Acta Astronautica*, vol. 74, pp. 50–68, June 2012.

[12] D. Selva and D. Krejci, "Preliminary Assessment of Performance and Cost of a Cubesat Component of the Earth Science Decadal Survey," in *Proc. AIAA/USU Conference on Small Satellites*, 2013, pp. 1–14.

[13] B. Lim *et al*., "The Radiometer Atmospheric CubeSat Experiment (RACE) pre-launch performance," in *IEEE MTT-S International Microwave Symposium Digest*, 2015, pp. 1–3.

[14] W. J. Blackwell *et al*., "MicroMAS: A First Step Towards a Nanosatellite Constellation for Global Storm Observation," in *Proc. AIAA/USU Conference on Small Satellites*, 2013, pp. 1–10.

[15] W. J. Blackwell *et al*., "Microwave Radiometer Technology Acceleration Mission (MiRaTA): Advancing Weather Remote Sensing with Nanosatellites," in *Proc. AIAA/USU Conference on Small Satellites*, 2014, pp. 1–15.

[16] L. Periasamy and A. J. Gasiewski, "Precision Design, Analysis and Manufacturing of Quasi-optic Lens/Reflector Antenna Systems for CubeSat MMW/SMMW Radiometers," in *Proc. USNC-URSI National Radio Science Meeting*, 2016, pp. 1–1.

[17] S. C. Reising *et al*., "Overview of Temporal Experiment for Storms and Tropical Systems (TEMPEST) CubeSat constellation mission," in *IEEE MTT-S International Microwave Symposium Digest*, 2015, pp. 1–4.

[18] F. T. Ulaby *et al*., *Microwave Remote Sensing: Active and Passive, Volume I*. Reading, MA: Addison-Wesley, 1981.

[19] N. Skou and D. M. Le Vine, *Microwave Radiometer Systems: Design and Analysis*, 2nd ed. Boston, MA: Artech House, 2006.

[20] R. R. Ferraro *et al*., "NOAA operational hydrological products derived from the advanced microwave sounding unit," *IEEE Transactions on Geoscience and Remote Sensing*, vol. 43, no. 5, pp. 1036–1049, May 2005.

[21] C. Muth *et al*., "Advanced technology microwave sounder on the National Polar-Orbiting Operational Environmental Satellite System," in *IEEE International Geoscience and Remote Sensing Symposium*, 2005, pp. 99–102.

[22] D. B. Kunkee *et al*., "Design and Evaluation of the First Special Sensor Microwave Imager/Sounder," *IEEE Transactions on Geoscience and Remote Sensing*, vol. 46, no. 4, pp. 863–883, Apr. 2008.

[23] D. A. Newell *et al*., "GPM Microwave Imager design, predicted performance and status," in *IEEE International Geoscience and Remote Sensing Symposium*, 2010, pp. 546–549.

[24] W. J. Blackwell, "Millimeter-Wave Receivers for Low-Cost CubeSat Platforms," in *IEEE MTT-S International Microwave Symposium Digest*, 2015, pp. 1–3.

[25] W. Blackwell and J. Pereira, "New Small Satellite Capabilities for Microwave Atmospheric Remote Sensing: The Earth Observing Nanosatellite-Microwave (EON-MW)," in *Proc. AIAA/USU Conference on Small Satellites*, 2015.

[26] B. Lim *et al*., "CHARM: A CubeSat water vapor radiometer for earth science," in *IEEE International Geoscience and Remote Sensing Symposium*, 2012, pp. 1022–1025.

[27] B. Lim *et al*., "Development of the Radiometer Atmospheric CubeSat Experiment payload," in *IEEE International Geoscience and Remote Sensing Symposium*, 2013, pp. 849–851.

[28] P. Kangaslahti *et al*., "Low noise amplifier for 180 GHz frequency band," in *IEEE MTT-S International Microwave Symposium Digest*, 2008, pp. 451–454.

[29] S. Padmanabhan *et al*., "Microwave Atmospheric Sounder on CubeSat (MASC) Prototype," in *Proc. USNC-URSI National Radio Science Meeting*, 2016, pp. 1–1.

[30] M. Ogut *et al*., "Tropospheric Water and Cloud ICE (TWICE) Instrument Development for 6U CubeSat Deployment: Back-End Electronic Design and Testing," in *Proc. USNC-URSI National Radio Science Meeting*, 2016, pp. 1–1.

[31] J. D. Cressler, Ed., *Silicon Heterostructure Handbook – Materials, Fabrication, Devices, Circuits, and Applications of SiGe and Si Strained-Layer Epitaxy*. Boca Raton, FL: CRC Press, 2006.

[32] M. Kaynak *et al*., "MEMS module integration into SiGe BiCMOS technology for embedded system applications," in *Proc. IEEE Bipolar/BiCMOS Circuits and Technology Meeting*, 2012, pp. 1–7.

[33] D. Knoll *et al*., "High-Performance BiCMOS Si Photonics Platform," in *Proc. IEEE Bipolar/BiCMOS Circuits and Technology Meeting*, 2015, pp. 88–96.

[34] H. Rucker *et al*., "Half-Terahertz SiGe BiCMOS Technology," in *IEEE Topical Meeting on Silicon Monolithic Integrated Circuits in RF Systems*, 2012, pp. 133–136.

[35] P. Chevalier *et al*., "Towards THz SiGe HBTs," in *Proc. IEEE Bipolar/BiCMOS Circuits and Technology Meeting*, 2011, pp. 57–65.

[36] A. Ç. Ulusoy *et al*., "An investigation of fT and fmax degradation due to device interconnects in 0.5 THz SiGe HBT technology," in *Proc. IEEE Bipolar/BiCMOS Circuits and Technology Meeting*, 2014, pp. 211–214.

[37] R. L. Schmid *et al*., "A comparison of the degradation in RF performance due to device interconnects in advanced SiGe HBT and CMOS technologies," *IEEE Transactions on Electron Devices*, vol. 62, no. 6, pp. 1803–1810, June 2015.

[38] B. Heinemann *et al*., "SiGe HBT with fT/fmax of 505 GHz/720 GHz," in *IEEE International Electron Devices Meeting*, 2016, pp. 3.1.1–3.1.4.

[39] P. S. Chakraborty *et al*., "A 0.8 THz fMAX SiGe HBT operating at 4.3 K," *IEEE Electron Device Letters*, vol. 35, no. 2, pp. 151–153, Feb. 2014.

[40] J. Yuan *et al*., "On the Performance Limits of Cryogenically Operated SiGe HBTs and Its Relation to Scaling for Terahertz Speeds," *IEEE Transactions on Electron Devices*, vol. 56, no. 5, pp. 1007–1019, May 2009.

[41] J. Hacker *et al*., "InP HBT Amplifier MMICs Operating to 0.67 THz," in *IEEE MTT-S International Microwave Symposium Digest*, 2013, pp. 1–3.

[42] A. Tessmann *et al*., "243 GHz low-noise amplifier MMICs and modules based on metamorphic HEMT technology," *International Journal of Microwave and Wireless Technologies*, vol. 6, no. 3/4, pp. 215–223, Jun. 2014.

[43] X. Mei *et al*., "First Demonstration of Amplification at 1 THz Using 25-nm InP High Electron Mobility Transistor Process," *IEEE Electron Device Letters*, vol. 36, no. 4, pp. 327–329, Apr. 2015.

[44] T. A. Doiron, "Low Power Silicon Germanium Electronics for Microwave Radiometers," in *IEEE International Geoscience and Remote Sensing Symposium*, 2001, pp. 1007–1009.

[45] F. Alimenti *et al*., "On the feasibility of single-chip SiGe microwave radiometric sensors," in *IEEE European Microwave Conference*, 2004, pp. 1033–1036.

[46] L. Aluigi *et al*., "Design of a Ka-Band LNA for SoC space-based millimeter-wave radiometers," in *IEEE MTT-S International Microwave Workshop Series on Millimeter Wave Integration Technologies*, 2011, pp. 156–159.

[47] J. D. Cressler and G. Niu, *Silicon-Germanium Heterojunction Bipolar Transistors*. Norwood, MA: Artech House, 2003.

[48] J.-S. Rieh and S. Kim, "Technology and design considerations for millimeter-wave circuits," in *International Conference on Solid-State and Integrated Circuit Technology*, 2008, pp. 1352–1356.

[49] L. S. Vempati *et al*., "Low-Frequency Noise in UHV/CVD Epitaxial Si and SiGe Bipolar Transistors," *IEEE Journal of Solid-State Circuits*, vol. 31, no. 10, pp. 1458–1467, October 1996.

[50] J. D. Cressler and H. A. Mantooth, Eds., *Extreme Environment Electronics*. Boca Raton, FL: CRC Press, 2012.

[51] J. D. Cressler, "On the Potential of SiGe HBTs for Extreme Environment Electronics," *Proceedings of the IEEE*, vol. 93, no. 9, pp. 1559–1582, Sep. 2005.

[52] D. Cline *et al*., "Parametric Evaluation of Cold-Land Processes Measurement Technologies, Final Report To NASA Earth Science Technology Office," NASA Earth Science Technology Office, Goddard Space Flight Center, 2003.

[53] R. L. Schmid *et al*., "Best Practices to Ensure the Stability of SiGe HBT Cascode Low Noise Amplifiers," in *Proc. IEEE Bipolar/BiCMOS Circuits and Technology Meeting*, 2012, pp. 194–197.

[54] W.-M. L. Kuo *et al*., "An X-Band SiGe LNA With 1.36 dB Mean Noise Figure for Monolithic Phased Array Transmit/Receive Radar Modules," in *Proc. IEEE Radio Frequency Integrated Circuits Symposium*, 2006, pp. 395-398.

[55] F. Korndorfer *et al*., "Simulation and Measurement of Back Side Etched Inductors," in *European Microwave Conference*, 2010, pp. 1631-1634.

[56] C. Tsironis, "AN-19: On-Wafer Noise Parameter Measurements Using Cold-Noise Source and Automatic Receiver Calibration," Focus Microwaves, Inc., 1999.

[57] T. K. Thrivikraman *et al*., "A 2 mW, Sub-2 dB Noise Figure, SiGe Low-Noise Amplifier for X-Band High-Altitude or Space-Based Radar Applications," in *Proc. IEEE Radio Frequency Integrated Circuits Symposium*, 2007, pp. 629-632.

[58] B.-W. Min and G. M. Rebeiz, "Ka-Band SiGe HBT Low Noise Amplifier Design for Simultaneous Noise and Input Power Matching," *IEEE Microwave and Wireless Components Letters*, vol. 17, no. 12, pp. 891-893, 2007.

[59] M.-H. Tsai *et al*., "An Ultra-Low Power K-Band Low-Noise Amplifier Co-Designed With ESD Protection in 40-nm CMOS," in *IEEE International Conference on IC Design & Technology (ICICDT)*, 2011, pp. 1-4.

[60] L. Liu *et al*., "InP-HEMT X-Band Low-Noise Amplifier With Ultralow 0.6-mW Power Consumption," *IEEE Electron Device Letters*, vol. 33, no. 2, pp. 209-211, 2012.

[61] A. H. Akgiray *et al*., "Noise Measurements of Discrete HEMT Transistors and Application to Wideband Very Low-Noise Amplifiers," *IEEE Transactions on Microwave Theory and Techniques*, vol. 61, no. 9, pp. 3285-3297, 2013.

[62] M. Elkhouly *et al*., "220-250-GHz phased-array circuits in 0.13-µm SiGe BiCMOS technology," *IEEE Transactions on Microwave Theory and Techniques*, vol. 61, no. 8, pp. 3115-3127, Aug. 2013.

[63] C. R. Poole and D. K. Paul, "Optimum noise measure terminations for microwave transistor amplifiers," *IEEE Transactions on Microwave Theory and Techniques*, vol. 33, no. 11, pp. 1254-1257, Nov. 1985.

[64] M. Karkkainen *et al*., "MHEMT G-band low-noise amplifiers," *IEEE Transactions on Terahertz Science and Technology*, vol. 4, no. 4, pp. 459-468, Jul. 2014.

[65] T. Gaier *et al*., "Measurement of a 270 GHz low noise amplifier with 7.5 dB noise figure," *IEEE Microwave and Wireless Components Letters*, vol. 17, no. 7, pp. 546-548, Jul. 2007.

[66] K. Eriksson *et al*., "Design and characterization of H-band (220–325 GHz) amplifiers in a 250-nm InP DHBT technology," *IEEE Transactions on Terahertz Science and Technology*, vol. 4, no. 1, pp. 56-64, Jan. 2014.

[67] Emerson & Cuming Microwave Products Inc. (2007, May) *ECCOSORB® HR Lightweight Flat-Sheet Broadband Microwave Absorbers*. [Online]. http://www.eccosorb.com/Collateral/Documents/English-US/HR.pdf.

[68] C. R. Dietlein, "Components and metrology for terahertz imaging," Ph.D. Dissertation, Dept. Elect. and Comp. Eng., Univ. Colorado, Boulder, CO, 2008.

[69] "Power Measurement Above 110 GHz," Virginia Diodes, Inc., Charlottesville, VA, Application Note VDI-704, 2007.

[70] P. Kangaslahti *et al*., "Low Noise Amplifier Receivers for Millimeter Wave Atmospheric Remote Sensing," in *IEEE MTT-S International Microwave Symposium Digest*, 2012, pp. 1-3.

[71] Virginia Diodes, Inc. *WR5.1SHM*. [Online]. http://vadiodes.com/index.php/en/products/mixers?id=130.

[72] A. Ç. Ulusoy *et al*., "A SiGe D-band low-noise amplifier utilizing gain-boosting technique," *IEEE Microwave and Wireless Components Letters*, vol. 25, no. 1, pp. 61-63, Jan. 2015.

[73] R. Ben Yishay *et al*., "A 122-150 GHz LNA with 30 dB gain and 6.2 dB noise figure in SiGe BiCMOS technology," in *Proc. IEEE Silicon Monolithic Integrated Circuits in RF Systems*, 2015, pp. 15–17.

[74] Y. Zhao *et al*., "A 160-GHz Subharmonic Transmitter and Receiver Chipset in an SiGe HBT Technology," *IEEE Transactions on Microwave Theory and Techniques*, vol. 60, no. 10, pp. 3286-3299, Oct. 2012.

[75] E. Ojefors *et al*., "A 160-GHz low-noise downconversion receiver front-end in a SiGe HBT technology," *International Journal of Microwave and Wireless Technologies*, vol. 3, no. 3, pp. 347-353, Mar. 2011.

[76] E. Dacquay *et al*., "D-band total power radiometer performance optimization in an SiGe HBT technology," *IEEE Transactions on Microwave Theory and Techniques*, vol. 60, no. 3, pp. 813-826, March 2012.

[77] D. Fritsche *et al*., "A broadband 200 GHz amplifier with 17 dB gain and 18 mW DC-power consumption in 0.13 μm SiGe BiCMOS," *IEEE Microwave and Wireless Components Letters*, vol. 24, no. 11, pp. 790-792, Nov. 2014.

[78] E. Ojefors *et al*., "Subharmonic 220- and 320-GHz SiGe HBT receiver front-ends," *IEEE Transactions on Microwave Theory and Techniques*, vol. 60, no. 5, pp. 1397–1404, May 2012.

[79] S. Malz *et al*., "A 233-GHz low noise amplifier with 22.5dB gain in 0.13μm SiGe," in *Proc. European Microwave Integrated Circuits Conference*, 2014, pp. 190–193.

[80] E. Weissbrodt *et al*., "Low-noise amplifiers in D-band using 100 nm and 50 nm mHEMT technology," in *Proc. German Microwave Conference*, 2010, pp. 55–58.

[81] M. Varonen *et al*., "160-270-GHz InP HEMT MMIC low-noise amplifiers," in *Tech. Dig. IEEE Compound Semiconductor Integrated Circuit Symposium*, 2012, pp. 1–4.

[82] G. Moschetti *et al*., "A 183 GHz metamorphic HEMT low-noise amplifier with 3.5 dB noise figure," *IEEE Microwave and Wireless Components Letters*, vol. 25, no. 9, pp. 618-620, Sep. 2015.

[83] A. Tessmann *et al*., "Metamorphic HEMT MMICs and modules for use in a high-bandwidth 210 GHz radar," *IEEE Journal of Solid-State Circuits*, vol. 43, no. 10, pp. 2194-2205, Oct. 2008.

[84] Z. Wang *et al*., "A CMOS 210-GHz fundamental transceiver with OOK Modulation," *IEEE Journal of Solid-State Circuits*, vol. 49, no. 3, pp. 564–580, Mar. 2014.

[85] W. J. Blackwell *et al*., "Hyperspectral microwave atmospheric sounding," *IEEE Transactions on Geoscience and Remote Sensing*, vol. 49, no. 1, pp. 128–142, January 2011.

[86] W. J. Blackwell *et al*., "Design and analysis of a hyperspectral microwave receiver subsystem," in *IEEE International Geoscience and Remote Sensing Symposium*, 2012, pp. 3435–3438.

[87] W. Blackwell *et al*., "Technology Development for a Hyperspectral Microwave Atmospheric Sounder (HyMAS)," in *Earth Science Technology Forum*, 2014.

[88] L. Hilliard *et al*., "Hyperspectral microwave atmospheric sounder (HyMAS) - New capability in the CoSMIR/CoSSIR scanhead," in *IEEE Aerospace Conference*, 2015, pp. 1–9.

[89] C. Galbraith, private communication, Sep. 2014.

[90] S. Seth *et al*., "On the RF properties of weakly saturated SiGe HBTs and their potential use in ultralow-voltage circuits," *IEEE Electron Device Letters*, vol. 32, no. 1, pp. 3–5, January 2011.

[91] F. Inanlou *et al*., "A 1.0 V, 10–22 GHz, 4 mW LNA utilizing weakly saturated SiGe HBTs for single-chip, low-power, remote sensing applications," *IEEE Microwave and Wireless Components Letters*, vol. 24, no. 12, pp. 890–892, Dec. 2014.

[92] T. Kanar and G. M. Rebeiz, "X- and K-Band SiGe HBT LNAs with 1.2- and 2.2-dB mean noise figures," *IEEE Transactions on Microwave Theory and Techniques*, vol. 62, no. 10, pp. 2381–2389, Oct. 2014.

[93] M. El-Nozahi *et al*., "A millimeter-wave (23–32 GHz) wideband BiCMOS low-noise amplifier," *IEEE Journal of Solid-State Circuits*, vol. 45, no. 2, pp. 289–299, Feb. 2010.

[94] P. K. Saha *et al*., "Analysis and design of a 3–26 GHz low-noise amplifier in SiGe HBT technology," in *Proc. IEEE Radio and Wireless Symposium*, 2012, pp. 203–206.

[95] H.-K. Chen *et al*., "Analysis and design of a 1.6–28-GHz compact wideband LNA in 90-nm CMOS using a pi-match input network," *IEEE Transactions on Microwave Theory and Techniques*, vol. 58, no. 8, pp. 2092–2104, Aug. 2010.

[96] Analog Devices, Inc. *HMC519 GaAs pHEMT MMIC Low Noise Amplifier, 18-32 GHz*. [Online]. http://www.analog.com/media/en/technical-documentation/data-sheets/hmc519chips.pdf.

[97] M. Uzunkol *et al*., "Design and analysis of a low-power 3–6-Gb/s 55-GHz OOK receiver with high-temperature performance," *IEEE Transactions on Microwave Theory and Techniques*, vol. 60, no. 10, pp. 3263–3271, Oct. 2012.

[98] J. W. May and G. M. Rebeiz, "Design and characterization of W-Band SiGe RFICs for passive millimeter-wave imaging," *IEEE Transactions on Microwave Theory and Techniques*, vol. 58, no. 5, pp. 1420–1430, May 2010.

[99] E. S. Malotaux and M. Spirito, "Characterization of broadband low-NEP square-law detectors for mm-wave passive imaging," in *IEEE MTT-S International Microwave Symposium*, 2016, pp. 1–4.

[100] T. Kanar and G. M. Rebeiz, "A low-power 136-GHz SiGe total power radiometer with NETD of 0.25 K," *IEEE Transactions on Microwave Theory and Techniques*, vol. 64, no. 3, pp. 906–914, Mar. 2016.

[101] A. Tomkins *et al*., "A passive W-band imaging receiver in 65-nm bulk CMOS," *IEEE Journal of Solid-State Circuits*, vol. 45, no. 10, pp. 1981–1991, Oct. 2010.

[102] M. Uzunkol and G. M. Rebeiz, "A low-noise 150-210 GHz detector in 45 nm CMOS SOI," *IEEE Microwave and Wireless Components Letters*, vol. 23, no. 6, pp. 309–311, June 2013.

[103] V. Vassilev *et al*., "140–220-GHz DHBT detectors," *IEEE Transactions on Microwave Theory and Techniques*, vol. 61, no. 6, pp. 2353–2360, June 2013.

[104] MACOM. *MSS20,000 Series Zero Bias Schottky Diodes*. [Online]. https://www.macom.com/products/product-detail/MSS20-141-B10D

[105] C. Galbraith, private communication, Jan. 2014.

[106] Virginia Diodes, Inc. *WR5.1x2*. [Online]. http://vadiodes.com/index.php/en/products/full-band-multipliers-wr-series/10-products/152-wr51x2.

[107] W. J. Blackwell, private communication, Mar. 2014.

[108] J.-J. Hung *et al*., "High-power high-efficiency SiGe Ku- and Ka-band balanced frequency doublers," *IEEE Transactions on Microwave Theory and Techniques*, vol. 53, no. 2, pp. 754–761, Feb. 2005.

[109] D. G. Thomas Jr. and G. R. Branner, "Single-ended HEMT multiplier design using reflector networks," *IEEE Transactions on Microwave Theory and Techniques*, vol. 49, no. 5, pp. 990–993, May 2001.

[110] P. B. Leite, "Design and modeling of mm-wave integrated transformers in CMOS and BiCMOS technologies," Ph.D. Dissertation, Université Bordeaux 1, 2011.

[111] L. Wang *et al*., "Millimeter-wave frequency doubler with transistor grounded-shielding structure in 0.13-µm SiGe BiCMOS technology," *IEEE Transactions on Microwave Theory and Techniques*, vol. 59, no. 5, pp. 1304–1310, May 2011.

[112] Y. Li *et al*., "A Frequency doubler/modulator with 4.5 dBm output power at 170 GHz using SiGe HBTs," *IEEE Microwave and Wireless Component Letters*, vol. 25, no. 3, pp. 181-183, Mar. 2015.

[113] H.-C. Lin and G. M. Rebeiz, "A 200-245 GHz balanced frequency doubler with peak output power of +2 dBm," in *Tech. Dig. IEEE Compound Semiconductor Integrated Circuit Symposium*, 2013, pp. 1–4.

[114] E. Ojefors *et al*., "Active 220- and 325-GHz frequency multiplier chains in an SiGe HBT technology," *IEEE Transactions on Microwave Theory and Techniques*, vol. 59, no. 5, pp. 1311–1318, May 2011.

[115] H.-C. Lin and G. M. Rebeiz, "A 135–160 GHz balanced frequency doubler in 45 nm CMOS with 3.5 dBm peak power," in *IEEE MTT-S International Microwave Symposium*, 2014, pp. 1–4.

[116] M. Bao *et al*., "A high power-efficiency D-band frequency tripler MMIC with gain up to 7 dB," *IEEE Microwave and Wireless Components Letters*, vol. 24, no. 2, pp. 123–125, Feb. 2014.

[117] U. J. Lewark *et al*., "A miniaturized unit cell for ultra-broadband active millimeter-wave frequency multiplication," *IEEE Transactions on Microwave Theory and Techniques*, vol. 62, no. 6, pp. 1343–1351, June 2014.

[118] M. Abbasi *et al*., "Single-chip frequency multiplier chains for millimeter-wave signal generation," *IEEE Transactions on Microwave Theory and Techniques*, vol. 57, no. 12, pp. 3134–3142, Dec. 2009.

[119] B. Sheinman *et al*., "A double balanced 81-86GHz EBAND active down conversion mixer in SiGe technology," in *Proc. IEEE Bipolar/BiCMOS Circuits and Technology Meeting*, 2013, pp. 183–186.

[120] D. Fritsche *et al*., "A low-power SiGe BiCMOS 190 GHz receiver with 47 dB conversion gain and 11 dB noise figure for ultra-large-bandwidth applications," in *Proc. IEEE Radio Frequency Integrated Circuits Symp.*, 2016, pp. 290–293.

[121] I. Kallfass *et al*., "A 200 GHz active heterodyne receiver MMIC with low sub-harmonic LO power requirements for imaging frontends," in *Proc. European Microwave Integrated Circuits Conf.*, 2009, pp. 45–48.

[122] K. Lam *et al*., "Wideband Millimeter Wave PIN Diode SPDT Switch using IBM 0.13µm SiGe Technology," in *Proc. European Microwave Integrated Circuits Conference*, 2007, pp. 108–111.

[123] M. Uzunkol and G. M. Rebeiz, "A low-loss 50–70 GHz SPDT switch in 90 nm CMOS," *IEEE Journal of Solid-State Circuits*, vol. 45, no. 10, pp. 2003–2007, Oct. 2010.

[124] C. W. Byeon and C. S. Park, "Design and analysis of the millimeter-wave SPDT switch for TDD applications," *IEEE Transactions on Microwave Theory and Techniques*, vol. 61, no. 8, pp. 2858–2864, Aug. 2013.

[125] X.-L. Tang *et al*., "A traveling-wave CMOS SPDT using slow-wave transmission lines for millimeter-wave application," *IEEE Electron Device Letters*, vol. 34, no. 9, pp. 1094–1096, Sep. 2013.

[126] R. L. Schmid *et al*., "On the analysis and design of low-loss single-pole double-throw W-Band switches utilizing saturated SiGe HBTs," *IEEE Transactions on Microwave Theory and Techniques*, vol. 62, no. 11, pp. 2755–2767, November 2014.

[127] W. Williams *et al*., "MicroNimbus: A CubeSat temperature profilometer for the Earth's atmosphere using a single-chip 60 GHz SiGe radiometer," in *IEEE International Geoscience and Remote Sensing Symposium*, 2017, to be presented.

[128] J. He *et al*., "Analysis and design of 60-GHz SPDT switch in 130-nm CMOS," *IEEE Transactions on Microwave Theory and Techniques*, vol. 60, no. 10, pp. 3113–3119, Oct. 2012.

[129] R. L. Schmid *et al*., "A compact, transformer-based 60 GHz SPDT RF switch utilizing diode-connected SiGe HBTs," in *Proc. IEEE Bipolar/BiCMOS Circuits Technology Meeting*, 2013, pp. 111–114.

[130] Analog Devices, Inc. *HMC-SDD112 GaAs PIN MMIC SPDT Switch 55-86 GHz*. [Online]. http://www.analog.com/media/en/technical-documentation/data-sheets/hmc-sdd112.pdf

[131] K. Cahoy *et al*., "The Microwave accelerometer technology acceleration CubeSat (MiRaTA)," in *Earth Science Technology Forum*, 2014.

[132] A.-L. Franc *et al*., "High-performance shielded coplanar waveguides for the design of CMOS 60-GHz bandpass filters," *IEEE Transactions on Electron Devices*, vol. 59, no. 5, pp. 1219–1226, May 2012.

[133] A. Freeman, "Deep space nanosats – positioned for exponential growth," in *Proc. Small Satellites, System & Services (4S) Symposium*, 2016, pp. 1–15.

[134] A. Poghosyan and A. Golkar, "CubeSat evolution: analyzing CubeSat capabilities for conducting science missions," *Progress in Aerospace Sciences*, vol. 88, pp. 59–83, Jan. 2017.

[135] R. J. Staehle *et al*., "Interplanetary CubeSats: opening the solar system to a broad community at lower cost," *Journal of Small Satellites*, vol. 2, no. 1, pp. 161–186, July 2013.

[136] J. D. Cressler, "Radiation effects in SiGe technology," *IEEE Transactions on Nuclear Science*, vol. 60, no. 3, pp. 1992-2014, June 2013.

[137] R. M. Diestelhorst *et al*., "A new approach to designing electronic systems for operation in extreme environments: Part I - the SiGe remote sensor interface," *IEEE Aerospace and Electronic Systems Magazine*, vol. 27, no. 6, pp. 25–34, June 2012.

[138] T. D. England *et al*., "A new approach to designing electronic systems for operation in extreme environments: Part II - the SiGe remote electronics unit," *IEEE Aerospace and Electronic Systems Magazine*, vol. 27, no. 7, pp. 29–41, July 2012.

[139] A. Ildefonso *et al*., "Utilizing SiGe HBT power detectors for sensing single-event transients in RF circuits," in *IEEE Nuclear and Space Radiation Effects Conference*, 2017, to be presented.

VITA

Christopher T. Coen was born in Burnsville, Minnesota in 1987 and moved to Acworth, Georgia in 1998. Chris enrolled at the Georgia Institute of Technology in 2005, where he earned a B.S. in Electrical Engineering in 2009 and an M.S. in Electrical and Computer Engineering in 2012. He has been a research assistant in Dr. John D. Cressler's SiGe Devices and Circuits Group since Fall 2008, focusing on the development of receiver components for millimeter-wave radiometers using SiGe technologies. Chris was a recipient of an inaugural NASA Office of the Chief Technologist's Space Technology Research Fellowship in 2011.

Chris worked part-time for Arylessence Inc, a manufacturer of chemical fragrances and flavors in Marietta, GA, from 2004–2007. He interned with Lockheed Martin in Manassas, Virginia in 2007 and in Eagan, Minnesota in 2008. As part of his NASA Fellowship, Chris interned at NASA's Goddard Space Flight Center in Greenbelt, Maryland each summer from 2012–2015 and at MIT Lincoln Laboratory in Lexington, Massachusetts in Fall 2014. After receiving his doctorate degree, Chris will join the Advanced Concepts Laboratory at the Georgia Tech Research Institute in Atlanta, Georgia.